Numerical and experimental modeling of thin metal plates forming process

Bubalo, Ante

UNIVERSITY OF ZAGREB

FACULTY OF MECHANICAL ENGINEERING AND NAVAL ARCHITECTURE

Ante Bubalo

NUMERICAL AND EXPERIMENTAL MODELING OF THIN METAL PLATES FORMING PROCESS

DOCTORAL THESIS

Zagreb, 2024

UNIVERSITY OF ZAGREB

FACULTY OF MECHANICAL ENGINEERING AND NAVAL ARCHITECTURE

Ante Bubalo

NUMERICAL AND EXPERIMENTAL MODELING OF THIN METAL PLATES FORMING PROCESS

DOCTORAL THESIS

Supervisor:

Prof. Zdenko Tonković, PhD

Zagreb, 2024

SVEUČILIŠTE U ZAGREBU

FAKULTET STROJARSTVA I BRODOGRADNJE

Ante Bubalo

NUMERIČKO I EKSPERIMENTALNO MODELIRANJE PROCESA OBLIKOVANJA TANKIH METALNIH PLOČA

DOKTORSKI RAD

Mentor:

Prof. dr. sc. Zdenko Tonković

Zagreb, 2024

BIBLIOGRAPHY DATA

UDC:	629.3:669.018:519.6
Keywords:	thin plate forming, finite element method, material anisotropy, thermoplasticity, ABAQUS, digital image correlation, thermography
Scientific area:	Technical sciences
Scientific field:	Mechanical engineering
Institution:	Faculty of Mechanical Engineering and Naval Architecture (FAMENA), University of Zagreb
Supervisor:	Prof. Zdenko Tonković, PhD
Number of pages:	137
Number of pictures:	86
Number of tables:	17
Number of references:	143
Date of oral examination:	30.09.2024.
Jury members:	Assoc. Prof. Tomislav Lesičar, PhD Prof. Vedrana Cvitanić, PhD Prof. Lovre Krstulović-Opara, PhD
Archive:	FAMENA, University of Zagreb

ACKNOWLEDGMENTS

First of all, I express my deepest gratitude to my supervisor Prof. Zdenko Tonković for individual guidance, support and encouragement through my research. His advice was always given at the right time, making this journey memorable and finally feasible.

I am also grateful to the members of my dissertation committee, Prof. Vedrana Cvitanić, Prof. Lovre Krstulović-Opara and Prof. Tomislav Lesičar, for their help with the experimental and numerical investigations at the early stages of this work. Their constructive feedback and suggestions significantly improved the quality of this dissertation.

Special thanks go to all my colleagues at Yazaki Europe Limited, whose support made this journey enjoyable. I am particularly thankful to Thomas Schaller, Josip Jelak, Vedran Mahović and Dalibor Zorica for their assistance and guidance.

Additionally, I would like to thank Prof. Janoš Kodvanj and Dr. sc. Martin Surjak for their invaluable assistance with the experimental setup and measurement, which were crucial parts of this research.

I am also thankful to Denis Pevec and Lea Ljubić for their help in evaluating numerical and experimental results.

My sincere thanks go to my parents, Milan and Štefica, sister Josipa, brother Tomislav, and all my friends, relatives, and people who were always by my side.

Finally, I would like to express my deepest appreciation to my family, my wife Ljubica and daughters Lucija and Mila. Their patience and encouragement have been a constant source of strength, without which this thesis would not have been possible.

Thank you,
Ante Bubalo

Zagreb, 2024

SPECIAL ACKNOWLEDGEMENTS

I express my gratitude to Yazaki Europe Limited for providing testing samples and unlimited support through its tooling and testing capabilities in the Zagreb department.

Thank you,

Ante Bubalo

Zagreb, 2024

ABSTRACT

Wire crimping, a process commonly used in the automotive industry, is a solderless method for establishing electrical and mechanical connections between wire strands and terminals. The complexity of predicting the final shape of a crimped terminal and the imperative to minimize production costs indicate the use of advanced numerical methods. Such an approach requires a reliable phenomenological elasto-plastic constitutive model in which material behaviour during the forming process is described. Copper alloy sheets, known for their ductility and strength, are commonly selected as terminal materials. Generally, sheet metals exhibit significant anisotropy in mechanical properties, and this phenomenon has not been sufficiently investigated experimentally for copper alloy sheets. Furthermore, the wire crimping process is conducted at higher velocities; therefore, the influence of the strain rate on the terminal material behaviour has to be known.

The influence of the strain rate on the anisotropic elasto-plastic behaviour of the copper alloy sheet CuFe2P is experimentally investigated. Tensile tests with strain rates of 0.0002 s^{-1}, 0.2 s^{-1}, 1 s^{-1}, and 5.65 s^{-1} were conducted on sheet specimens with orientations of 0°, 45°, and 90° to the rolling direction. The influence of the strain rate on the orientation dependences of the stress–strain curve, elastic modulus, tensile strength, elongation, and Lankford coefficient was determined. In addition to the uniaxial tensile test, cylindrical cup deep drawing, non-standard compression test and crimping process were made. With the usage of DIC and IRT methods, it was feasible to determine the thermoplastic behaviour of the material during the forming process.

The numerical model for the wire crimping process is established, incorporating the description of anisotropic elasto-plastic material behaviour at different strain rates, thermoplasticity, and an advanced contact algorithm, such as cohesion. Based on the numerical results the main aim of this study was achieved, to determine the optimum compression of terminals with predefined mechanical properties of wires and terminal joint.

KEYWORDS: thin plate forming, wire crimping, finite element method, plastic material anisotropy, thermoplasticity, strain rate, copper alloy, ABAQUS, digital image correlation, thermography

PROŠIRENI SAŽETAK

Sve stroži zahtjevi u autoindustriji u pogledu pouzdanosti i sigurnosti, zajedno s upotrebom novih materijala, oblika konstrukcijskih komponenata i tehnologija proizvodnje mogu se realizirati jedino primjenom naprednih metoda analize konstrukcije i opisivanja ponašanja materijala. Ovo je slučaj i kod postupka krimpanja (stezanja), odnosno čvrstog spajanja žica i tankih metalnih ploča (eng. *terminal*, u literaturi na hrvatskom jeziku često korišten izraz kabelska stopica), koji sve više zamjenjuje proces lemljenja. Dinamičkim procesom deformiranja krimpanjem omogućuje se oblikovanje kabelske stopice i žica u gotov proizvod kroz mehaničko deformiranje bez dodavanja materijala. Iz tog razloga je postupak krimpanja izrazito rasprostranjen u autoindustriji, za razliku od lemljenja koji je dosta složeniji i skuplji postupak jer iziskuje unos topline i dodatni materijal. Kabelska stopica se nakon krimpanja znatno deformira i poprima novi oblik u kojem krila stopice obuhvaćaju bakrene žice u cijelosti. Pritom kontaktna površina između bakrene žice i krila stopice znatno utječe na mehanička svojstva i na električni otpor. Kabelske stopice se obično proizvode iz legiranih bakrenih traka koje se postupkom valjanja stanjuju na željenu debljinu. Osim promjene debljine, valjanje uzrokuje promjenu čvrstoće, duktilnosti i anizotropije mehaničkih svojstava materijala.

Tijekom postupka krimpanja materijal ulazi u plastično područje te se trajno deformira u željeni oblik. Velike brzine deformiranja uzrokuju oslobađanje toplinske energije uslijed pojave plastične deformacije u materijalu. Tijekom dinamičkog procesa deformiranja kabelske stopice i žice, unutar materijala generira se toplinski tok te dolazi do lokalnog porasta temperature. Uslijed razlike temperatura unutar materijala dolazi do provođenja topline. Ukoliko je temperatura zakrimpane stopice nakon deformiranja viša od temperature okolišnjeg medija, javlja se prijenos topline konvekcijom između okolišnjeg medija i kabelske stopice. Osim toga, toplina se oslobađa uslijed trenja između licni žice te između licni žice i stopice tijekom tlačenja. Kako se proces krimpanja odvija u kratkom vremenu, može se pretpostaviti da je proces adijabatski.

Za optimizaciju postupka definiranje konačnog oblika zakrimpane kabelske stopice uz smanjenje troškova razvoja i proizvodnje, u zadnje vrijeme primjenjuje se metoda konačnih elemenata (MKE) čime se numeričkom simulacijom nastoji zamijeniti, odnosno nadopuniti skupi eksperiment. Značajan utjecaj na točnost numeričkog postupka ima odabir konačnih

elemenata, formuliranje konstitutivnih modela s pripadnim karakteristikama materijala te opisivanje rubnih uvjeta, dinamičkih efekata, geometrijske nelinearnosti, trenja, elastičnog povrata, prijenosa topline i velikih kontaktnih pritisaka. U literaturi je izveden niz algoritama, no samo rijetki objedinjuju veći dio nabrojenih efekata.

Zbog izrazito nelinearnog ponašanja materijala uslijed velikih deformacija pri velikim brzinama deformiranja, za modeliranje procesa krimpanja jako je važno što točnije opisati realno ponašanje materijala. Dostupni podaci svojstava materijala ne opisuju dovoljno točno ponašanje materijala pri velikim deformacijama i velikim brzinama deformiranja. Osim toga, važna je procjena faktora trenja. Istraživanja se provode s ciljem modeliranja trenja tijekom postupka oblikovanja deformiranjem primjenom analitičkih, eksperimentalnih i numeričkih metoda. Ovisnost faktora trenja o kontaktnom pritisku te utjecaj adhezije i pojave brazdi na površini materijala se sve više istražuje. U radovima koji se bave problematikom krimpanja analiziran je također utjecaj izbora faktora trenja, kao i utjecaj elastičnog povrata na konačni oblik zakrimpane kabelske stopice u numeričkim analizama. Zaključeno je da adhezija ima veliki utjecaj u procesu krimpanja na elastični povrat materijala.

Za rješavanje problema nelinearnog nestacionarnog prijenosa topline spregnutog s materijalno i geometrijski nelinearnom mehaničkom analizom općenito se primjenjuju dvije metode: potpuno spregnuta i sekvencijalno spregnuta analiza. Za slučaj krimpanja primjenjuje se potpuno spregnuta analiza, gdje se toplinska i mehanička analiza odvijaju istovremeno u jednom koraku. Kada se brzina generiranja topline uslijed disipacije mehaničke energije može zanemariti u analizi prijenosa topline, uobičajeno se primjenjuje sekvencijalno spregnuta toplinsko-mehanička analiza. Nadalje, za integriranje toplinskih jednadžbi i jednadžbi gibanja vremenska derivacija obično se aproksimira primjenom implicitnih i eksplicitnih metoda konačnih razlika. Implicitna vremenska integracija uključuje uzastopna računanja velikog broja jednadžbi, tako da za slučaj dinamičke analize kontakta i trenja klizanja postaje dosta neučinkovita, jer se kod implicitne metode javlja problem konvergencije. Stoga se za nelinearne dinamičke simulacije oblikovanja deformiranjem, odnosno krimpanja, najviše primjenjuje eksplicitna metoda. Eksplicitna metoda je puno zahtjevnija u pogledu računalnih resursa, ali uz umjetno povećanje gustoće materijala vrijeme trajanja simulacija se može drastično smanjiti, no uz mogućnost pojave nefizikalnih rezultata. Prvotni numerički modeli procesa krimpanja bili su dvodimenzijski (2D). Ovi modeli nisu mogli točno opisati uzdužna produljenja bakrene žice, kao i zaostala naprezanja za daljnja istraživanja elastičnog povrata,

ali su mogli poslužiti za procjenu geometrije zakrimpane kabelske stopice na žicu. U zadnje vrijeme, povećanjem računalnih resursa počele su se provoditi i trodimenzijske (3D) simulacije. Utjecaj konstitutivnog modela, elastičnog povrata i faktora trenja na konačni oblik željenog proizvoda analiziran je u radovima. Pritom se simulacija procesa deformiranja provodi eksplicitnom metodom, a elastični povrat korištenjem implicitne metode. Ovaj pristup daje nešto točnije rezultate, ali vrijeme računanja se znatno povećava zbog prisutne nelinearnosti, kontaktnih pritisaka i trenja klizanja.

Provođenje eksperimentalnih istraživanja je ključni korak u razumijevanju i modeliranju ponašanja materijala tijekom procesa krimpanja. Eksperimentalna istraživanja u ovom radu usmjerena su na određivanje i analizu mehaničkih svojstava za dva različita materijala koji se koriste u procesu krimpanja: čistog bakra (Cu-ETP) i bakrene legure (CuFe2P). Svojstva čistog bakra se koriste za materijalno modeliranje žice, dok se bakrena legura koristi za modeliranje kabelske stopice. Vlačna ispitivanja provedena su na uzorcima lima bakrene legure CuFe2P kako bi se odredila mehanička svojstva pri različitim brzinama deformacije. Uzorci su izrađeni rezanjem ploča debljine 0,8 mm, a ispitivanja su obuhvatila različite orijentacije uzoraka u odnosu na smjer valjanja (0°, 45° i 90°). Korištene brzine deformiranja pri vlačnom ispitivanju su 0,0002 s^{-1}, 0,2 s^{-1}, 1 s^{-1}, i 5,65 s^{-1}. Kako bi se precizno izmjerila deformacija uzoraka tijekom ispitivanja, korištena je metoda korelacije digitalne slike (DIC). Uzorci su obojeni stohastičkim uzorkom (crne točke na bijeloj podlozi) kako bi se omogućilo praćenje pomaka i deformacija uzoraka tijekom rastezanja. Uz DIC metodu, korištena je i infracrvena termografija za mjerenje porasta temperature na površini uzoraka, čime se dobiva uvid u termoplastično ponašanje materijala tijekom deformacije. Također su provedena i kompresijska ispitivanja Cu-ETP i CuFe2P limova, pri različitim brzinama. Tijekom ispitivanja, također je korištena metoda digitalne korelacije slike i termografija.

Eksperimentalna ispitivanja postupka krimpanja provedena su pomoću aplikatora za krimpanje integriranog na hidrauličku kidalicu, kako bi se ostvarile što veće brzine krimpanja. Cilj je bio simulirati proces krimpanja u kontroliranim uvjetima pri različitim brzinama, od kvazistatičkih do dinamičkih uvjeta. Korištenjem DIC i IR metoda, dobivene su vrijednosti deformacija i prirasta temperature na mjernom području, kako bi se rezultati mogli usporediti s rezultatima numeričkih modela.

Postavljen je numerički model procesa krimpanja žice koji uključuje anizotropno ponašanje materijala u ovisnosti o brzini deformiranja, termoplastičnost, te napredni kontaktni algoritam,

kao što je kohezija. Kako bi se ocijenila točnost numeričkih simulacija, rezultati su validirani eksperimentalnim podacima. To uključuje usporedbu deformacija, naprezanja i temperatura dobivenih simulacijom s onima izmjerenim tijekom eksperimentalnih ispitivanja.

Numerički rezultati su pokazali visoku razinu podudaranja s eksperimentalnim podacima, uz realno opisivanje anizotropnog ponašanja materijala za slučaj velikih deformacija i brzina deformiranja, kontakta, trenja te elastičnog povrata. Navedenom numeričkom formulacijom provedena je evaluacija mehaničkih svojstava zakrimpane kabelske stopice te je omogućena izrada kabelske stopice s unaprijed definiranim mehaničkim svojstvima.

Provedena istraživanja i rad tijekom izrade ove disertacije rezultirali su sljedećim znanstvenim doprinosima u području numeričke mehanike:

- Vlačnim ispitivanjima je dokazana izraženost anizotropije, odnosno ovisnost mehaničkih svojstava razmatrane bakrene legure o orijentaciji uzorka u odnosu na smjer valjanja.

- Pokazano je kako brzina deformiranja utječe na mehanička svojstva bakrene legure kao što su vlačna čvrstoća, istezljivost, modul elastičnosti i Lankfordov parametar. S povećanjem brzine deformiranja općenito se povećava vlačna čvrstoća i istezljivost materijala u svim ispitanim usmjerenjima epruveta, dok modul elastičnosti ostaje konstantan.

- Vlačnim ispitivanjima je pokazano da se Lankfordov parametar mijenja s iznosom deformacije čime se dovodi u pitanje uobičajena pretpostavka da je konstantan.

- Pokazano je kako neelastični toplinski udio (eng. *Inelastic Heat Fraction*) varira s brzinom deformiranja i orijentacijom uzorka u odnosu na orijentaciju uzorka s obzirom na pravac valjanja, što ukazuje na to da sposobnost materijala da pretvori plastični rad u toplinu nije konstantna vrijednost.

- Pokazano je kako brzina deformiranja i orijentacija uzorka utječe na kut loma uzorka materijala.

- Na temelju eksperimentalnih rezultata predložen je numerički model za simuliranje procesa deformiranja materijala kabelske stopice i žice.

- Definiran je učinkovit numerički model za simulaciju procesa krimpanja žica. To omogućuje točnije numeričko modeliranje procesa oblikovanja deformiranjem u odnosu na postojeće algoritme.

- Izvršena je validacija predloženog numeričkog modela primjenom metode korelacije digitalne slike i infracrvene termografije.

- Rezultati istraživanja omogućuju dobivanje kabelske stopice s unaprijed definiranim mehaničkim svojstvima.

Provedeno istraživanje je u doktorskom radu prikazano kroz osam poglavlja. U prvom poglavlju dan je uvod u rad koji opisuje polje istraživanja te su navedeni motivacija, svrha, hipoteze i ciljevi rada. Prikazan je pregled dosadašnjih teorijskih, eksperimentalnih i numeričkih istraživanja procesa oblikovanja tankih metalnih ploča. Navedena bibliografija sadrži relevantne radove za razmatrano područje.

Drugo poglavlje uključuje opis procesa krimpanja i pojave anizotropije materijala u tijeku proizvodnje kabelske stopice.

Treće poglavlje pruža temeljiti opis metoda mjerenja primijenjenih u ovom radu što uključuje uređaje za vlačno ispitivanje, mehaničke ekstenzometre, uređaj koji se temelji na metodi korelaciji digitalne slike (DIC), infracrvenu kameru te uređaj za računalnu tomografiju.

U četvrtom poglavlju prikazani su rezultati eksperimentalnih istraživanja mehaničkog ponašanja materijala koji se koriste u procesu krimpanja: čistog bakra (Cu-ETP) i bakrene legure (CuFe2P). Pritom su svojstva čistog bakra korištena za materijalno modeliranje žice, dok su svojstva bakrene legure korištena za modeliranje kabelske stopice.

U petom poglavlju dan je sažeti prikaz izraza za opisivanje elastoplastičnog anizotropnog ponašanja materijala što uključuje kriterije tečenja, očvršćenje materijala, pridruženo i nepridruženo pravilo tečenja materijala te termoplastičnost.

U šestom poglavlju prikazan je numerički model za simulaciju procesa krimpanja primijenjen u ovom radu, a koji se temelji na metodi konačnih elemenata.

Usporedba rezultata numeričkih simulacija i eksperimentalnih ispitivanja dana je u sedmom poglavlju. Najprije je provedena validacija numeričkog modela na jednostavnijim primjerima

kao što su ispitivanje dubokog vučenja i kompresijsko ispitivanje bakrenih limova, a zatim je numerički model validiran na složenom ispitivanju procesa krimpanja žica, odnosno čvrstog spajanja žica i kabelske stopice.

U zadnjem poglavlju rada dani su zaključci istraživanja. Osim toga, dane su preporuke za odabir mogućih smjerova daljnjih istraživanja.

TABLE OF CONTENTS

LIST OF FIGURES

LIST OF TABLES

NOMENCLATURE

A	-	area
c	-	specific heat capacity
c_v	-	specific heat capacity at constant volume
$\mathbf{C}$	-	elastic stiffness matrix
E	-	elastic modulus
G_s	-	shear modulus
$F(\boldsymbol{\sigma})$	-	yield criterion
$f(\boldsymbol{\sigma})$	-	yield function
F, G, H, L, M, N	-	Hill1948 yield function anisotropy parameters
n	-	strain hardening exponent
k	-	thermal conductivity
K	-	strength coefficient
r	-	Lankford coefficient
$r_0, r_{15}, r_{30}, r_{45}, r_{60}, r_{75}, r_{90}$	-	Lankford coefficient for specimen with 0°, 15°, 30°, 45°, 60°, 75° and 90° to the rolling direction
R_n	-	normal anisotropy parameter
$R_{11}, R_{22}, R_{33}, R_{12}, R_{13}, R_{23}$	-	anisotropy yield stress ratios
ΔR	-	planar anisotropy parameter
T	-	temperature
ΔT	-	temperature change
Q_e	-	thermoelastic heating
Q	-	saturation parameter
α	-	coefficient of thermal expansion
β	-	inelastic heat fraction
ε	-	strain
$\boldsymbol{\varepsilon}$	-	strain tensor
ε_e	-	elastic strain
ε_{pl}	-	plastic strain
$\varepsilon^p{}_{22}$	-	plastic strain in specimen width direction
$\varepsilon^p{}_{33}$	-	plastic strain in specimen thickness direction
λ	-	Lame constant

ρ	-	mass density
σ	-	stress
$\boldsymbol{\sigma}$	-	stress tensor
$\mathbf{C}', \mathbf{C}''$	-	transformation tensors
c'_{ijkl}, c''_{ijkl}	-	anisotropy coefficients
σ_x	-	stress in *x*-direction
$\sigma_{0.01}$	-	stress at 0.01 plastic strain
$\sigma_{0.2}$	-	stress at 0.2 plastic strain
σ_M	-	tensile strength
$d\lambda$	-	plastic multiplier
I_1, I_2, I_3	-	stress invariants
τ	-	shear stress
Θ	-	break angle
ν	-	Poisson's ratio

Chapter 1

Introduction

1.1. Motivation

Wire crimping is one of the basic methods of connecting wires and terminals, it is often used because of its simplicity, reliability and low cost. A solid connection between the wire and the terminal is realized by the plastic deformation of the terminal wings. Without crimping simulation, trial and error methods with real parts would consume a lot of time and increase the overall costs. Due to that, the need for the development of crimping simulations is high. That can also be seen in a number of literature and ongoing studies. As the crimping process is dynamic, it occurs in a small amount of time and numerical simulation can give great insight into what is happening during crimping. The importance of understanding the crimping process and its parameters impact on the mechanical and electrical performance of terminal is high. The motivation to write a thesis about crimping simulations comes from the need to point out the new challenges and gaps in related literature.

The possibility to accurately simulate the crimping process is an essential step in order to produce terminal design with adequate crimping tools that would have good mechanical properties. Also, due to the increasing demands in automotive industry new improvements to the crimping process are needed. To catch up with new demands, there is a clear need for a deeper understanding of the crimping process. The correlation between parameters like material properties, terminal design, tool geometry and process parameters are not investigated enough. Any of these parameters can make impact on the mechanical strength and performance

of the crimp connection. By developing advanced simulation models, it would be possible to have a clear view into the complex interactions between the crimping components and possibility to optimize the design and process.

Furthermore, there is a trend started by some car manufacturers as a request to reduce the number of real laboratory testing and exchange them with numerical simulations. This so-called *virtual validation* is part of ongoing automotive digitalization. Traditional testing and product validation of real parts is time-consuming and costly. The ability to simulate the crimping process using finite element analysis gives a cost and time effective alternative. One iteration loop of numerical simulations is significantly less time-consuming, as traditional laboratory testing requires real terminal samples, which are complex to produce. By developing advanced simulation techniques, it is possible to evaluate a wide range of terminal designs using different crimping tools and materials. The final goal is to predict the behaviour of crimped connections under various loading conditions. The goal of this approach is not just to decrease the product development time, but also to provide a deeper understanding of crimp behaviour under influence of different crimping parameters, which may not be feasible with traditional trial-and-error approaches.

The development of more advanced crimping numerical models can be extended to other areas, not just to crimping applications. Investigations made for these numerical models can help in better understanding of material behaviour under assumption of finite deformations. Also, numerical approach can be used for determination of a final product shape in the context of metal forming process. Consequently, a thesis with focus on crimping simulations, through material behaviour investigation, has a potential to contribute to the fields of materials science and manufacturing technology.

1.2. State of the art

The development of effective and reliable crimp connections is an important step in a wire harness production. Especially in sectors that are crucial in passenger safety for automotive, aerospace or similar industries. Crimping refers to the process of deforming a terminal to its plastically deformed shape, which will secure a conductor wire. This process, which is the mechanical joining of two different parts, does not involve welding or soldering. Between terminal and wire strands will be a metal-to-metal contact, capable of conducting electrical

conductivity in harsh environments [1]. The quality of a crimp connection is determined by its mechanical strength [2–4] and electrical resistance [5–7]. The performance of the crimped terminal is influenced by various parameters like the base material of the terminal, its thickness, the size and strand number of the wire, terminal serration shape, crimping tools shape [8], and the crimping process itself [9,10]. With the increasing demand for reliability in electrical connections, by new revisions of crimping specification, there has been an increase of interest in understanding of the wire crimping process [11,12]. In the early stages of wire harness production, the foundation of crimp standards and the evaluation of crimp quality were based mostly on empirical testing and gathered experience [13]. However, as reliability requirements have increased, a deeper investigation in order to understand ongoing principles of good crimp performance has become necessary. Especially as the amount of electrical components in vehicles is increasing yearly, even without the trend of increasing the number of electric vehicles [14]. Due to this need, there is a purpose to new development and investigation in this field of area.

The study of wire crimping processes has shown a great evolution, which is related to an increase in computation power. In earlier stages, two-dimensional (2D) simulations were made, mostly due to computational constraints. Despite that limitation they provide good observation in terms of understanding the crimping process. For 2D approaches, the initial investigation is related to plane stress or plane strain assumptions [15,16]. With the increase of computation power, the limitations of 2D models were recognized, as they could not consider third dimension and longitudinal expansion of the material. An additional disadvantage was related to the impossibility of evaluating the springback effects as real material deformation cannot be described [17,18]. The transition to three-dimensional (3D) simulations made a significant improvement in this investigation area. 3D models allowed a far better understanding of the crimping process and the possibility of capturing complex interactions and deformations which were not possible with 2D simulations. Authors Mocellin et al. in study [19] presented advantages of 3D crimping simulations in regard to the actual behaviour of materials during crimping [20]. In work [21] comparison of 3D and 2D crimping simulations is made related to the difference in wire and terminal compression ratio and impact of the terminal wings penetration into the wire strands. Based on that difference it can still be seen that for initial terminal design, 2D simulations can still be used to gather quick visualization of the crimp shape.

Implementation of numerical simulations in the analysis of wire crimp is increasing also due to the robustness and significant improvements in computational software. With the implementation of new material and interaction models into FEA software, it is possible to achieve better control of the simulation progress. These simulations serve as a development tool for terminal design, allowing to minimize the number of real experimental tests needed. For numerical simulations, two main types of algorithms are typically used: implicit and explicit. The implicit algorithm is more commonly used for static and quasi-static problems, while the explicit algorithm is reserved for dynamic analyses. As the crimping process is dynamic and involves a high number of complex contact interactions, accompanied by high deformations, an explicit algorithm would be more efficient [22]. Study [23] presents a comprehensive overview of the crimping simulations as an explicit dynamic analysis. This approach gave a reliable method for evaluating the crimping process via numerical simulations, enabling engineers to investigate the impact of different parameters in the crimping process in a controlled virtual environment. As the real crimping process takes no longer than 0.3 seconds, the aim of such simulations is to increase the understanding of the mechanics involved in crimping, without involving new technologies, that could not be achieved by regular experimental investigation only [11,24]. This can lead to improved crimp and tooling specifications, and as a result a crimped terminal with predefined mechanical properties [25].

Metal forming processes have been the part of numerous investigations due to its widespread application in different industries. Crimping as a reliable method for creating a mechanical connection between wire strands and terminal, represents a plastically deformed metal to it final shape. During crimping process, terminal is compressed by crimping tools. Due to this, crimping simulation can be evaluated as part of the metal forming process and considered a subset of metal forming. Implementation of knowledge gathered from metal forming investigations would help in better performance of wire crimping simulations. Researches in work [26] investigated the sticking phenomena in cold forging of aluminium billets, evaluating the influence of contact pressure, plastic strain and sliding velocity. A significant number of papers [27,28] have been focused on springback effect, constitutive models and the coefficient of friction (COF), all of which are critical parameters influencing the crimping process [29]. For instance, the COF plays a significant role in determining the interaction between the crimping tool and the terminal. The lower the COF is, the deeper terminal wings will get into the wire strands. Some crimping simulations studies are suggesting a value of 0.1 [18], while others recommend higher values to simulate more accurate results [1]. Advancements in

simulation technology allowed implementation of micro-scale surface changes in friction models [30,31], which improved the accuracy of the numerical simulations. By considering local adhesion [32] and ploughing effects, these models have provided more realistic COF values under normal loading conditions, in between 0.13 and 0.145 [33]. Those values were interpreted as expected in another research [34]. Friction in metal forming is a local phenomenon, influenced by the contact conditions [35] and material itself [36,37]. A multi-scale friction model for coated sheets in the boundary lubrication regime has been developed [38], taking into account the physical behaviour of the coating and measured surface topographies of the sheet and tools [39]. The model uses a micro-scale ploughing model at each contact patch to determine friction force and the overall coefficient of friction. Authors Karupannasamy et al. have developed a model to describe the friction behaviour and deformation of surfaces for loading/reloading conditions [40]. In the automotive industry, friction modelling has evolved to include advanced friction models that account for the surface texture changes on the micro-scale, influenced by normal loading and stretching during forming processes [41,42]. Authors Doca et al. have extended a multibody frictional mortar contact formulation to address the simulation of solids experiencing finite strains with inelastic material behaviour [43]. That approach integrates finite strain modeling, frictional contact numerical treatment and finite element technology. It is based on dual Lagrange multipliers and a primal–dual active set strategy for robust and efficient analysis of metal forming problems. Despite the development of sophisticated friction models, there are still challenges in fully understanding friction behaviour under various contact conditions in metal forming processes [44]. The accuracy and efficiency of friction models, their implementation in numerical simulations and experimental validation require further work to improve predictability [45]. Implementation of complex friction models would also have impact on a computational time. Newly developed visco-mechanochemical interactive friction model has accurately predicted the transient tribological behaviour of the lubricant under changes in temperature, load and sliding speed. In another research authors Seitz et al. applied a semi-smooth Newton method to orthotropic plasticity and frictional contact at finite strains [46]. It offered a robust numerical approach for solving non-smooth and non-linear problems in metal forming processes. This method improved the computational efficiency and convergence, which enabled more accurate simulations of the contact behaviour between tools and workpieces under complex loading scenarios. The application of Arbitrary Lagrangian-Eulerian (ALE) finite elements to a lubricated friction model in sheet metal forming was also

investigated [47]. This approach evaluated lubricant's behaviour, considering its impact on the frictional forces during the forming process. Authors Krstulović-Opara et al. introduced a novel approach to 3D finite deformation frictional contact problems by developing a C^1-continuous formulation. This method applies a smooth triangular frictional node-to-surface contact element, significantly increasing the accuracy and stability of contact simulations. Another investigation was related to the smoothing of discretized surfaces with the application of Nagata patches in 3D frictional contact problems [48]. This technique improved the representation of contact surfaces, reducing the computational errors associated with surface discretization and enhancing the accuracy of contact and friction models. The measurement of Contact Potential Difference (CPD) during the adhesion process gave insights into the adhesion mechanisms during metal forming [49]. Improvements in tribotesting for sheet metal forming were achieved by developing more representative test methods, that better represent the actual conditions during forming processes [50]. These improved tests provided more accurate friction data, which could be directly applied to increase efficiency of finite element simulations of wire crimping process.

Material springback has been studied in the field of sheet metal forming, where the elastic recovery of a material leads to deviations from the desired geometry shape. Springback is also observed in wire crimping, but there have been no significant improvements in addressing this issue in that area. This elastic recovery or springback is influenced by various material properties and forming parameters [51,52]. They have been studied to improve the accuracy of formed parts and to reduce the need for iterative tooling adjustments. In the domain of sheet metal forming, V-die bending is a process where a sheet of metal is pressed into a V-shaped die to create an angle. This process is highly affected by springback, which results in elastic recovery after unloading and leads to unwanted geometry [53]. Regarding to numerical simulation improvement, researchers proposed an explicit to implicit finite element method, that significantly improved springback prediction. This explicit-implicit approach showed good match with experiments, where numerical predictions were within 1% of actual production values [54]. Similar investigation presented the importance of boundary conditions and the balance of constraints in achieving robust and accurate solutions [55].

In the study by Dilip Kumar et al. the L-bending operation's impact on aluminium sheet metal was examined, with focus on the spring back and thinning [56]. Methodological test of variation of sheet thicknesses and punch-to-die showed a linear increase in spring back and

thinning beyond specific clearance thresholds. In incorporated surface wear observation at lower clearances through scanning electron microscopy (SEM) analysis. In multi-stage rotary draw bending of thin-walled tubes, the homogeneous anisotropic hardening model offers a refined prediction of springback phenomena [57]. In the deep drawing of steel sheets, numerical simulations were validated in order to reduce the springback with different tool profile and blank holder force [58,59]. experimental and numerical investigation of the spring back of double-curved sandwich sheets showed the impact of sheet thickness and tool curvature radii on spring back [60]. In a separate study authors Esener et al. [61], evaluated the anisotropy of automotive sheets and its impact on stamping formability, presenting the importance of material properties in predicting spring back.

One of the challenges in simulating the crimping process is to accurately define material behaviour. This means setting up the appropriate constitutive model for the terminal and wire strands, which will be highly deformed. It was shown that material behaviour is having significant influence in metal forming. Elastic-plastic behaviour and anisotropic characteristics are important factors to predict the final shape of a product. The study of plastic anisotropy and its accurate representation in constitutive models for numerical simulations is unavoidable for predicting the behaviour of sheet metals in different forming processes. Numerous researchers were contributing to the development of theoretical frameworks, experimental investigations, and numerical implementations. In the context of material microstructure, research by Liu et al. on magnesium alloy revealed that rolling process significantly affects the microstructure. After rolling, alloy showed anisotropic behaviour with different tensile properties in various directions [62]. Numerous studies on the microstructure and mechanical properties of aluminium alloys made by rolling process have shown the relationship between rolling, microstructure and anisotropic mechanical behaviour [63]. These contributions collectively improved the understanding and predictive capabilities of anisotropic plasticity models in metal forming applications [64,65]. Chahaoui et. al. in work [66] compared associated and non-associated flow rules for stainless steel forming. They presented quadratic and nonquadratic orthotropic flow functions, demonstrating that non-associated flow rule approach provided better match with experimental data. The finite element formulation based on non-associated plasticity for sheet metal forming can capture complex behaviour of materials during forming operations [67]. With the theoretical advancements, an improved analytical description of orthotropy in metallic sheets has been proposed. This work enhances the predictive capabilities of yield criteria by incorporating prediction of directional yield stresses and *r*-values

parameters [68]. The dynamic response of materials, particularly the evolution of the Lankford coefficient at different strain rates, has also been a subject of interest. Research focusing on materials such as AA6016-T4, DP800, and DC06 provides insights into the strain rate sensitivity of anisotropy parameters, which is crucial for high-speed forming and impact scenarios [69]. Experimental investigation plays a crucial role in constitutive modeling, as seen in studies that examine the hardening behaviour of 5754O aluminium alloy sheet under two-stage loading [70]. Such research aims to capture the complex stress–strain response of materials subjected to non-monotonic loading paths, which are common in industrial forming processes. The finite element implementation of orthotropic plasticity models for sheet metal in low velocity impact simulations represents the practical application of these theoretical and experimental findings [71]. By incorporating material anisotropy into numerical models, is possible to predict the behaviour of aluminium plates during impact, considering the effects of non-linear isotropic/kinematic hardening [72]. The influence of anisotropy on the cold bending of S600MC sheet metal underscores the directional dependence of mechanical properties due to crystallographic texture induced by rolling [73]. The research utilized uniaxial tests and Digital Image Correlation (DIC) techniques to capture surface strains, constructing an anisotropic material model for numerical simulation validation [74]. Enhancing the understanding of material behaviour, the mechanical characterization of the elastoplastic response of C11000-H2 copper sheets in work [75] provided insights into the orthotropic non-associated Hill-48 criterion with a modified Voce hardening law. This study emphasized the need for numerical simulations to capture the complex triaxial stress and strain patterns that develop in the post-necking regime. The numerical determination of forming limit curves (FLCs) of anisotropic sheet metals using the Gurson-Tvergaard-Needleman (GTN) damage model, as investigated by researchers Kami et al. [76], has shown GTN model implementation in finite element simulations and validates the numerical results against experimental data, demonstrating the model effectiveness in predicting formability. The authors Marth at. al. [77] introduced a novel Stepwise Modelling Method (SMM) for characterizing post-necking behaviour of anisotropic sheet metals, extending its application beyond isotropic materials. By integrating the Barlat Yld2000 criterion [78], Džoja et al. accurately predicted the flow stress of presented aluminium alloy 5754-H22. Their approach involved determining sixteen anisotropy parameters using selected experimental data through an error minimization technique, which enabled precise predictions of uniaxial plastic material behaviour up to the point of fracture. The texture evolution and plastic strain ratio (*r*-value) anisotropy in Ta-2.5W

alloy sheets under varying rolling reductions are investigated [79]. It reveals that increased rolling reduction leads to a decrease in *r*-value and an increase in anisotropy, affecting deep drawing properties. The research establishes a predictive model correlating microstructural evolution with macroscopic *r*-value, providing insights into the material's formability. Based on the examination of the crystallographic texture, it is observed that the evolution of texture with the progression of plastic deformation in uniaxial test experiments influences the alteration of the Lankford coefficient [80,81]. Numerical analyses, such as those presented by authors Cvitanić et al. [83], have assessed the accuracy of evolutionary anisotropic plasticity models. The study introduced constitutive models based on the quadratic Hill (1948) and non-quadratic Karafillis-Boyce (1993) function. These models incorporate anisotropy parameters that evolve with plastic strain, enabling a more precise representation of the material's response under stress. Additional, Cvitanić et al. [82] made significant contributions by proposing algorithmic formulations for evolutionary anisotropic plasticity models based on non-associated flow rules. They focused on the distortion of the yield function/plastic potential with ongoing deformation, adjusting anisotropy parameters to data related to yield stress ratios and *r*-value evolutions.

The study of thermal plasticity deals with relations between temperature rise and the plastic deformation of materials [83]. Authors Taylor et al. [84] introduced the “latent energy” concept to describe the energy storage in material and its behaviour during deformation. New experimental investigations and thermodynamic descriptions provide a better understanding of the energy balance in materials under load [85]. To quantify the energy stored in alloys during deformation by performing mechanical tensile test, specimen surface temperature was measured with infrared camera or thermal probes [86–88]. Authors Pottier et al. [89] have presented a novel methodology for determining the inelastic heat fraction in materials, by a combination of full-field measurements and inverse Finite Element Updating (FEU). This approach improves the understanding of metal thermoplasticity, by identifying material parameters and strain-dependent heat fraction models. Based on some researches it can be noted that copper alloy mechanical properties depends on strain rate [90–92]. A higher strain rate is needed to achieve adiabatic process during experimental testing. Advancements in mechanical testing have been improved by combining two different techniques, such as Infrared Thermography (IRT) [93] and Digital Image Correlation (DIC) method. These methods have improved the understanding of deformation and fracture processes on complete specimen surface, not just at certain points. It offered a new view in terms of understanding

material behaviour under stress [94]. Authors Sendrowicz et al. [95] present another approach in combining these techniques, with the goal of improving the conventional mechanical tests and providing a detailed characterization of material responses. DIC and IRT methods were also combined in investigation of thermomechanical behaviour of coarse-grained aluminium multicrystals. It demonstrated the efficiency of these methods in evaluating microstructural-scale phenomena, which was used for the development of constitutive models for crystalline plasticity [96]. Authors Krstulović-Opara et al. [97] compared infrared thermography with 3D DIC in mechanical testing, evaluating their efficiency in detecting yielding processes in metals. Point where temperature will start to increase is just after the material yielding. Robustness of IR thermography for complex structures and the superiority of 3D DIC at lower loading velocities was also proven. Another technique, which represents improvement by applying phosphor pattern when combined IRT and DIC, to simultaneously capture full-field surface strains and temperatures with higher accuracy [98]. Authors Tretyakova et al. [99] present a correlation between strain localization and temperature fluctuations during plastic deformation for complicate loading condition. One of the challenging part, when referring to DIC, is capturing images with low exposure time in order to gain sufficient number of frames per second for high speed experimental test [100,101]. Based on the experimental data [102], numerical models were developed with constitutive models describing thermomechanical behaviour of material under stress [103,104]. Validation of numerical models through DIC and thermography has been presented in several works data [105–107].

Deep drawing is a metal forming process widely used in the manufacturing for producing hollow-shaped components with various geometries [108]. The process involves the plastic deformation of a sheet metal blank into a die cavity, thus forming a cup or box-like structure without being fractured [109,110]. The deep drawing process is influenced by different factors, like material properties, tool geometry, lubrication, and process parameters like applied force [111] at different velocity. All these parameters would have impact on the final quality of the product. A considerable number of research has been written to understand and optimize these factors to improve the formability of materials and to minimize defects. Most common defects in deep drawings are wrinkling, earing [112], springback [113] and at the end fracture [114]. The study of optimal die curvature in deep drawing processes improves the understanding of material flow and strain distribution and tool design optimization deep drawn product [115,116]. Various deep drawing tests are used for numerical model validation, wherein the final shape is being compared [117,118]. The prediction of Lankford coefficients for

aluminium sheets through uniaxial tensile tests and cup drawing experiments has provided a more comprehensive framework for anticipating material behaviour under various strain paths, contributing to the advancement of metal forming precision and efficiency [119].

1.3. Research hypothesis and objectives/present contribution

The thesis framework focuses on determining the optimal compression of wire strands in crimped terminals, with the goal of having terminals with predefined mechanical properties. This approach consists of the development of a finite element model that can accurately describe the crimping process. The numerical model should account for the complex interactions, at a high strain rate, between the wire strands and the terminal, including the effects of material plasticity, anisotropy in mechanical properties, thermoplasticity, frictional contact and springback.

To ensure the model's accuracy, it is crucial to validate the numerical predictions with experimental data. This involves conducting a series of crimping experiments under controlled conditions to measure parameters such as crimping force, terminal deformation, and wire strand compression. The experimental setup should be designed to replicate the conditions assumed in the numerical model as closely as possible.

The capability of the considered numerical formulation will allow the evaluation of the mechanical properties of the crimped terminal, with the final goal of the research to enable the production of terminals with predefined mechanical properties.

The work behind this thesis makes the following contributions to the field of numerical and experimental mechanics:

1. The strain rate effect on terminal and wires thermoplastic material behaviour in the case of large deformations will be defined.

2. Based on the experimental results, a numerical model for simulating the deformation process of the terminal and wire material will be proposed. This will enable more accurate numerical modelling of wire crimping process in relation to the existing models.

3. A validated numerical model of the wire crimping process will enable the production of a terminal with predefined mechanical properties.

Chapter 2

Wire crimping

This chapter presents the theoretical background regarding metal forming with a focus on wire crimping. The wire crimping process is widely used in the automotive industry. It is one branch of the metal forming process where the terminal is drastically deformed to the new shape, as shown in Figure 1. Due to the minimization of all parts in the automotive industry and new demands on reliability and safety, together with the applications of new materials and new production technologies, new studies must be made.

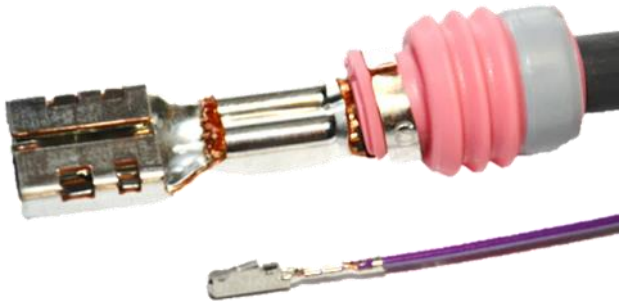

Figure 1. Two different samples of crimped terminals

2.1. Wire crimping process

The wire crimping process is the solderless procedure of making an electrical connection between wire strands and the terminal. It involves the deformation of a metal terminal, known as a crimp barrel, around wire strands to create an adequate electrical and mechanical connection. This method of crimping terminals mechanically rather than ultrasonically or

electromagnetically is still preferred in the automotive industry. The mechanical crimping process is characterized by its efficiency, reliability, and repeatability, making it a preferred method for achieving good connections. The success of wire crimping relies on the base terminal design for a specific wire size accompanied by adequate crimping tool shape and specified parameters. In case everything is aligned, the new crimped terminal will have good mechanical and electrical performance.

Wire crimping can be categorized into two different types: open barrel and closed barrel crimping, as shown in Figure 2. Open barrel crimping involves a "U" shaped terminal into which the wire strands are laid before the sides of the terminal are folded over to secure the wire crimping tool shape, which will prevent wire strands from coming out of the open barrel. Closed barrel crimping, on the other hand, requires the wire to be inserted into a pre-formed cylindrical barrel, which is then deformed around the wire. Usually, crimping tools will press cylindrical barrel symmetrically from at least 2 sides. Each type has its advantages and challenges, and the choice between them often depends on the specific requirements of the application, including the need for automation and the desired reliability of the connection. In general, for low voltage applications, open barrel is used more often, while for high voltage and high-speed data (HSD) applications, it is more common to have closed barrel crimping.

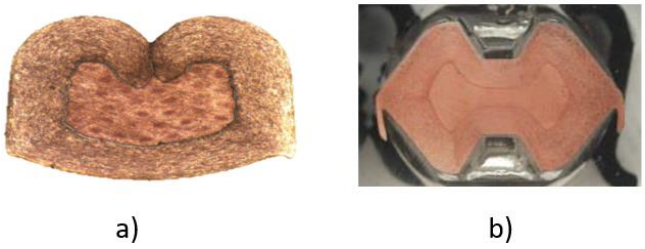

Figure 2. Cross sections of a crimped a) open and b) closed barrel

Due to the wire and terminal compression, an air-tight seal is generated that prevents corrosion and ensures a large contact surface area. This leads to low electrical resistance and good mechanical strength, which are crucial for maintaining the integrity of the electrical connection over time. To ensure the quality of crimped connections, monitoring techniques such as crimp curve monitoring are employed. This involves analysing the force and displacement curves generated during the crimping process to detect any anomalies that may indicate a defective crimp [120].

2.1.1. Terminal design

Considering the mating with the opposite side, there are two types of terminals, male and female terminals. Each terminal consists of a contact area; in the case of a male terminal, it is called a blade. The female terminal contact area is more complex, usually a box shape, which consists of a deformable spring to achieve electrical contact with the opposite male terminal's blade. On the other side of the terminal, there would be terminal wings for crimping. Every terminal has at least one set of wings for crimping wire strands and achieving mechanical and electrical connection and, optionally, another set of wings for crimping wire insulation for mechanical connection. An example of male and female terminals is shown in Figure 3.

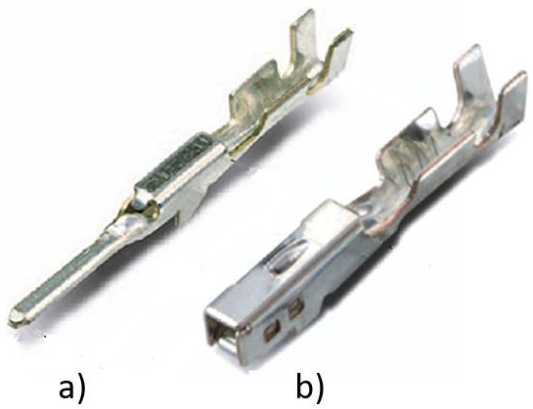

Figure 3. Uncrimped a) male and b) female terminal

When defining terminal base material there are several points to consider:

1. Electrical conductivity

   As the terminal is a crucial component in current flow, copper or its alloys are the logical choices for terminal base material. Pure copper has a high electrical conductivity of 58 MS/m, while copper alloys like CuFe2P have 35 MS/m, which is 40% less.

2. Strength and formability

   Strength is an important factor in achieving good contact force between crimped terminal and wire strands, but also between the male blade and female terminal spring. For instance, pure copper temper classes are in range from R220 (UTS 220-260 MPa) to R360 (UTS 360-410 MPa), which is not adequate in most cases. Additionally, minimum guaranteed elongation (A_{50mm}) will drop from 33% for R220 to only 2% for R360. Low elongation would have an impact on formability, and that is one of the

reasons why copper alloys are used. For reference, copper alloy CuFe2p R370, with almost the same strength, would have a minimum elongation of 8%.

3. Stress relaxation performance

   The property of a material to persist with remaining stress level under constant deformation at increased ambient temperature in a defined time is called stress relaxation performance. In general, pure copper (Cu-ETP) has low stress relaxation performance, while some copper alloys like CuFe2P have good performance even at higher temperatures like 150°C. As shown in Figure 4, at 150°C, the material retains approximately 70% of its initial stress after 100 hours and about 60% after 1000 hours, demonstrating its relatively strong stress relaxation performance under elevated temperature conditions.

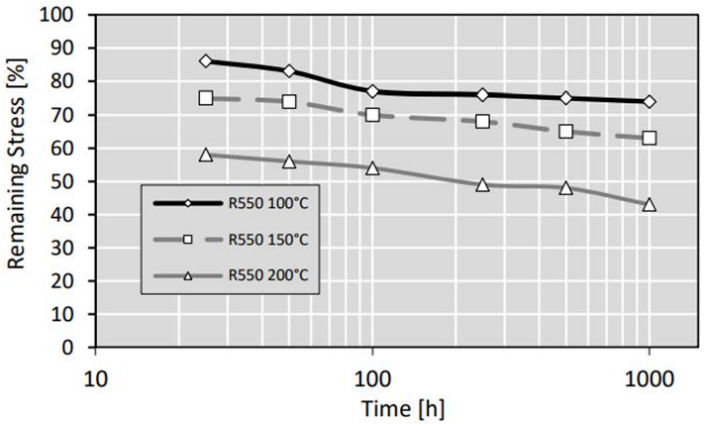

Figure 4. Stress relaxation curve for Cufe2P [121]

4. Corrosion resistance and plating compatibility

   Copper's natural ability to resist corrosion contributes to the longevity of the electrical terminals, when compared to aluminium and its alloy. When additional protection is needed, especially in high-humidity environments, a tin surface plating is applied. In case of need for a terminal for higher temperature application, above 125°C, silver or gold plating will be applied.

An overview of the mechanical and electrical properties of copper and its alloys is presented in Figure 5. It can be noted that with the increase of tensile strength, there would be an almost proportional decrease in electrical conductivity.

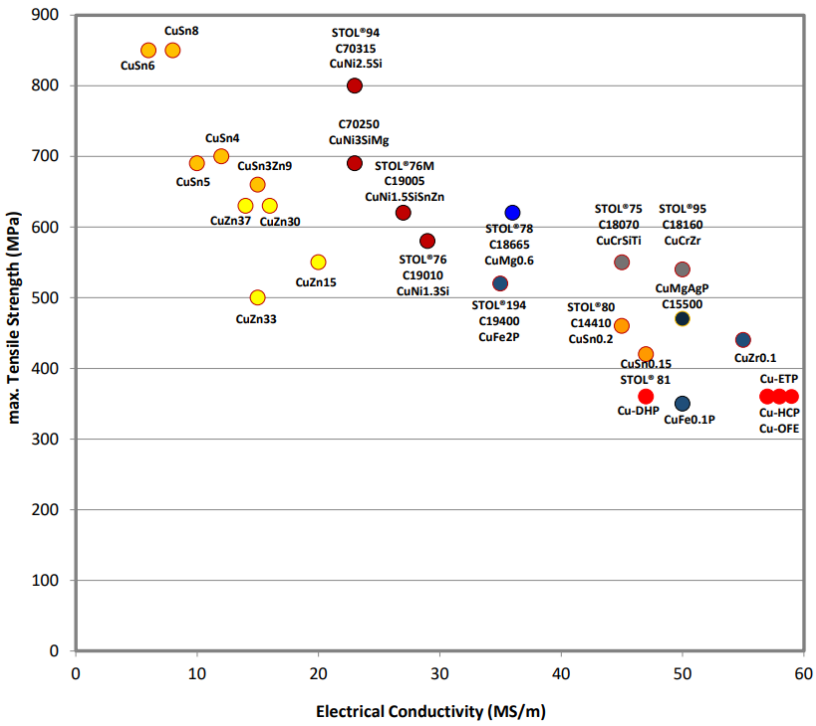

Figure 5. Mechanical and electrical properties of copper and its alloys [121]

When designing a terminal, material thickness is also one point which is considered. It should be optimized to balance the needs between structural integrity and material cost. Thinner materials can reduce costs and improve flexibility, but they may also compromise the terminal's strength and its ability to maintain a secure connection over time in harsh environments.

2.1.2. Wire size and type

Each terminal is designed to accommodate a wide range of wire sizes, with different numbers of strands and strand diameters. During the terminal crimping of different wire sizes, terminal wings must envelop and compress all wire strands without damaging them, to ensure good mechanical and electrical contact. Serration design in terminal conductor wings must be optimized to prevent wire slippage and to increase contact pressure to achieve good electrical contact [23].

The most common material for wire strands is pure copper, but for some applications, copper is alloyed with materials like tin, magnesium, iron or silver. The reason for that is to increase the tensile property of wires with small cross-section areas like 0.13 mm^2. Lately, aluminium wires have also been introduced into the automotive industry due to their low density and lower cost per kilo. Although, they have the disadvantage of lower electrical conductivity, strength and corrosion resistance.

2.1.3. Crimping tools

The crimping tool function is to deform terminal wings over wire strands or insulation with a defined stroke to the final shape, which is equivalent to the shape of the crimping tools. For each terminal set of wings, a corresponding set of crimping tools is required. The upper tool is called a wire or insulation crimper, while the bottom tool is called a wire or insulation anvil. Crimping tools are made of hardened steel to reduce wear and increase lifetime. The surface of the crimping tool, which comes into contact with the terminal, is polished to have a lower coefficient of friction. These sets of crimping tools are positioned into the applicator, a mechanism which is pushing crimping tools and cutting the terminals from the strip in one stroke. Each applicator has the possibility to adjust the crimp height via an adjustment head. With different sets of crimps height, it is possible to achieve different values of wire strand compression. The wire crimping applicator produced by the company Mecal is shown in Figure 6.

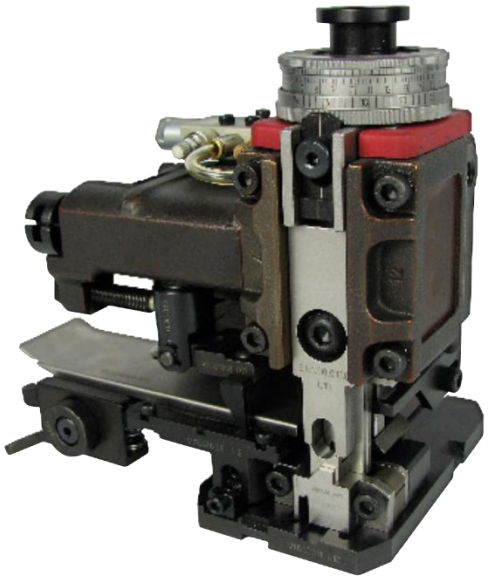

Figure 6. Wire crimping tools positioned inside the crimping applicator

Applicators are positioned inside crimping machines, an eccentric press which is pressing the applicator head with constant stroke. There are two types of crimping machines: manual and automatic as shown in Figure 7. Manual crimping machines are operated by human operators, who need to manually position the wire inside the terminal wing and press the pedal, after which the machine will crimp the terminal. These types of machines are used for low-volume

series as they are more time-consuming, and the final product strongly depends on the operator. On the other hand, automatic crimping machines will automatically strip the wire, position inside the crimp and crimp it. The operator only needed to observe the process in case of some malfunction.

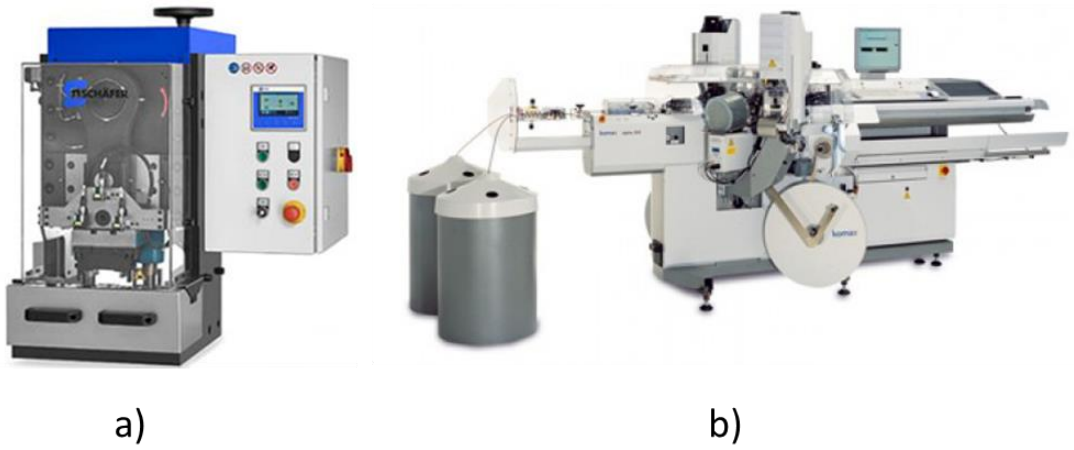

Figure 7. Wire crimping machine types a) manual and b) automatic

2.1.4. Process Efficiency and Quality Assurance

During crimping, there are some unwanted scenarios, which can be seen in Figure 8. To overcome those issues, crimp force analysers are integrated into crimping machines to provide real-time feedback on the crimping force applied during the process. As there is no influence of the operator on wire positioning, most of the automatic crimping machines are equipped with these types of monitoring systems to detect if some oscillations in the force-path curve have occurred.

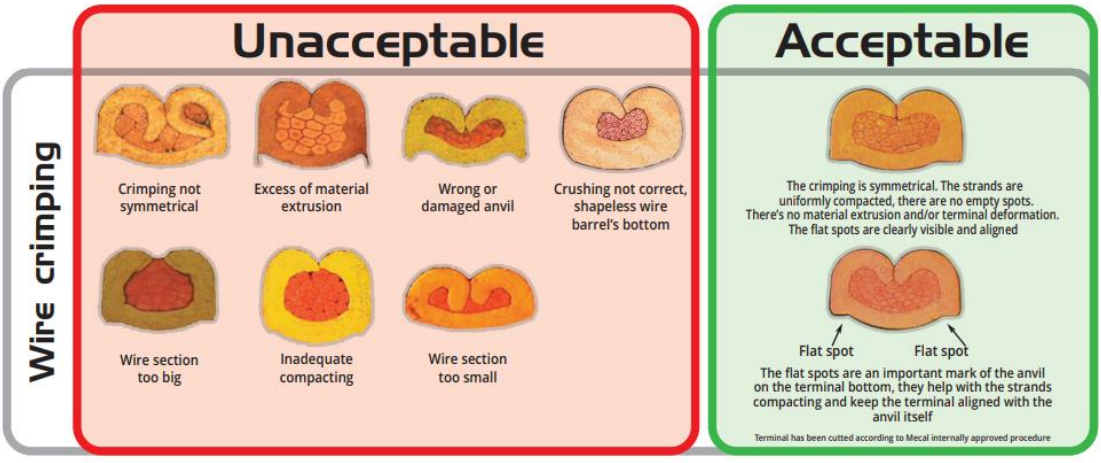

Figure 8. Acceptable and non-acceptable crimp cross-sections [122]

There is a specially developed algorithm according to which crimp force-displacement curve is divided into several zones for better detection of scrap products [120]. The implementation of machine learning techniques, particularly deep learning, offers a promising avenue for inline quality monitoring of crimping processes. By analysing process curves generated during crimping, algorithms can learn to identify patterns associated with both acceptable and defective crimps, as shown in Figure 9. Line R represents the normalized force of a regular crimp, while line E represents an empty crimp, without wire strands, during the defined stroke. The graph is divided into three zones: Z1, Z2 and Z3. These zones are used for algorithm evaluation and detection of anomalies by calculating the area difference of each zone. This approach facilitates the automation of quality control, allowing the real-time monitoring of each wire crimped connection during production [123].

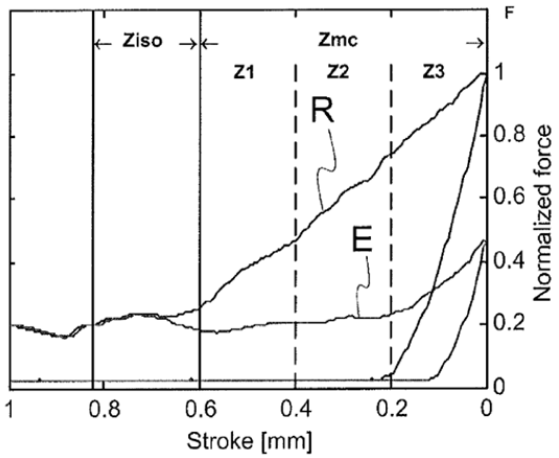

Figure 9. Crimp force-stroke diagram divided into several zones for algorithm interpretation [120]

2.2. Material anisotropy in terminal production

Materials used to manufacture the terminals, such as copper sheets and their alloys, often have anisotropic properties due to the way they are produced. The raw material used to produce terminals is a strip which is obtained by rolling, a process where the copper plate is passed through a series of rolling mills, one rolling mill from the upper and one from the bottom side. The rolling mills will plastically deform material to its new thickness and also change the grain morphology. Due to the initially random orientation of crystal grains, the material will be nearly isotropic. However, as deformation progresses in the rolling process, these grains reduce size and elongate along the direction of maximum strain and adopt a preferred orientation, which leads to anisotropic behaviour. Despite the fact that copper alloys are widely used in the

automotive industry, wherein a lot of optimizations are required, according to literature research, no study has considered copper alloys anisotropy.

Terminal, which is produced from a copper alloy strip, would have orientational dependent mechanical properties like yield, tensile strength and ductility. In production, terminals are stamped from metal strips in a way to optimize the terminal position on the strip to reduce the material scrap, as shown in Figure 10. This means that terminal wings can be positioned in different orientations, and even for the same terminal wing design, different performances can be expected due to anisotropy. For this reason, it is important to consider the influence of terminal orientation on the metal strip with numerical simulation of the crimping process.

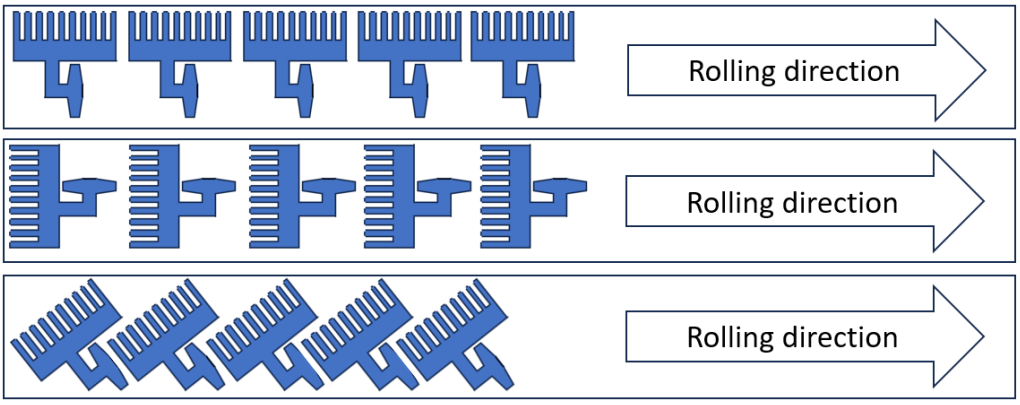

Figure 10. Different terminal positions for stamping on the metal strip

Chapter 3

Measuring methods

3.1. Tensile test machine

Tensile test machines are essential tools in material science and engineering, providing valuable insights into material behaviour under tensile loads. Standard output of tensile test machine during measurement are force and displacement over some period of time. The primary components of a tensile test machine include a load cell to measure the force applied to the specimen, grips to hold the material in place, and a mechanism, typically a hydraulic actuator or screw-driven system, to generate the tensile force. Each tensile test machine has its limits in maximum force, displacements and speed. In general, screw-driven grips can achieve lower speeds, while hydraulically actuated ones can achieve higher speeds, which are needed for some dynamic tests.

In a standard uniaxial tensile test, the specimen is carefully positioned between two grips, ensuring proper alignment to avoid bending stresses and rotations. One grip is fixed, while the other is moving away from the fixed one. After positioning, the specimen is pulled apart with a defined stroke and speed. Based on the specimen length and speed, the strain rate can be calculated. The load cell continuously records the force during the measurement, while the elongation is measured by internal machine mechanism as displacement of the grip. This data is then used to calculate material properties, such as yield and ultimate tensile strength and elastic modulus.

There is one issue with usage of only tensile test machine for material evaluation, it is the way displacement is being measured. As displacement is measured internally, in best case it would represent displacement of the grip. During testing, there are always some displacements that cannot be excluded, such as slippage in grips and even the stiffness of the complete machine frame. This error in results can easily be seen in the measurement of elastic modules, as the force is constantly increasing and unwanted displacements will occur, which would result in lower elastic modulus. For that reason, different types of extensometers are used to measure correct displacement. In this work, experiments were done on servo-hydraulic tensile test machine Instron 8801 and screw-driven ZwickRoell Z010, displayed at Figure 11.

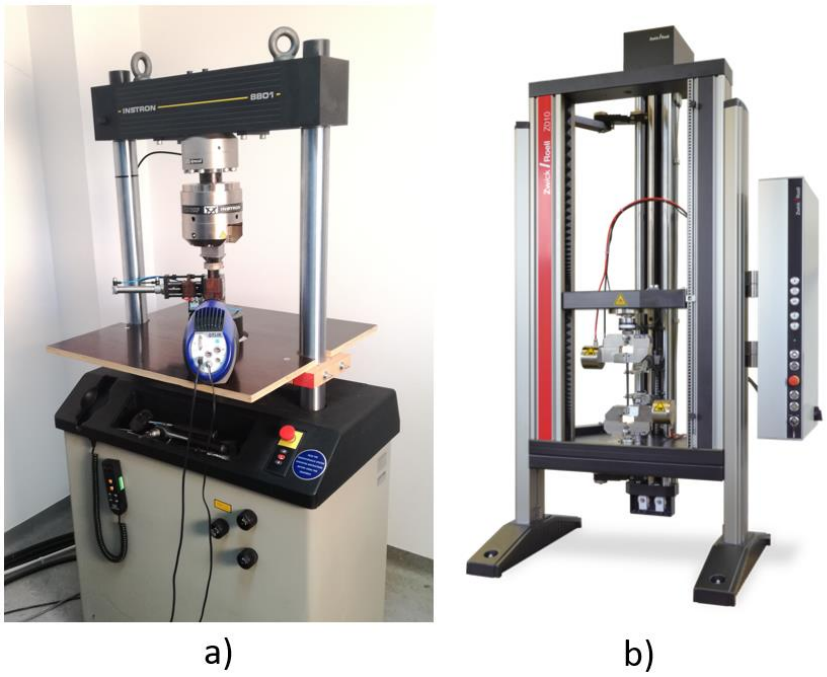

Figure 11. Tensile test machines a) Instron 8801 and b) ZwickRoell Z010

3.2. Mechanical extensometer

Mechanical extensometers are used to measure relative displacement between two defined points of a specimen during tensile tests. For uniaxial tensile tests, most commonly, longitudinal and lateral extensometers are used to measure the strains. As the deformation is ongoing, the extensometer tracks the longitudinal or lateral strain of the specimen in a real-time. Mechanical extensometers belong to a group of contact measuring devices, as they are physically clipped on the specimen. Due to measuring size limitations, they are not applicable for specimens with higher elongation. When the extensometer output signal is connected to a

tensile test machine interface, force, displacement and strain data will be automatically synchronized.

The use of mechanical extensometers with tensile testing machines is a well-established practice in material characterization. One of the advantages of mechanical extensometers is their reliability, robustness and low time consumption for data processing. With a longitudinal mechanical extensometer, it is possible to determine and generate stress-strain curves based on which yield strength, elastic modulus, tensile strength and elongation can be obtained with high confidence. There is also a possibility to combine longitudinal and lateral extensometers together on the same specimen. With that approach, the calculation of the *r*-value (Lankford coefficient) for the evaluation of plastic flow anisotropy can be done. In this work, longitudinal extensometer EPSILON 3542 and lateral extensometer EPSILON 3575AVG-ST were used as shown in Figure 12.

Figure 12. Tensile test specimen with longitudinal and lateral clip-on extensometer

3.3. Digital image correlation (DIC) and Aramis 4M

Digital image correlation was developed in the early 1980s at the University of South Carolina to measure the deformation and displacement of bodies subjected to load. This method does not require physical contact with the measuring body, but by using high-resolution cameras it is possible to monitor changes of the surface on the measuring body. Although standard tests at the macroscale provide useful information related to the material, this is not sufficient

because many changes occur at the micro- or nanoscale. For this reason, DIC is widely used in material testing.

DIC was proven to be very effective in detecting deformations in microscopic mechanical examinations, where a stochastic pattern is directly applied and thereby provides the necessary contrast in order to measure surface deformation. This non-contact, full-field technique captures the surface texture of a specimen using a series of images taken before, during and after deformation. The working principle of DIC involves dividing the images into small regions, known as facets, and finding the corresponding facets in the subsequent images by a correlation criterion. This process allows the determination of the displacement field by calculating the movement of each facet from its initial to its deformed position.

DIC offers significant advantages over traditional measurement techniques, such as mechanical extensometers. It provides a comprehensive strain field rather than point measurements, allowing for the analysis of strain localization and the detection of phenomena like necking or crack propagation. Just like the combined usage of longitudinal and lateral extensometer, DIC can also be used for the determination of *r*-value based on the longitudinal and perpendicular deformation. DIC is also not limited by fixed measurement area length as it can measure strain on the complete stochastic surface, which is captured by the camera lens. In the case of a non-standard test, where a mechanical extensometer cannot be positioned, DIC can still be used to record and process data.

For the purpose of this investigation, the optical measurement system Aramis 4M as shown in Figure 13, was used. The Aramis measurement system is a sophisticated optical system designed for the precise measurement of displacements and deformations across a variety of scales and material types. This system is capable of assessing both small and large objects, ranging from 1 mm to 2000 mm in size, using the same sensor. It can accurately measure deformations from as little as 0.01% up to 100%, providing a comprehensive field of displacement and deformation data across the surface of the object under examination. This makes Aramis an exceptionally powerful tool for validating numerical calculations in research and engineering applications.

Figure 13. Optical measurement system Aramis 4M

To have a clear image at higher load velocities, as exposition time will be short due to the high frame rate, an adequate external light source needs to be used. The standard light source from the Aramis 4M system, which consists of 2 LED light sources of 9W each, was not enough for the current study. Therefore, an additional LED light source was made, which consists of two 50W LED sources accompanied by a stabilized DC power supply, to prevent flickering. A lens with a polarization filter was mounted on LED chips to prevent light reflection during image recording. Additionally, for achieving higher frame rates only one camera was used. By using two-dimensional instead of a three-dimensional measurement, the system is capable of faster capturing and processing images.

The impact of the implementation of new light sources was tested with the light measurement tool Velleman DEM300. With standard Aramis 4M light, measured illuminance at the specimen surface was 2300 Lux, while with an additional light source, it increased to 7800 lux. This measurement is for reference only, test was performed as presented in Figure 14.

Figure 14. Illuminance with a) Aramis 4M integrated light b) additional 2 x 50W led light

3.4. IR thermal camera

Thermography is non-contact method for surface temperature measurements based on the infrared imaging to visualize the thermal profile of a specimen under stress. Similar and compatible to DIC stochastic pattern, optical and infrared camera can be used to monitor same specimen surface. With usage of thermography in tensile testing, it is possible to detect heat localization which may indicate potential necking and failure area. Also, when a material is stressed up to yield point, the camera would detect small temperature drop, but after material passes the yield point and starts to deform plastically, temperature will rise.

As IR thermography is a non-contact method that measures radiance, results and accuracy will depend on emissivity, ambient temperature, focus and other thermographic parameters. Prior to recording of the surface, it is needed to measure emissivity factor of the surface. The accuracy of IR cameras is ±2%, and for the specific model used in this research ±1% or ±1°C. For purpose of this work fast cooled middle wave InSb thermal camera IR camera FLIR SC 5000 was used, shown in Figure 15.

Figure 15. IR thermal camera FLIR SC 5000

With the usage of IR thermography, elastic deformation can be distinguished from plastic one. According to the first law of thermodynamics, for uniaxial case this equation can be used:

$$\rho c\dot{T} - k\frac{\sigma^2 T}{\sigma_x^2} = \beta\sigma\dot{\varepsilon}^{\mathrm{p}} - \alpha ET\dot{\varepsilon}^{\mathrm{e}} \quad (1)$$

where T is temperature, σ is stress, ε^{e} is elastic strain, ε^{p} is plastic strain, ρ is mass density, c is specific heat capacity, k is thermal conductivity, α is thermal expansion coefficient, E is Young's modulus and β is a fraction of the plastic work converted into thermoplastic heating. For the case of adiabatic conditions, at a higher strain rate and since the part related to thermoelastic heating $\dot{Q}^e = \alpha ET\dot{\varepsilon}^e$ is small compared to thermoplastic heating $\dot{Q}^p = \beta\sigma\dot{\varepsilon}^p$, the simplified equation would be:

$$\rho c_v\dot{T} = \beta\sigma\dot{\varepsilon}^p \quad (2)$$

Inelastic heat fraction (IHF) β can be expressed as

$$\beta = \frac{\rho c_v\dot{T}}{\sigma\dot{\varepsilon}^p}, \quad (3)$$

where c_v is the specific heat capacity at constant volume as the plastic flow is an isochoric process.

Non-contact methods like DIC and IR will provide more accurate results, as they are not in contact with the specimen. Conventional extensometer or strain gauge may locally increase stiffness and change stress distribution. Also, in combination with temperature probe heat flow may influence on temperature reading. DIC and IR methods have some limitations which are opposite to each other. The DIC method is more convenient at lower test velocities as exposition time can be longer, and blurred images will be eliminated. Optical measurement system Aramis 4M is limited by the frame rate which can go from 1 Hz up to 480 Hz. For higher frame rates, an adequate light source needs to be used, as camera exposition time would be lower. For infrared (IR) thermography, it is desirable to have higher velocities, as it will reduce heat dissipation, and the process will be closer to the adiabatic process. The quasi-static test can't be traced with the IR method, as heat will be exchanged with the ambient. The thermal camera used in this work has a frame rate limit of 700Hz, which is adequate for this investigation.

3.5. Computed tomography

Computed tomography (CT) is a non-destructive imaging technique that provides detailed 3D models and cross-sectional images of an object by utilizing X-rays. In manufacturing, CT can be used as a quality assurance method, in which dimensional accuracy of produced components can be made. In this work, the CT scan machine Werth TomoScope S shown on Figure 16 was used. With an *x*-ray tube output of 80 W and voltage up to 225 kV, this machine is capable to scan high density material like copper and its alloys. In this study, computed tomography was used to evaluate the crimped terminal and the shape of a cup obtained by deep drawing.

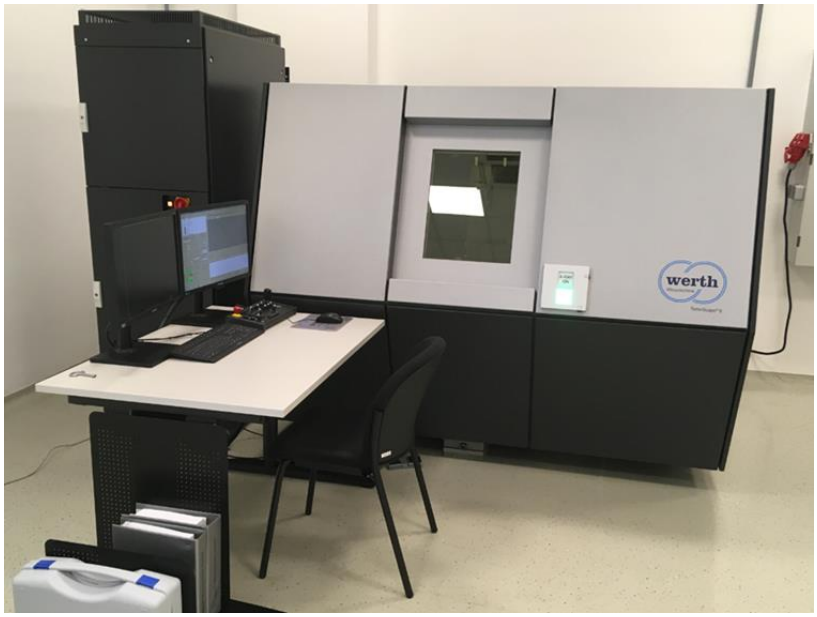

Figure 16. CT scan machine - Werth TomoScope S

Crimped terminals are used to connect end of wires to other electrical devices. The quality of the crimp connection is critical for ensuring electrical conductivity and mechanical strength. Traditional methods of evaluating crimp quality often involve destructive testing, where the terminal is cut to measure the degree of compression. With CT scanning these destructive methods can be exchanged with a non-destructive one. Default CT scanning output is 3D outer shape of the terminal, which can be overlapped by numerical model results of the crimped terminal. Another advantage of CT scan is capability to make crimp cross sections, without destroying terminal with mechanical cutting methods. The CT cross section images provide detailed information about the density and distribution of the material within the crimped area. As CT is based on material absorption of X-rays dependable on their density, it would be challenging to detect the difference between wire strands and terminal. According to the table 1., it can be seen that Cu-ETP (wire strands material) and CuFe2P (terminal material) have almost the same density and ability to absorb X-rays. The solution to this challenge is to use high-resolution CT scan magnification to capture Sn (Tin) plating, which is a few µm thick. Sn density is having approximately 20% lower density, which would be visible as a lighter outline which would divide terminal from the wire strands.

Table 1. Material density

	Cu-ETP	CuFe2P	Sn
Density [g/cm3]	8.92	8.91	7.31

By comparing the dimensions of the crimped section to the original dimensions of the terminal and wire, it is possible to calculate the degree of compression according to equation (4). This information helps in verifying if the compression ratio is at the desired level and to evaluate if the crimping process meets the crimping specifications.

$$\text{Compression ratio } [\%] = \frac{Cross\ section\ of\ deformed\ wire\ [mm]}{Cross\ section\ of\ undeformed\ wire\ [mm]} \times 100 \qquad (4)$$

With this approach, a sample of the crimped terminal, which was CT scanned, can undergo wire pull-out tests to evaluate the mechanical strength of the crimp connection. Since the CT scan would cause no damage to the terminal or wire strands, the pull-out test results would indicate the actual performance of the crimp in its intended application. With the conventional way of testing, this would not be achievable.

Deep drawing is a metal-forming process used to create hollow-shaped parts, such as cups. The final shape of the deep-drawn parts is influenced by material properties and process parameters. The presence of thickness reduction, earring, wrinkling and tearing can be easily determined and measured with a CT scan. Earring is a common defect in deep-drawn cups, characterized by the formation of uneven rims due to material anisotropy in plastic flow. CT scanning can be used to measure the height and distribution of the ears for a cup quarter. This can be achieved by measuring directly on 3D model generated from a series of cross-sectional images along the height of the cup. One of the aspects of deep drawing is controlling the thickness of the material to prevent tearing. CT scans allow for the measurement of wall thickness throughout the cup without the need for cutting the sample. The appearance of wrinkling and tearing on a cup is considered to be an inadequate sample for the validation of numerical models. In case of their appearance, with modification of parameters like blank holder force, punch velocity and even modifying blank diameter they should be overcome.

This work considers the cup deep drawing process as it serves as a widely accepted benchmark test for evaluating anisotropic plasticity constitutive models for sheet metals. Simulating this

process provides a robust method of validating the accuracy of these models, particularly in capturing the complex behaviour of materials during forming conditions.

Chapter 4

Experimental investigation

Summary

Performing experimental investigation of material behaviour is the first step in developing a reliable constitutive model for numerical simulations. In the wire crimping process, there are at least two different metal materials involved. Alloyed copper with improved tensile strength is used for terminals and pure copper is used for wire strands. This chapter presents a comprehensive experimental investigation aimed to determine the mechanical properties and deformation mechanisms of a pure copper Cu-ETP and copper alloy CuFe2P. The experimental tests are designed to capture the response of the material at different loads with different strain rates, which is crucial for a reliable numerical model for crimping simulations.

4.1. Tensile tests at different strain rates

Tensile testing is a fundamental approach to evaluate the material's strength and ductility. Tensile tests were conducted at different strain rates, starting from slow up to high-speed conditions. This variation in strain rates helps in understanding the rate sensitivity of the copper and copper alloy, which is important for applications subjected to dynamic loading.

In the wire crimping process, there are at least two different metal materials involved. Alloyed copper with improved tensile strength is used for terminals and pure copper is used for wire

strands. In this study, the mechanical behaviour of the copper alloy sheet CuFe2P was thoroughly investigated to understand its performance under various loading conditions. The chemical composition of the alloy CuFe2P is given in weight percent (wt%) in Table 2, according to the received supplier datasheet. The material used in this study, CuFe2P, was sourced from KME Germany GmbH as A4 size sheet metal plates.

Table 2. Chemical composition of CuFe2P

Element	Fe	Zn	P	Cu
Composition (wt%)	2.1 – 2.6	0.05 – 0.2	0.015 – 0.15	rest

Tensile test specimens were made of CuFe2P sheet with a thickness of 0.8 mm, specimen size was 135.4 mm x 24 mm x 0.8 mm (Figure 17). Each specimen was cut out using a wire EDM (Electrical Discharge Machining) which enables high-precision cuts following a defined contour. To characterize material anisotropy in mechanical properties, tensile tests were conducted on specimens whose longitudinal axes 1 are oriented at 0°, 45° and 90° relative to the rolling direction x.

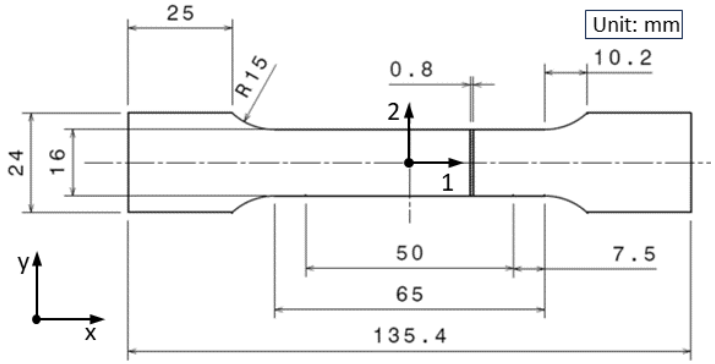

Figure 17. Tensile specimen geometry

Tensile tests were performed at four different strain rates, according to Table 2. This range of velocities was chosen to simulate the various strain rates that the material might experience during different stages of the crimping process. For the evaluation of the mechanical behaviour of tested specimens, a standard uniaxial tensile test was performed. This test method is widely recognized for its ability to provide fundamental material properties such as yield stress, ultimate tensile strength and elongation at break, which are essential for the design and analysis of crimped connections.

Table 3. Strain rates of uniaxial tensile tests

Strain rate (s^{-1})	0.0002	0.2	1	5.65

During loading the specimen surface temperature and strain were acquired by cooled middle-wave IR camera and ARAMIS 4M system. For additional confirmation of DIC method, the clip-on Epsilon longitudinal extensometer was used. System ARAMIS was synchronized with a thermographic camera in order to find a correlation between strain and temperature change. Due to DIC method requirements, test samples were painted with a stochastic pattern, i.e. black dots on a white background (Figure 18.). Here it is important to mention that paint of both colours must be of same origin, that means showing same emissivity in infrared spectrum. Based on these contrasting dots, Aramis 4M whose algorithm is based on the digital image correlation method, can calculate displacements of the dots during tensile test load. The influence of DIC pattern on the results is described in the works [124,125].

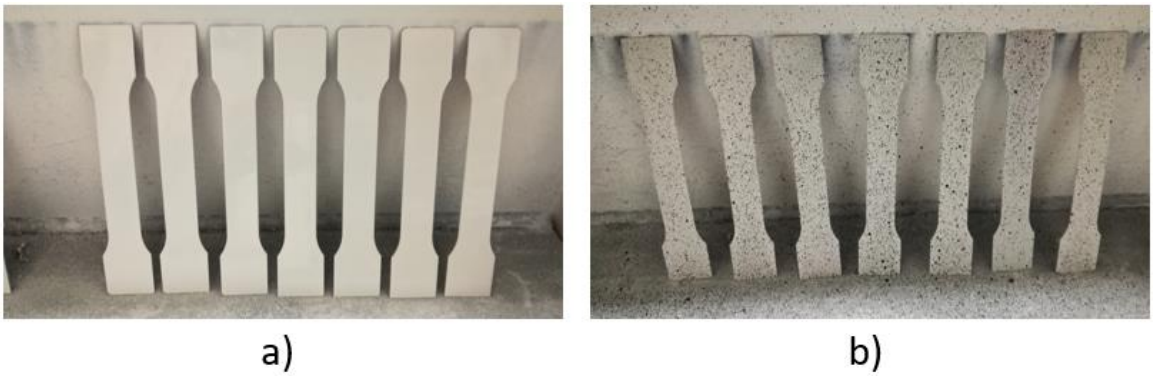

Figure 18. Application of stochastic pattern a) specimens with white background colour b) specimens with stochastic black dots

The optical system was calibrated before the measurement with appropriate measuring volume. The initial image, captured by an optical system, was at the unloaded stage and used as a reference image. The thermal emissivity coefficient for the used pattern was 0.85. The thermal emissivity is evaluated by a standard procedure where the specimen is at a uniform temperature, and emissivity is evaluated by comparing it with part of the surface covered with a layer of materials with known emissivity. This calibration process ensured that the temperature readings from the IR camera were reliable and accurate. The experimental setup for the uniaxial tensile test is shown in Figure 19.

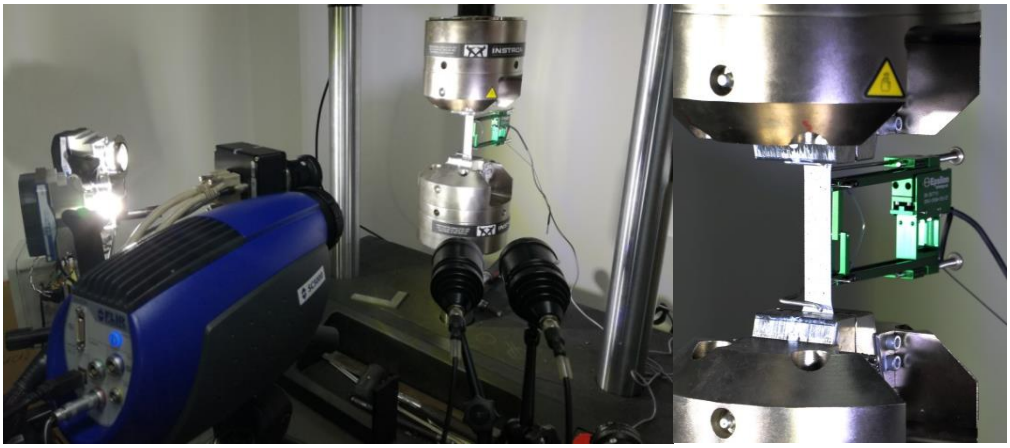

Figure 19. Experimental setup, uniaxial tensile test

For the estimation of elastic modulus, digital image correlation (DIC) was used. To have DIC results comparable to the clip-on extensometer, elongation was measured at the same points where the extensometer was clipped, as shown in Figure 20. The initial distance between these two measured points was 50 mm. Specimen orientation is defined with the axis 1 representing the longitudinal direction, the axis 2 the width and the axis 3 the thickness, as indicated in Figure 20. Within ARAMIS software, all images were discretized using square facets size 20 x 20 pixels with an overlap of 20 x 20%. Furthermore, the DIC sampling rate enables the determination of *r*-value at each increment of strain, capturing the evolution of anisotropy in plastic flow throughout the deformation process.

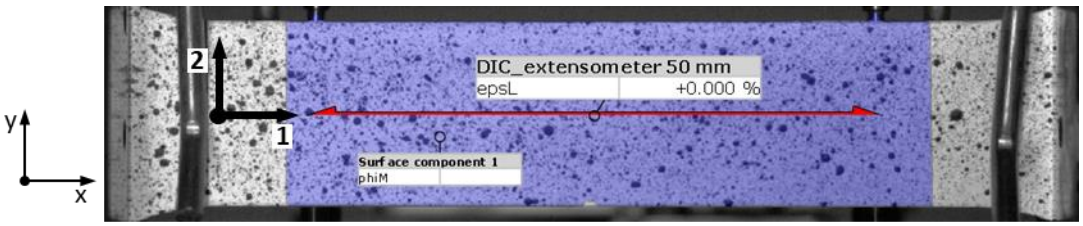

Figure 20. Location of elongation measurement points for DIC method at the same position where the extensometer is clipped on

To ensure the acquisition of high-quality images during high-load velocity experiments, where short exposure times are necessitated by elevated frame rates, an external lighting system was implemented. This system comprised of a two 50W LED air-cooled light source, each powered by a stabilized direct current (DC) power supply to maintain consistent illumination levels to eliminate flickering. To prevent the issue of light reflection, which can obscure critical details in the recorded images, a lens equipped with a polarization filter was mounted directly onto the LED chips. The polarization filter ability to reduce glare and unwanted reflections enhanced

the contrast and sharpness of the images, which lead to more accurate analysis of specimen surface.

First evaluation of the results is related to the data obtained from the tensile test machine and extensometer. An extensometer is a conventional tool used for evaluation of strain to determine elastic modulus. Due to the Aramis 4M recording frame rate limitation, the decrease in the number of recorded images can be observed as strain rate increases, as shown in Figure 21. It was found that extensometer is not appropriate measuring tool when thin specimens are loaded with higher velocities. Starting from the velocity of 50 mm/s (1 s^{-1}) and above wave form of the stress–strain curve in the elastic region can be seen. Only for tests performed with lower velocities 0.01 mm/s (0.0002 s^{-1}) and 10 mm/s (0.2 s^{-1}) waveform is not present and elastic modulus can be determined by using extensometer only. The point is that due to specimen thickness, extensometer readings are inaccurate for higher velocities. When a specimen is pulled with higher velocity, thin specimen starts to vibrate and with the increase of tensile test velocity vibrations are becoming more pronounced. After material starts to deform plastically, vibrations start to calm down. For higher velocities, a combination of clip-on extensometer and DIC was used for reconstruction of stress-strain curve. As DIC method demonstrates accurate results during elastic and plastic deformation, but has limitation in number of recorded images, use of clip-on extensometer increased number of usable points for newly generated stress-strain curve.

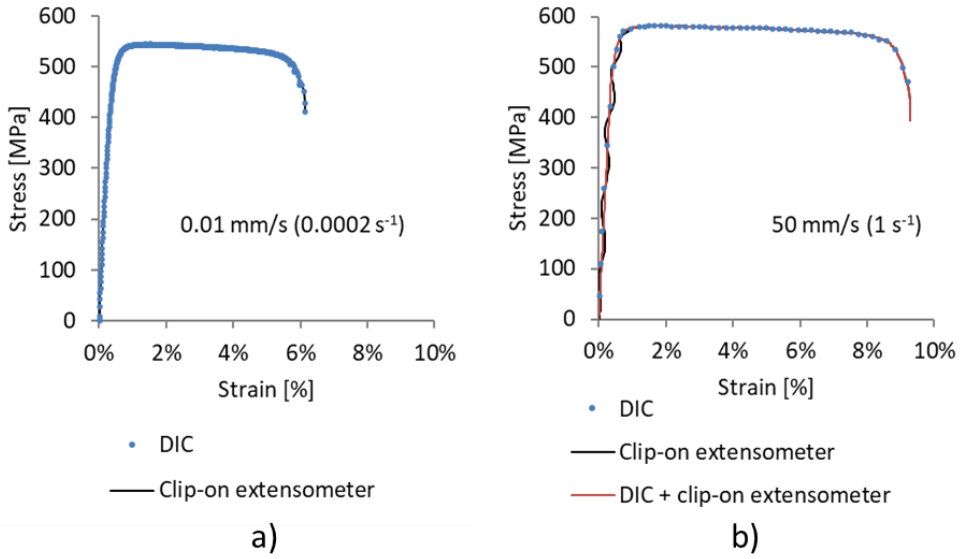

Figure 21. Comparison of engineering stress-strain curves for selected specimen with orientation 0°, wherein strain is measured with the extensometer and DIC method at strain rate of: a) 0.0002 s^{-1} (0.01 mm/s) and b) 1 s^{-1} (50 mm/s)

4.1.1. Stress-Strain curves

Based on the experimental data, engineering stress-strain curves for selected specimens with different alignment to the rolling direction at different strain rates were recorded and are presented in Figure 22. It can be observed that considered material demonstrates pronounced anisotropy in stress-strain curve. Furthermore, strain rate significantly influences material response. For each considered strain rate, strength and elongation have the greatest values for orientation 0°, while the lowest values are obtained for orientation 45°. With the increase of strain rate, strength and elongation are increased for all considered orientations.

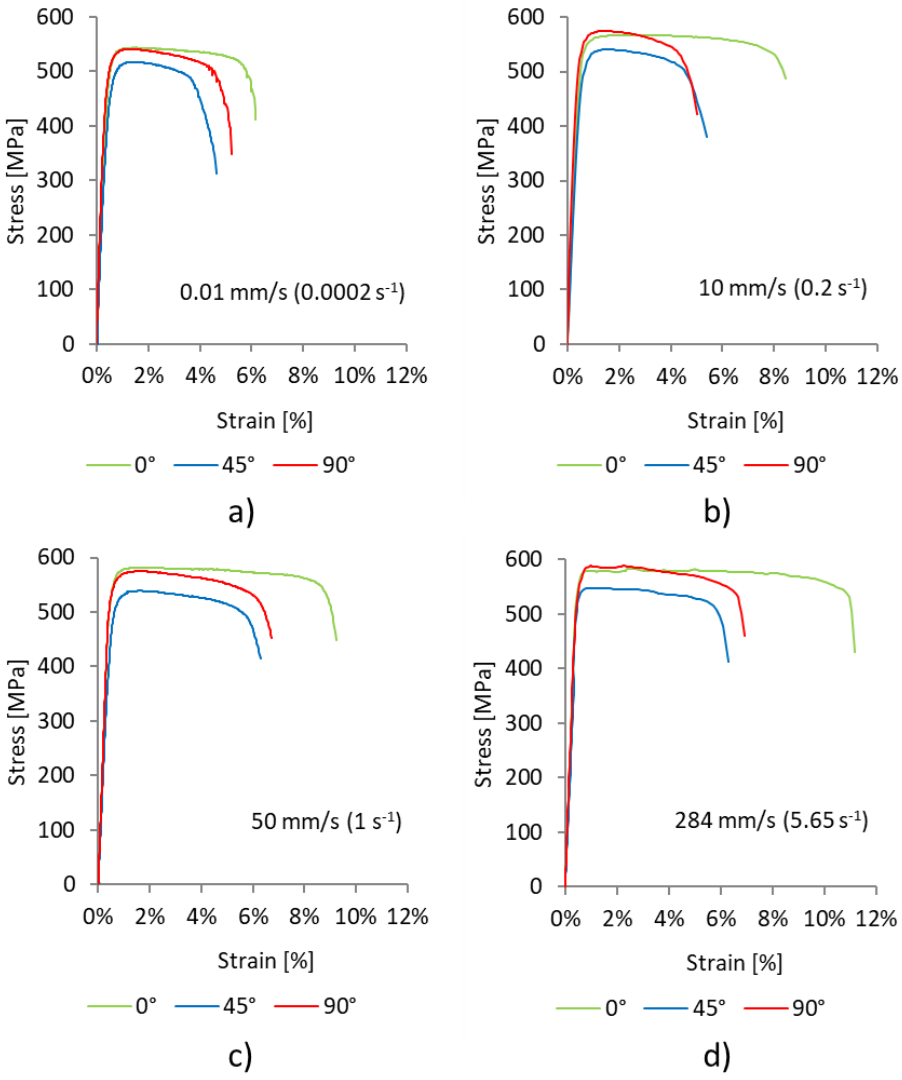

Figure 22. Comparison of engineering stress-strain curves calculated using DIC data for selected specimens with orientations 0°, 45° and 90° at strain rates: a) 0.0002 s^{-1}, b) 0.2 s^{-1}, c) 1 s^{-1} and d) 5.65 s^{-1}

The experimental results shown in Figure 23 present the impact of strain rate on the mechanical properties for specimens oriented at 0°, 45°, and 90° with respect to the rolling direction. Presented results are averaged data obtained from three samples for each considered orientation

while depicted vertical bars denote the lowest and the highest measured values. Considered mechanical properties are elastic modulus, tensile strength and elongation. It can be noticed that the elastic modulus is not influenced by the strain rate but is highly dependent on the specimen orientation angle. When considering reference specimen aligned with the rolling direction (0° orientation), it is evident that the one with orientation 90° exhibits a slightly higher elastic modulus, while the one with orientation 45° demonstrates a pronounced reduction of elastic modulus. In terms of tensile strength, a similar orientation dependence trend is observed. Here, specimen with orientation 90° has the highest tensile strength value, while specimen with orientation 45° has the lowest. For all orientations, tensile strength is increasing with the strain rate increase. This indicates that the material resistance to deformation improves under rapid loading conditions. The initial elongation trends diverge slightly from the patterns seen for elastic modulus and tensile strength. The reference specimen (0° orientation) possesses the greatest elongation, while the specimen with orientation 90° the lowest. However, as the strain rate intensifies, there is an increase in elongation for specimens with orientation 0° and 90°, while distribution for specimen with orientation 45° demonstrates one extreme for the considered strain rate range. This suggests that material ductility is increased at higher strain rates, which could have implications in forming processes where material ductility is a critical factor. The increase in elongation is the most pronounced for orientation 0°.

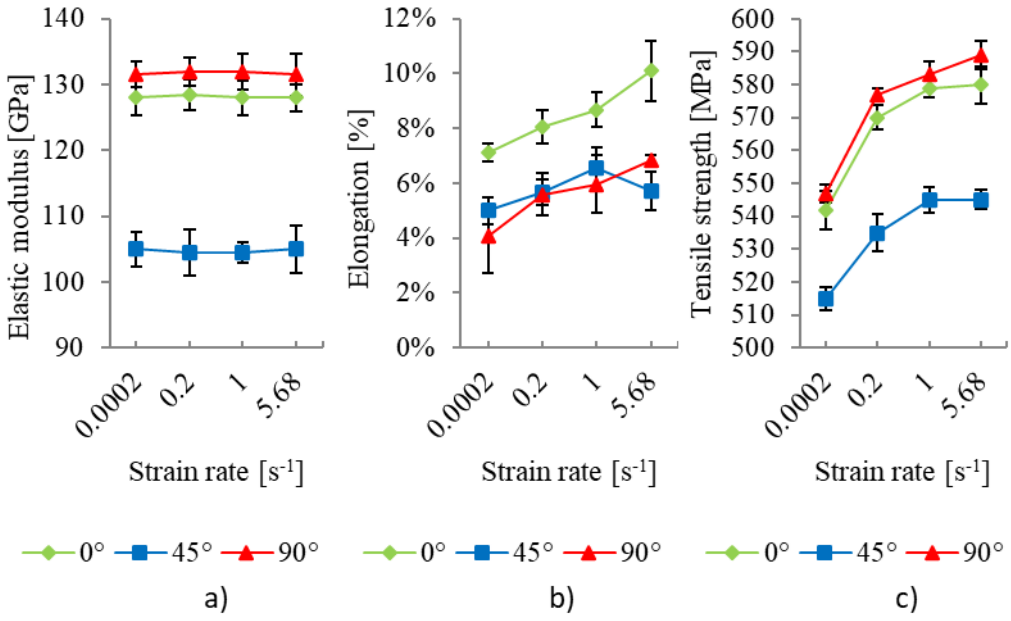

Figure 23. Comparison of a) elastic modulus, b) elongation and c) tensile strength calculated using DIC data for specimens with orientations 0°, 45° and 90° at different strain rates

The observed elongation rise for strain rate increase contrasts with reported results of similar studies found in literature. Elongation drop with strain rate increase is usually reported for metals, for instance, in studies incorporating aluminium alloy metal sheets AA6019-T4, AA6061-T4, and AA2139-T351 [126,127]. However, a study of influence of strain rate on uniaxial tensile properties for nano and ultrafine-grained (UFG) copper showed that for 200 nm UFG copper elongation increases with strain rate increase while for 110 nm UFG copper strain rate doesn't influence elongation [128]. Furthermore, same study reports that for the nano-grained copper with a grain size of 59 nm elongation decreases with strain rate increase. These observations indicate the influence of grain size on macroscopic material behaviour under different loading conditions. Furthermore, elongation increase with strain rate increase is reported for AA6016 alloy sheet in different tempers [129].

4.1.2. Utilization of infrared thermography

The experimental results show the effectiveness of Digital Image Correlation (DIC) in capturing deformation across specimen surfaces. While mechanical extensometer and DIC had the highest number of readings for quasi-static test of 0.01 mm/s velocity, IR camera wasn't able to capture temperature changes. IR method is not suitable for low-rate loading velocities due to the high thermal conductivity of copper alloy sheet and heat convection causing dissipation of thermal effect. Samples subjected to higher strain rates have been successfully acquired with both methods, IR and DIC, so results can be compared. Figure 8 presents the Von Mises equivalent strain distribution and thermal distribution for specimens oriented at 0° at loading velocities of 10 mm/s, 50 mm/s, and 284 mm/s. Each set of three images (DIC and IR) represents different stages of deformation: initial, mid-stage and near fracture. Provided Figures corresponding to different deformation stages enable analysis of the strain and thermal evolution during the tensile test. From these Figures, it can be seen that as the tensile specimen is being loaded, temperature and strain are increasing along the whole surface. When comparing IR thermography and DIC method one can observe an increase in temperature and strain occurring at the same location on the specimen. This correlation provides evidence that the generated heat is indeed a consequence of plastic deformation. Prior to a specimen failure, strain and temperature localize and form an angled slide line (in form "X") which can be seen in Figure 24.

With usage of DIC method it was feasible to determine local strains and measure elastic modulus more accurately. Although mechanical extensometer and DIC had the highest point

density at quasi-static test of 0.01 mm/s velocity, IR camera couldn’t capture temperature changes. IR method is not suitable for low loading velocities due to the high thermal conductivity of copper alloy and heat convection. Samples with higher strain rates have been successfully acquired with IR and DIC method, so results can be compared.

When comparing IR and DIC method, increase of temperature and strain can be noticed on the bottom of the specimen. As tensile specimen is stretched, temperature and strains are increased and “X” mark is formed on the specimen, until the rupture occurred. Fracture angle was close to 45°, which indicates that specimen is made of ductile material. DIC and IRT results can be seen in Figures 24.

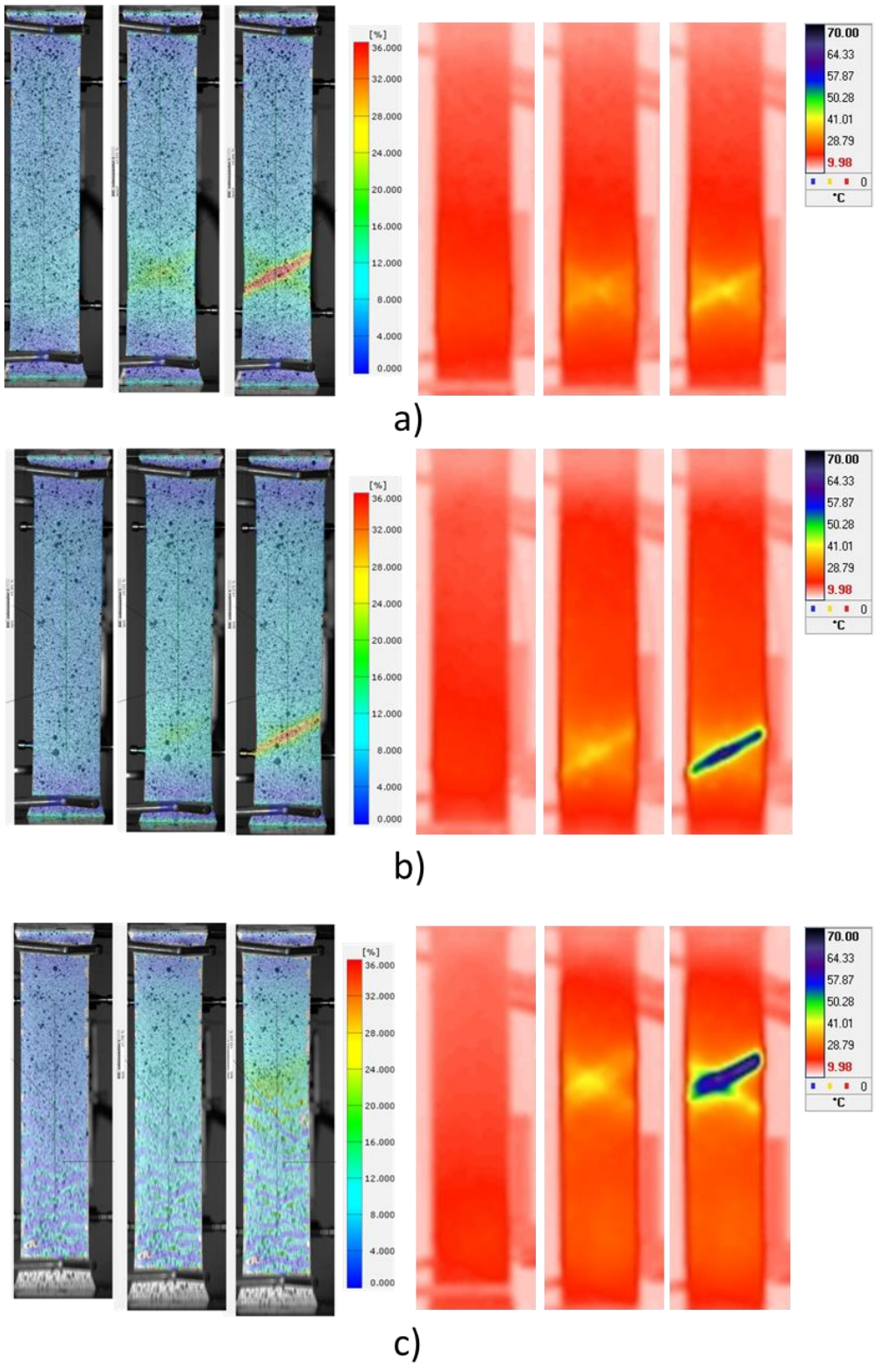

Figure 24. Von Mises equivalent strain distribution (2D DIC) and IR thermal distribution for specimen with orientation 0° during uniaxial tensile test conducted with velocity of a) 10 mm/s, b) 50 mm/s and c) 284 mm/s

The experimental determination of the inelastic heat fraction β across tensile specimens with different alignments to the rolling direction in tests performed with different strain rates gave

insight into the material thermomechanical behaviour. As previously mentioned, results obtained for a strain rate of 0.0002 s^{-1} were not analysed due to heat dissipation at lower tensile velocities due to the pronounced effect of heat dissipation, which could affect the calculation of inelastic heat fraction. For selected specimen with orientation 0°, surface temperature rise distributions along 50 mm gauge length at different elongations are presented in Figure 25. The gauge length is aligned with the axis 1, representing the longitudinal direction of the specimen positioned in the same way as DIC extensometer shown in Figure 20.

Calculation of inelastic heat fraction was conducted on tensile specimens in different rolling direction at different strain rate. As previously mentioned, samples at a strain rate of 0.0002 s^{-1} were not analysed due to heat dissipation at lower tensile velocities. Based on the specimen surface temperature rise according to Figure 25, mean temperature values were calculated for each test sample. According to equation (3), the calculated β coefficient shows dependence on the specimen orientation and the strain rate. Lowest β coefficient of 0.51 has specimen in rolling direction at strain rate of 0.2s^{-1} and highest β coefficient of 0.88 has specimen at 45° to the rolling direction at strain rate of 5.65 s^{-1}. Calculated values of inelastic heat fraction are presented in table 2.

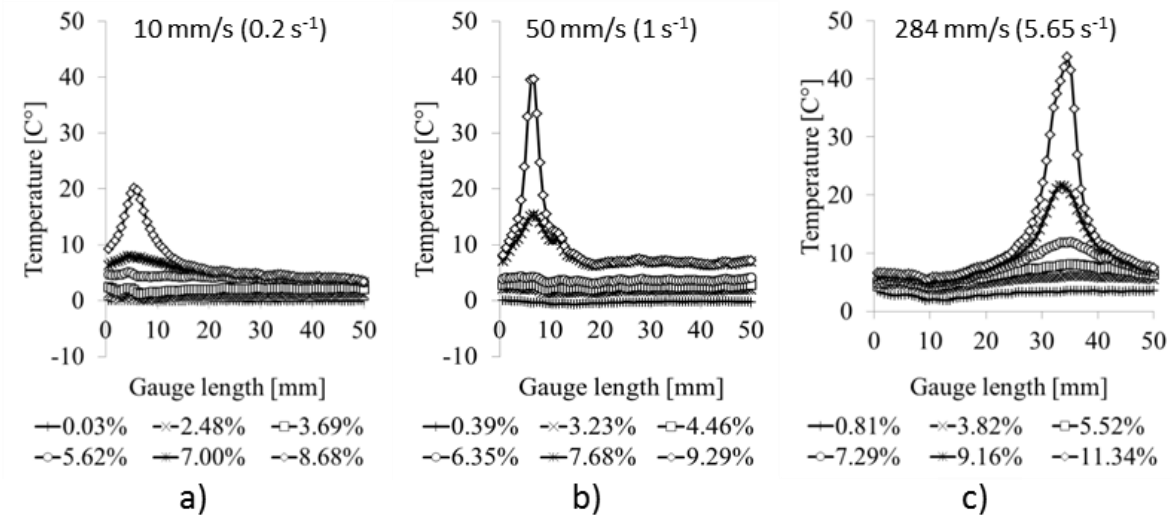

Figure 25. Temperature rise distribution of the specimen surface along longitudinal axis 1 for selected specimen with orientation 0° at loading velocity of: a) 10 mm/s, b) 50 mm/s and c) 284 mm/s

With the utilization of IR thermography, it is possible to distinguish between elastic and plastic deformation. For the uniaxial case, the first law of thermodynamics is given by relation (3).

Based on the specimen surface temperature rise according to Figures 24 and 25, mean temperature values were calculated for each tested sample. The results indicate that the β coefficient is not a constant value, as traditionally assumed and widely used in the literature [128]. This conclusion has also been addressed by other authors [97,130]. The nonlinear evolution of β, especially pronounced in specimens tested at higher strain rates, implies that the material's ability to convert plastic work into heat changes as deformation progresses. These experimental results demonstrate the importance of considering the strain rate and material anisotropy when evaluating the amount of work converted into heat. The observed dependency of β on these factors shows the need for more sophisticated models that can accurately predict energetic processes occurring during plastic deformation.

Table 4. Inelastic heat fraction at different strain rates for selected specimens with orientation 0°, 45° and 90° relative to the rolling direction

	β		
	0.2 s^{-1} (10 mm/s)	1 s^{-1} (50 mm/s)	5.65 s^{-1} (284 mm/s)
0°	0.51 ± 0.07	0.66 ± 0.05	0.72 ± 0.04
45°	0.61 ± 0.05	0.79 ± 0.05	0.88 ± 0.07
90°	0.70 ± 0.01	0.72 ± 0.01	0.81 ± 0.06

4.1.3. Breaking angle

The fracture characteristics of tensile specimens were assessed using an optical measurement technique. The primary focus of this analysis was the determination of the breaking angle Θ, a critical parameter for evaluating the fracture behaviour of the material. The objective was to capture the breaking angle of the tensile specimens differently aligned to the rolling direction across various strain rates. Values of the measured averaged breaking angles are presented in Table 5. It can be observed that the strain rate doesn't affect the breaking angle Θ. On the other hand, breaking angle is significantly influenced by specimen orientation. This difference arises as a result of the manufacturing rolling process, which leads to changes in the material microstructure. The dependency of the breaking angle on the specimen orientation highlights the importance of considering manufacturing induced anisotropy when predicting the fracture behaviour of materials in real-world applications.

Table 5. Average breaking angle at different strain rates for specimens with orientation 0°, 45° and 90° relative to the rolling direction

	Θ			
	0.0002 s^{-1} (0.1 mm/s)	0.2 s^{-1} (10 mm/s)	1 s^{-1} (50 mm/s)	5.65 s^{-1} (284 mm/s)
0°	62.4° ± 0.4°	64.6° ± 1.1°	63.7° ± 0.5°	62.2° ± 1.6°
45°	54.7° ± 1.2°	56.6° ± 0.6°	57.5° ± 3.3°	54.6° ± 0.9°
90°	57.5° ± 0.7°	58.2° ± 0.2°	59.1° ± 1.1°	58.1° ± 1.2°

In Figure 26 values of breaking angle corresponding to tensile elongation at break are presented for all tested samples and all considered strain rates. By considering results, unexpected trend can be noticed, with the increase in elongation, the breaking angle also increases.

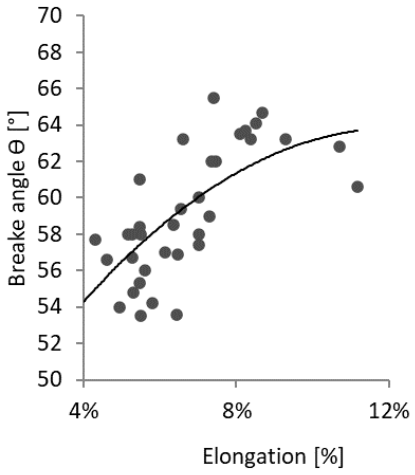

Figure 26. Specimen break angle in correlation with tensile elongation at break for all samples at all strain rates

Figure 27 presents influence of the tensile specimen orientation and strain rate on the breaking angle for the considered CuFe2P sheet material. The results are presented for all tested samples, i.e. three samples for each considered orientation and each strain rate. The breaking angle is a critical parameter in metal forming as it reflects the slope at which a metal begins to fracture or fails under stress. According to the results presented in Table 5, it can be observed that the rolling process affects the breaking angle due to the anisotropic properties introduced during the rolling process, while the strain rate appears to have a minimal impact. Specimens oriented along the rolling direction exhibit the highest Θ values, ranging between 60.6° and 65.5°. Specimens oriented at 45° to the rolling direction have the lowest Θ values, ranging between 53.5° and 59.4°, while specimens perpendicular to the rolling direction display Θ values ranging between 56.8° and 61°.

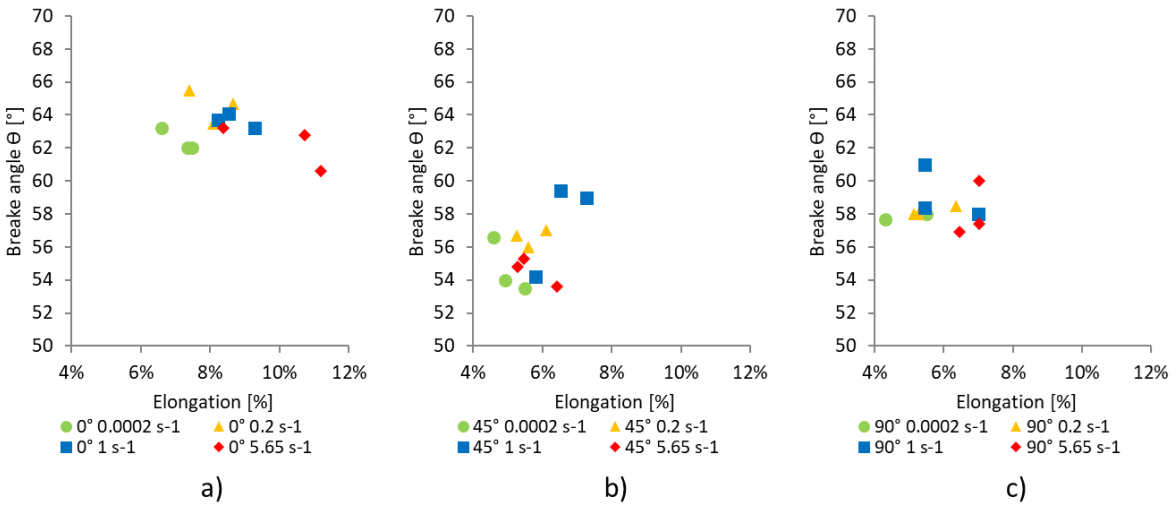

Figure 27. Strain rate influence on the breaking angle for specimens with alignment to the rolling direction: a) 0°, b) 45° and c) 90°

4.1.4. Lankford coefficient

Lankford coefficient, or *r*-value, is defined as the ratio of the true plastic strain in the width direction ϵ_{22}^{p} to the true plastic strain in the thickness direction ϵ_{33}^{p} during uniaxial tensile testing:

$$r_\theta = \frac{\epsilon_{22}^{p}}{\epsilon_{33}^{p}} = \frac{ln\left(\frac{w}{w_0}\right)}{ln\left(\frac{t}{t_0}\right)}. \quad (5)$$

Due to the assumption of the incompressibility hypothesis, the equation for thickness strain can be expressed as

$$\epsilon_{33}^{p} = -(\epsilon_{22}^{p} + \epsilon_{11}^{p}) \quad (6)$$

and Lankford coefficient can be calculated as

$$r_\theta = \frac{\epsilon_{22}^{p}}{-(\epsilon_{22}^{p} + \epsilon_{11}^{p})} = \frac{ln\left(\frac{w}{w_0}\right)}{-\left(ln\left(\frac{w}{w_0}\right)+ln\left(\frac{l}{l_0}\right)\right)}. \quad (7)$$

In above equations *w*, *t* and *l* are width, thickness and length, respectively in combination with subscript 0 representing their initial values. According to the standard [131], the Lankford coefficient can be determined in two ways:

- As a constant value, the *r*-value is calculated from the slope of the line drawn through the origin in a plot of true plastic strain in the width direction versus true plastic strain in the longitudinal direction over the entire deformation range.

- As an incremental value: the *r*-value is calculated incrementally as the slope of the line in the same diagram, but this time considering different segments of the deformation curve. This approach allows the *r*-value to be analysed as it changes with ongoing deformation.

In order to obtain Lankford coefficient for tested orientations Digital Image Correlation (DIC) method was utilized. Based on the measurements, total strains in specimen's width and longitudinal directions are obtained for the defined area of the specimen. Lankford coefficient is then calculated as the ratio of width and thickness plastic strain measures according to equation (7). For the specimens with orientation 0°, under different strain rate conditions, Lankford coefficient is calculated for different values of the longitudinal true plastic strain and results are presented in Figure 28. It can be observed that *r*-value changes with ongoing deformation process during tensile testing. This alternation is the most pronounced for the highest considered strain rate, where rapid reduction of *r*-value with longitudinal strain can be observed. For lower considered strain rates, alternation of *r*-value with on-going deformation is less pronounced. These results clearly indicate that strain rate has impact on *r*-values for the considered orientation.

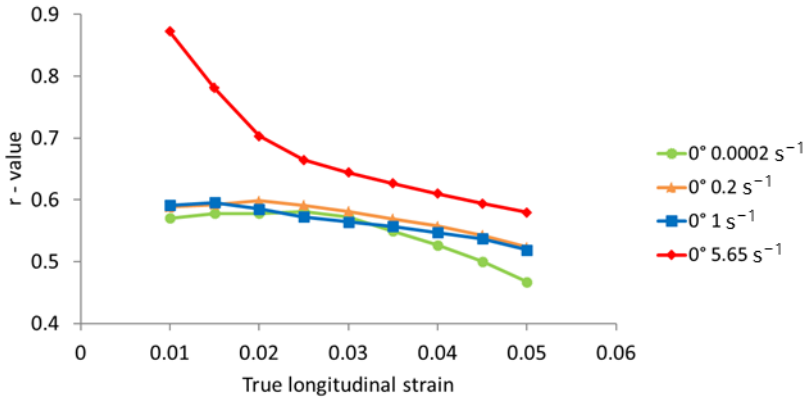

Figure 28. Lankford coefficient at different longitudinal true strains for specimens with orientation 0°

In Figure 29 influence of the strain rate on orientational dependence of Lankford coefficient, calculated at 2.5% of true longitudinal strain, is presented. Since for different orientations, *r*-values are significantly different it can be stated that material exhibits highly anisotropic

behaviour. Furthermore, strain rate has the smallest impact on *r*-values for orientation 0° and highest for orientation 90°. There is no clear indication that higher strain rates will result in greater *r*-values for all specimen orientations, but a trend of *r*-value increase between quasi-static test speed and higher strain rates can be seen. Traditionally, *r*-values are considered constant in anisotropic material models. However, presented experimental data revealed that *r*-values vary with ongoing deformation process and are affected by strain rate, challenging the assumption of constancy and emphasizing the importance of strain rate in assessing material anisotropy.

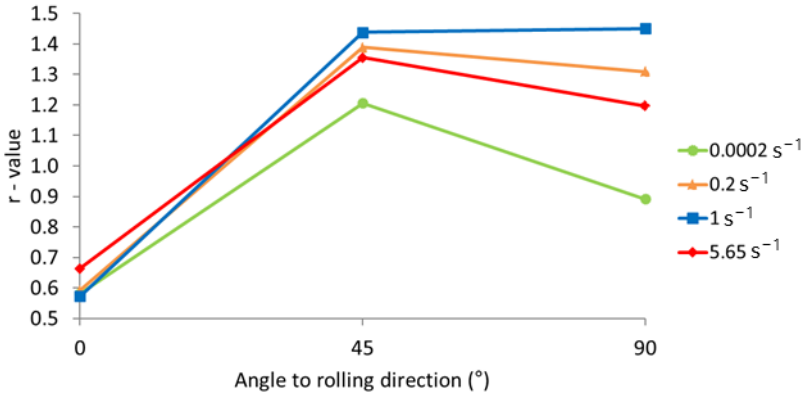

Figure 29. Influence of the strain rate on orientational dependence of Lankford coefficient calculated at true longitudinal strain corresponding to 0.025

4.2. Compression tests at different velocities

In the wire crimping process, the terminal wing will bend towards the wire strands and then compress together to the final plastically deformed shape. During the bending process of a wings, stress arises due to the movement of the crimping tools. The stress distribution is not uniform; it varies across the thickness of the material. The outer surface of the plate, convex side, experience the tensile while the inner shape of the plate, concave side, experience the compressive stress. At the neutral axis, which is an imaginary line within the material where the stress is zero, the material does not experience elongation or compression. As bending progresses, the material may yield if the stress exceeds the material's yield strength, leading to permanent deformation. Soon after the terminal wings touch the wire strands and penetrate deeper into them, compressive stress will become dominant.

The compression test performed in this study was not a standard one, as the scope of the investigation was to have a more realistic approach. In the test, 7 plates with dimensions 17.5

x 7.5 mm, were positioned on top of each other and compressed with a 7 mm thick tool. During the initial trial test, it was noted that tools had a tendency to move aside. To prevent that movement, a guiding tool was designed to have precise control and repetency of the test. Tool slippage in test trial and fixation tools design are presented in Figure 30.

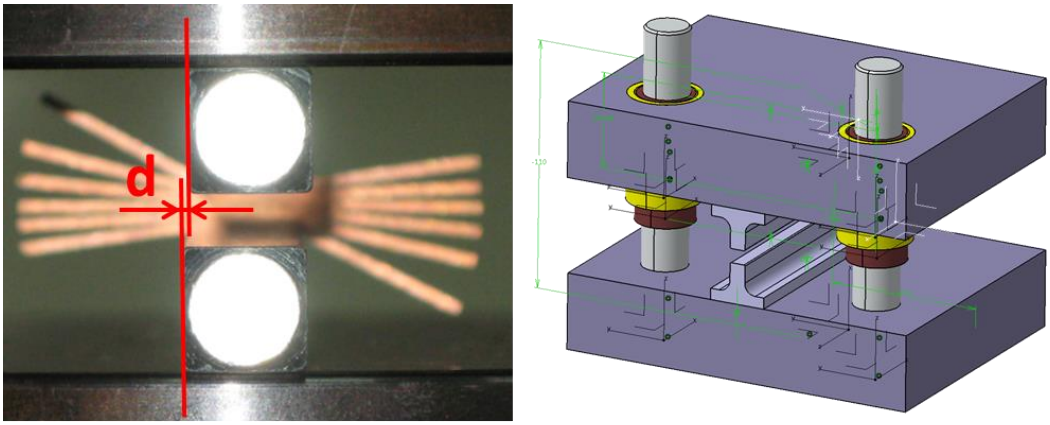

Figure 30. a) Compression tools slipping a side b) design of a guiding tool to prevent slipping movement

For the purpose of DIC measurement, on the side surface of the plates, the stochastic pattern of paint was applied. The pattern was applied the same way for tensile test specimens: first white colour, then black, with stochastic dots on top of it. In the case of these compression plates, the additional tool was made to allow better distribution of paint only in the area where it is needed. As seen in Figure 31, compression plates were put on each other in the array, while each array was separated with a spacer so paint wouldn't go on surfaces other than needed one.

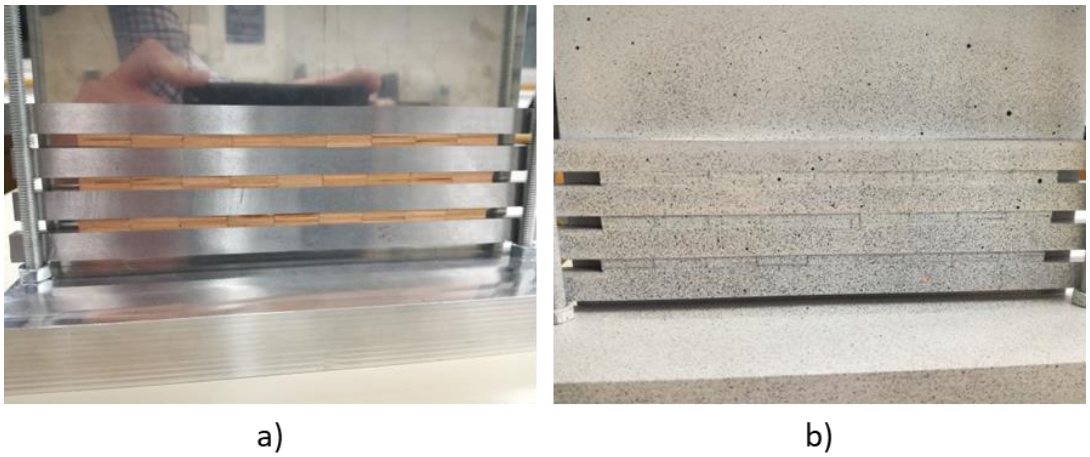

Figure 31. Compression plates a) without paint and b) with paint

Due to the small specimen size and small recording surface, the optical camera was moved more forward towards the specimens, giving no space for the IR thermal camera to measure temperature rise during the same test. Therefore, the same test setup was evaluated separately with DIC and IR methods. To have a consistent result, especially due to the small specimen size, a positioning tool was made into which 7 plates were loaded and centred to the guiding tool as presented in Figure 32.

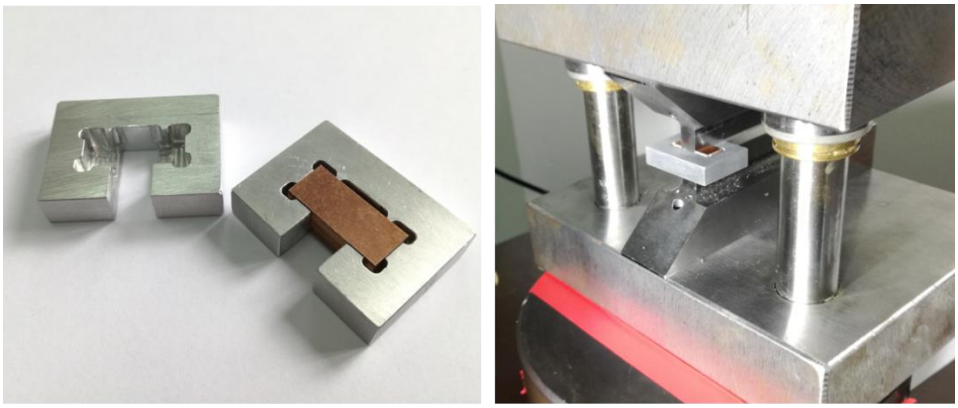

Figure 32. a) Positioning tool and b) positioning tool mounted on guided tool

Compression test was conducted with four different speeds: 0.01, 0.1, 10 and 50 mm/s. For a speed of 0.01 mm/s, an IR camera was not used, as heat would spread over plates and finally exchange with the ambient environment. During the compression test, when material locally passes the yield point and starts to deform plastically, the temperature will start to increase. In a controlled experimental setup, copper plates were subjected to uniaxial compression to investigate the thermomechanical response of the material. Each sample set was compressed with a displacement of 2 mm. The deformation of the plates was recorded, revealing a correlation between the degree of deformation and the generated heat. As the compression forces intensified, the plates underwent substantial plastic deformation, which, in turn, led to a rise in temperature. This thermal effect was attributed to the conversion of mechanical work into thermal energy, a phenomenon consistent with the principles of plasticity and heat transfer in metals. Correlation can be seen in Figure 33, where in the first step, there is a noticeable formation of “X” for both IR and DIC images. In further compression steps, X formation is constantly visible on DIC images, but on IR, it starts to blur due to the high heat conductivity of considered copper and copper alloy (CuFe2P).

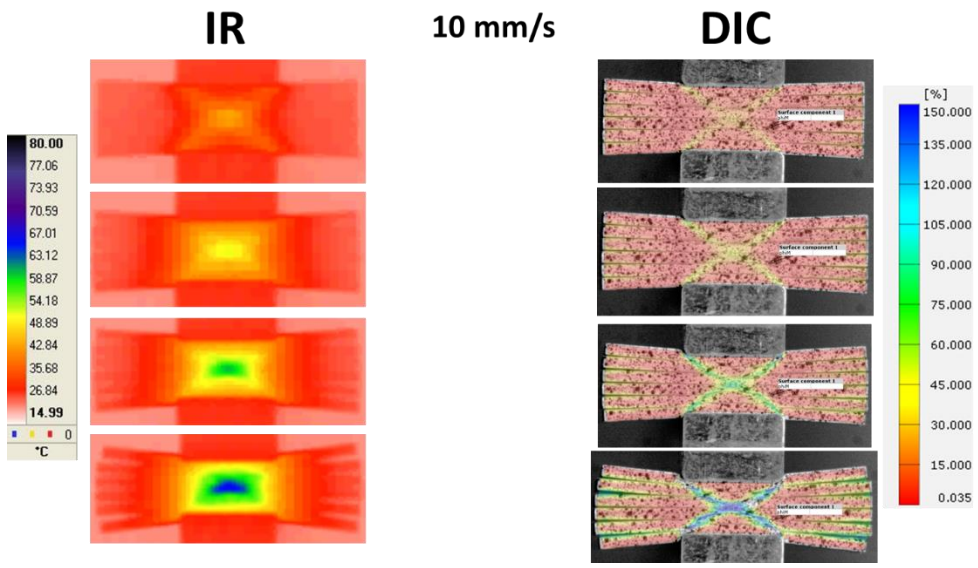

Figure 33. Thermography and DIC images during compression test of CuFe2P

The force-displacement curves generated from these experiments serve as a critical tool for understanding the material's response to varying strain rates. As the deformation speed was incrementally increased, a corresponding increase in the force required to achieve a given displacement can be seen. This phenomenon is indicative of the strain rate sensitivity of copper and its alloys, a characteristic that is commonly associated with the rate-dependent nature of the material's flow stress. These compression test results correspond to the previous results of the tensile tests at the different strain rates. These trends can be seen in Figure 34, for Cu-ETP and Figure 35, for CuFe2P.

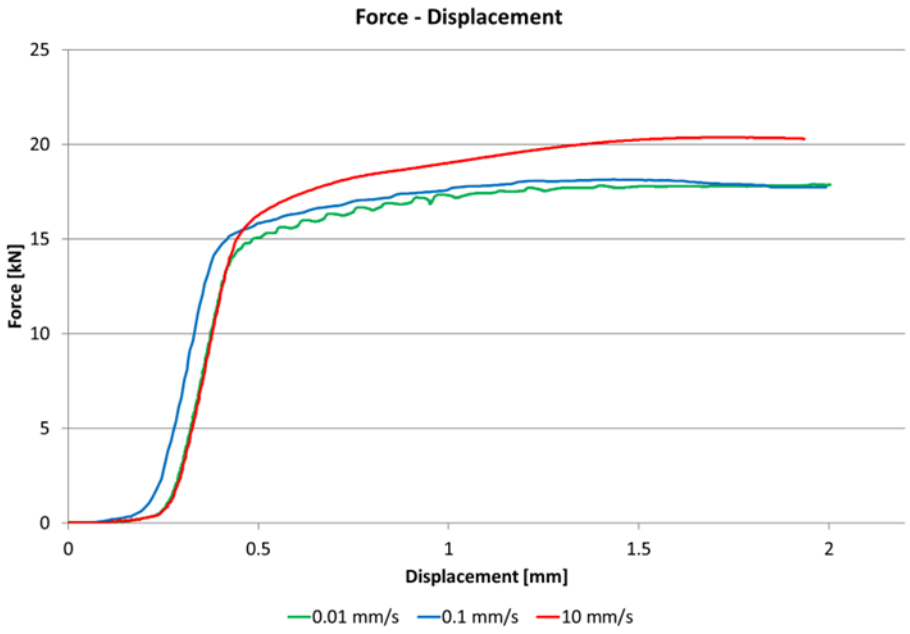

Figure 34. Compression tests for pure copper Cu-ETP at different velocities

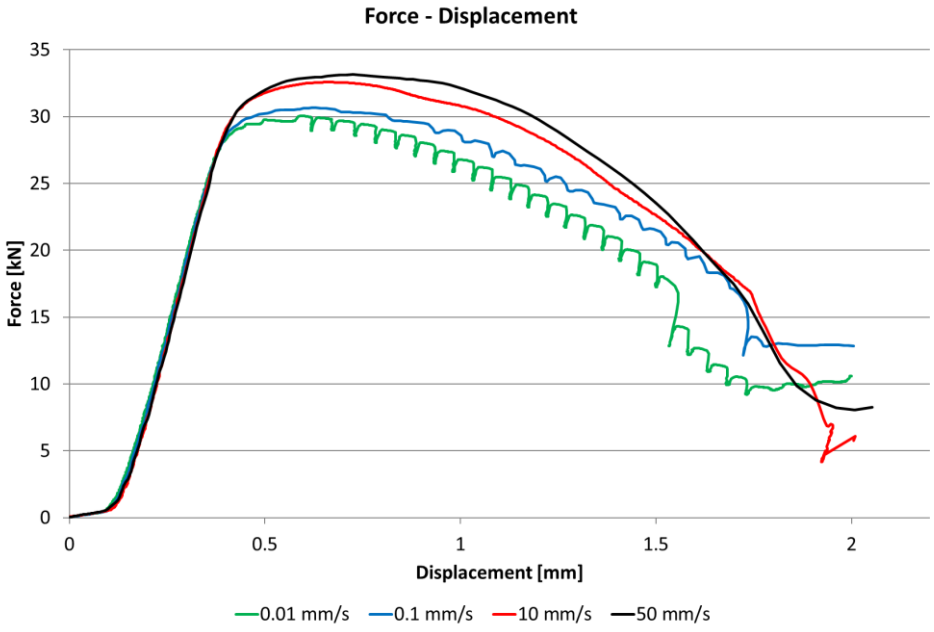

Figure 35. Compression tests for copper alloy CuFe2P at different velocities

4.3. Crimping tests at different strain rates

The mechanical characterization of crimping processes under varying strain rates is essential for understanding the deformation behaviour of terminal wings during crimping operations. This study presents a comprehensive approach to crimping tests, where a crimping tool applicator is integrated into a tensile testing machine Instron 8801. The objective is to simulate the crimping process under controlled conditions, with precise manipulation of different velocities, starting from quasi-static to dynamic conditions.

The experimental setup is designed to ensure repeatability and accuracy, as can be seen in Figure 36. The tensile testing machine is equipped with a high-capacity load cell to measure the forces involved in the crimping process, while the DIC system and IR camera are synchronized to capture the deformation and thermal fields simultaneously. This synchronized data acquisition is vital for correlating mechanical and thermal responses with the applied strain rates.

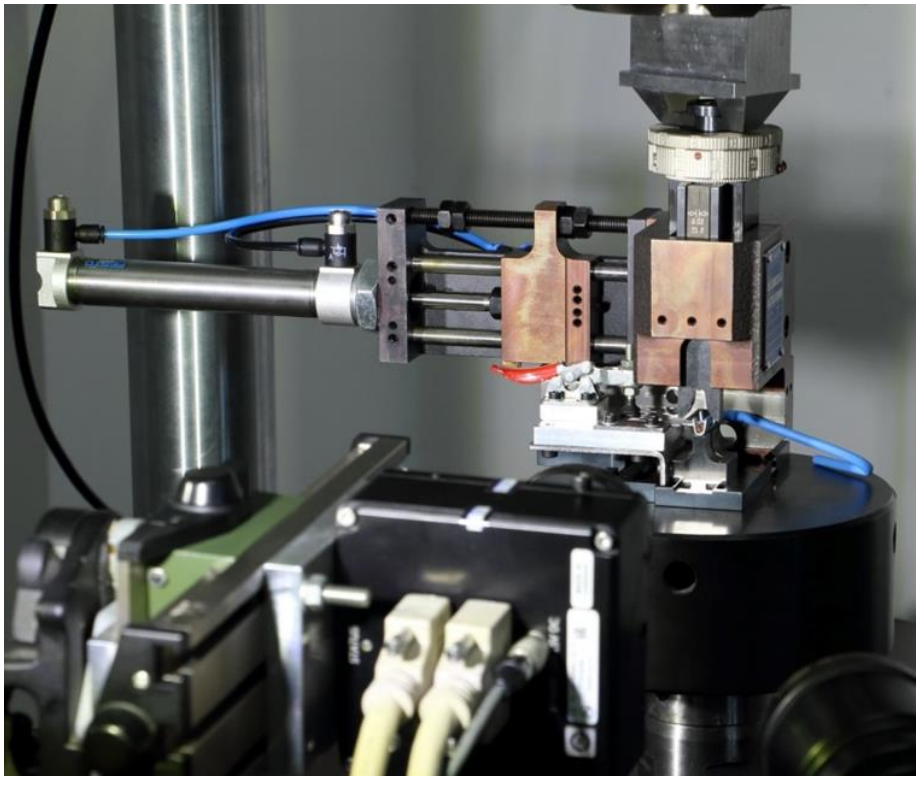

Figure 36. Experimental setup for crimping test

To capture the details of the deformation process, DIC and IRT methods were employed. DIC is a non-contact, full-field optical technique that provides a detailed understanding of the strain

distribution across the surface of the terminal wings. By applying a stochastic speckle pattern on the surface of the material and utilizing advanced image correlation algorithms, DIC enables the measurement of displacement fields and the calculation of corresponding strains with high accuracy. Results of DIC strain measurement during crimping at speed of 10 mm/s, can be seen in Figure 37.

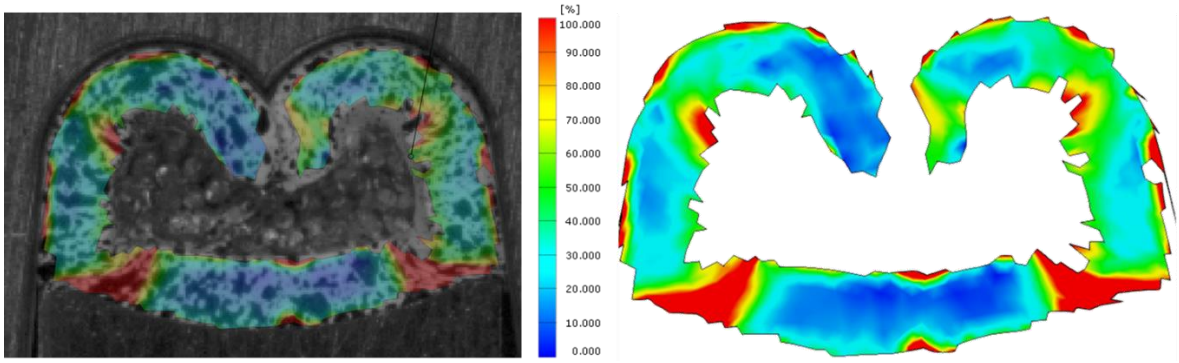

Figure 37. DIC strain measurement during crimping at 10 mm/s

Digital Image Correlation is a powerful tool for capturing full-field strain data, but it has limitations in high-speed applications like crimping. The failure to capture the terminal wings during crimping speeds above 50 mm/s can be due to several factors. The movement of the bottom jaws in the tensile test machine at increased speed is giving terminal high acceleration, which is already pushing camera to the limits. When terminal and applicator movement being combined with the wings bending process when rolled by crimping tool, it exceeds the camera's capabilities to keep exposition time low and images clear. If the top jaw had been moving instead, it might have offered a more stable platform for DIC, potentially reducing motion blur and allowing clearer image capture, thus improving the results. Additional factor may be the thickness of the material, which is just 0.8 mm. Blurred image at velocity of 50 mm/s can be seen in Figure 38.

Figure 38. Blurred image captured by camera at crimping speed of 50 mm/s

The goal of thermography was to measure temperature rise, i.e. thermal effects, due to plastic deformation and contact friction. At the slowest speed of 0.1 mm/s, the thermographic data indicated minimal heat generation, indicating that the rate of work done on the material was over a long period of time so significant temperature rise was avoided. As the crimping speed increased to 10 mm/s and 50 mm/s, an increase in temperature was captured, which is due to the higher strain rates. At the highest speed of 284 mm/s, the thermography results showed the highest increase in temperature, which confirms the influence of strain rate on thermal energy conversion. The rapid deformation at this crimping speed resulted in quasi-adiabatic heating, where the heat generated could not spread quickly through material or exchange with ambient environment, leading to localized temperature spikes. These thermographic findings are useful for understanding the thermal dynamics of the crimping process. Images captured during crimping process at velocity of 284 mm/s are shown in the Figure 39. Initial temperature rise measured at the terminal surface is during wings bending, when material is being deformed plastically, as can be seen on image a). With further crimping tools stroke, plastification of the top wings will increase, but also bottom of the barrel will start to deform above yield point and generate heat. At the end of a crimping step, temperature on complete surface will converge to uniform values as complete terminal will plastically deform due to compression. Additionally, the high thermal conductivity of CuFe2P ensures that heat disperse evenly across the terminal surface.

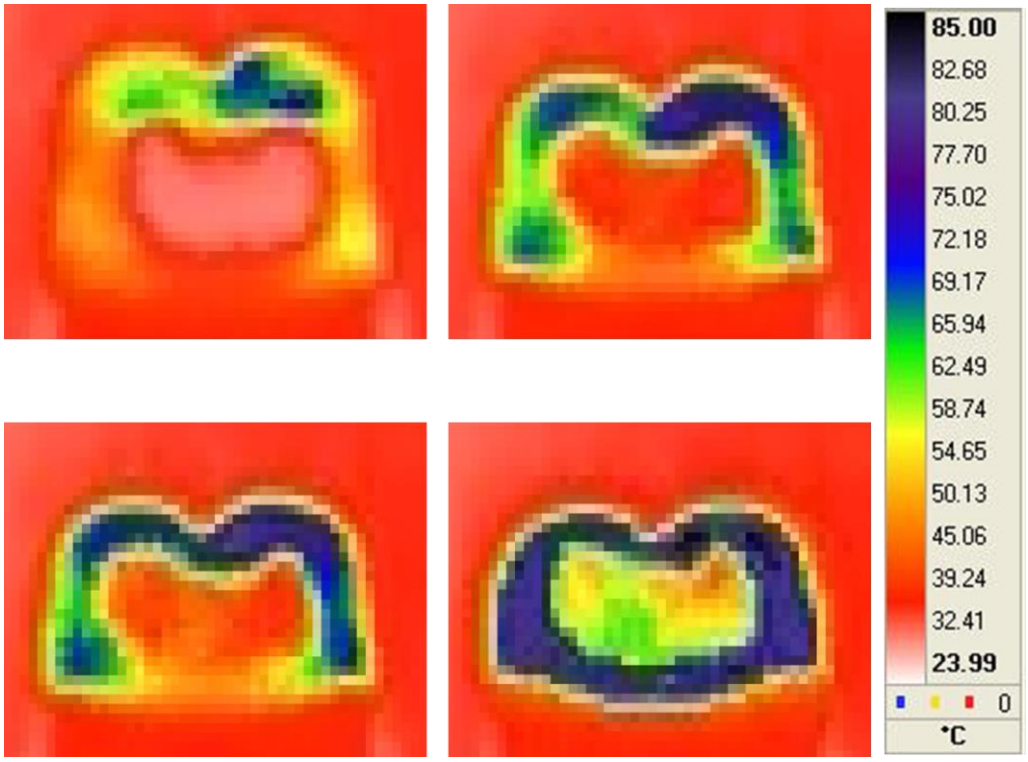

Figure 39. Temperature rise captured by IRT camera during crimping process at 284 mm/s

4.3.1. Crimping speed measurement

To accurately measure the speed of an eccentric press during the crimping process, a high-speed slow-motion camera was used. Camera is set up to capture the rapid movements of the press, which is not achievable with regular 60 FPS camera. Tests were done on a manual crimping machine with the usage of an Olympus i-SPEED 3 camera with an acquisition rate of 7500 FPS. The time needed for the eccentric press to go from the top dead centre (TDC) to the bottom dead centre (BDC), which is half of the cycle, is 0.28 s and an additional 0.26 s to return to the top dead centre. Images captured by high-speed camera at different points are shown in Figure 40. Standard crimp stroke for crimping machines is 135.78 mm, based on that average crimping speed is 483 mm/s is calculated.

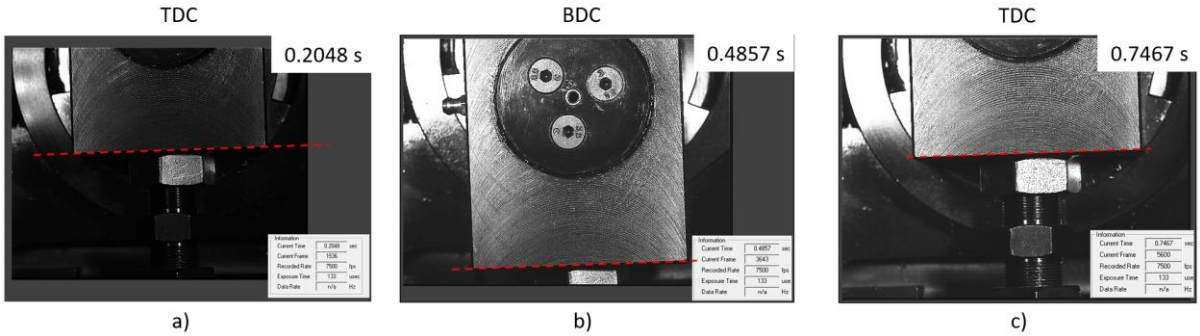

Figure 40. Position of eccentric crimp press at a) TDC, b) BDC and c) end of a cycle -TDC

4.3.2. CT scan of a crimped terminals

After the terminal is crimped, the standard procedure for evaluation of crimp quality is performing micro-cuts to ensure that the shape of the crimp is according to the specifications. Unfortunately, that would result in the destruction of the tested sample. With the implementation of the non-destructive method, computed tomography (CT), one terminal sample can be crimped, scanned, and mechanically tested at the tensile test machine. The standard output of CT scan measurement is the outer surface of the scanned product. Positioning of the terminal into fixture and visualization of the terminal can be seen in Figure 41.

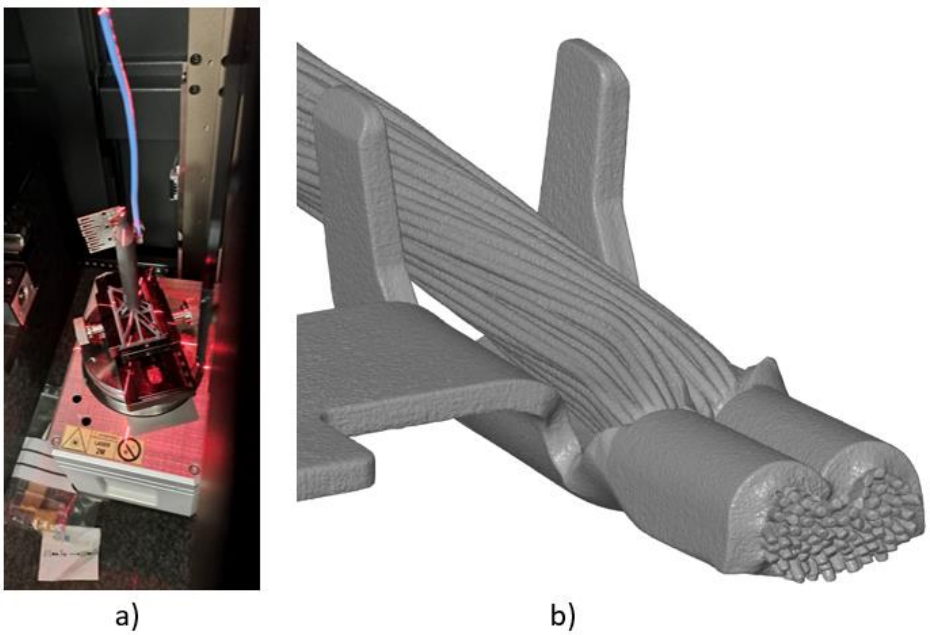

Figure 41. a) Sample positioned on CT scan machine b) 3D visualization of scanned part

Getting the 3D shape of crimped terminal or some other product, is straightforward. By choosing an adequate filter and setting X-ray tube parameters in terms of voltage, current and exposition time, CT scan can be made. For evaluation of the cross-section shape, the highest resolution to capture interesting details in the crimp should be used. With a magnification of 7XL, the voxel size would be 3 µm; this is the highest magnification achievable with the possibility to fit the crimped terminal inside the measuring area. Voxel as 3D cubic shape (3x3x3 µm) would be presented as a pixel in 2D space (3x3 µm). As the thickness of the tin plating on the terminal is small, up to three sizes of the voxel, it is challenging to extract the plating of a scanned sample. Improved method for obtaining better data from CT scan measurement was suggested and implemented [132]. With multispectral scan (MSP) at least two CT volumes are made with different x-ray parameters, and finally combined into one scan output. MSP scan parameters can be seen in Table 6.

Table 6. CT scan parameters for MSP

	Filter	Voltage [kV]	Current [µm]	Exposition [ms]	Images
1st scan	Cu - 1 mm	225	70	2500	6400
2nd scan	Sn - 2 mm	225	90	4000	6400

These parameters showed adequate contrast between different materials within the copper and thin tin plating. Adjusting the X-ray energy levels can help optimize the contract and reduce noise. Result of cross section made on CT scan sample can be seen on Figure 42. Based on equation (4) wire strand compression can be calculated from representative cross section area. Raw data format (.rek) was evaluated with Fiji software. The result is a yellow highlighted boundary between wire strands and the terminal.

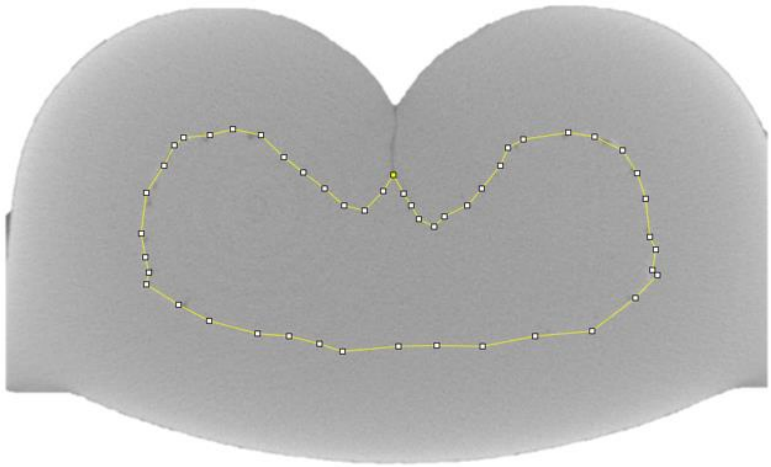

Figure 42. Cross section based on MSP CT scan with a yellow line representing boundary between terminal and wire strands

4.3.3. Wire pull-out force

To find the relationship between the wire compression and the wire pull-out force from the crimped terminal, it is necessary to perform tests on the tensile test machine. The experiment involves crimping a series of terminals onto wires with varying degrees of compression, achieved by adjusting the crimping tool's settings to different indentation depths. Each crimped assembly was then subjected to a pull-out force test using a tensile test, which measured the force at a defined path with the goal of finding the maximum force the crimped terminal can withstand. The wire was attached to upper, movable clamps, while the terminal was fixed to the bottom clamp, as can be seen in Figure 43. Wire length between crimp and upper clamp was set to 50 mm.

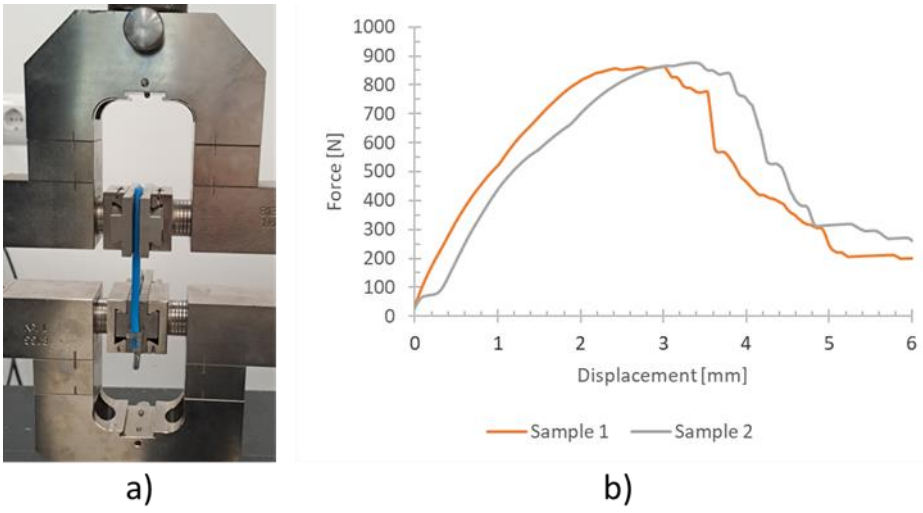

Figure 43. Wire pull-out a) experimental setup and b) force displacement graph of wire pull-out

The tensile test of wire pull-out was performed at the speed of 25 mm/min, until the wire was pulled from the crimped terminal or failure occurred. The failure type (e.g., wire breakage, terminal deformation, or slippage) and the corresponding maximum tension value were recorded for each sample. The collected data were then analysed to establish a correlation between the compression value, calculated from CT scan, and the pull-out force. This correlation provided insights into the optimal compression level for ensuring a secure and reliable crimp connection, which is critical for maintaining the integrity of electrical connections in wiring harnesses.

4.4. Deep drawing test

Deep drawing is one of the most popular numerical validation methods for anisotropy, and due to that, this test was also conducted. In the experimental investigation of the deep drawing process, a CuFe2P copper alloy was used to form cups from an initial circular plate with a diameter of 65 mm and a thickness of 0.8 mm according to Figure 44. This high-strength copper alloy is often used as a base material for terminal design due to its good electrical conductivity and mechanical properties, although elongation is not so high. The deep drawing test was conducted under controlled conditions, during which force was monitored, to ensure the material's behaviour could be accurately captured and used to validate an anisotropy model within numerical simulations. The forming process involved positioning the circular blank between a die and a blank holder, and subsequently drawing it into a cup shape using a punch as can be seen on Figure 44.

Figure 44. a) Deep drawing setup with b) positioned ⌀65 mm circular plate

Key process parameters, such as punch speed, binder force, and lubrication were varied until the desired cup shape was achieved. The produced cups were then evaluated for damage or some artefacts due to material bulking. These empirical observations were essential for validating the numerical model with deep drawn cup geometry. Figure 45 represent tolls dimensions used for deep drawing of a cup.

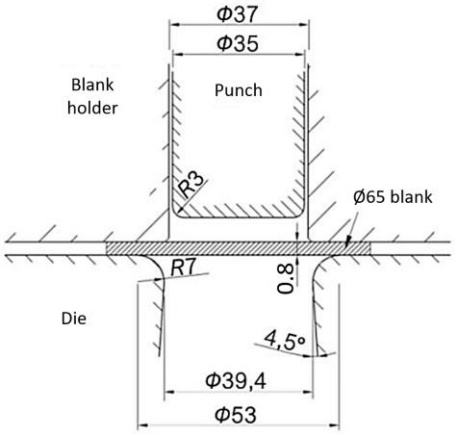

Figure 45. Geometry shape used for deep drawing

In the experimental investigation of material anisotropy through the deep drawing of circular plates, the formation of ears on the drawn cups was observed. This earring effect is a direct manifestation of the material's anisotropic behaviour in plastic flow. In the case of anisotropic flow, the material's behaviour during the forming process is strongly influenced by the directional properties of the sheet metal. The presence of ears indicates that the material

exhibits different flow resistances in various orientations relative to the rolling direction (RD). For evaluation of earing height difference, CT scan of sample was made. Results of CT scan and difference in cup height can be seen in Figure 46. The presented results are based on one cup sample, and the measured height represents one-quarter of a cup.

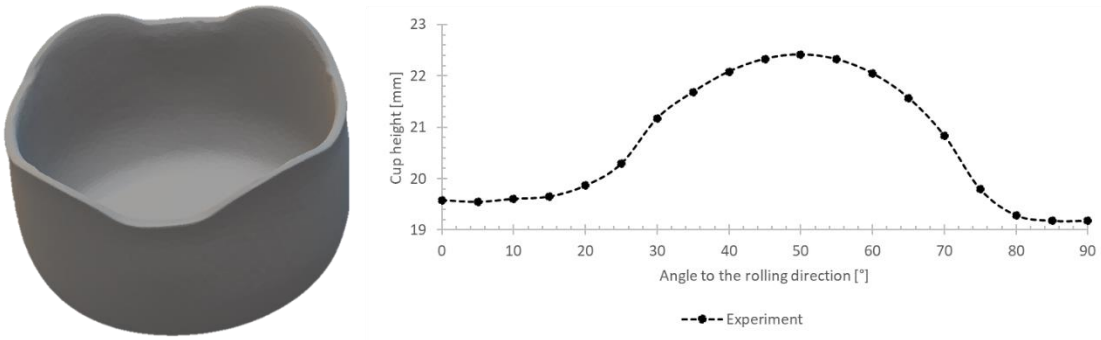

Figure 46. CT scan of deep drawing sample and cup height measurement

Cup earrings result from severe CuFe2P anisotropy and variations in Lankford coefficients (*r*-value) with uniaxial tensile specimen orientation to the rolling direction. The highest cup height is measured at 50° orientation to the rolling direction, with a value of 22.4 mm, while the lowest is at 90°, with a value of 19.2 mm. For the considered quarter, the maximum amplitude of the heights amounts 3.2 mm.

4.5. Tensile tests for specimens with seven orientations relative to the rolling direction

An uniaxial tensile test performed in three rolling directions (0°, 45° and 90°) showed that the CuFe2P sheet is highly anisotropic, which was additionally confirmed with cup earrings after a deep drawing process. In order to describe anisotropic behaviour with more advanced constitutive models, there is a need for additional tests. For example, anisotropic yield criterion Yld2004-18 has 18 parameters by which material anisotropy is described. Calculation of these parameters requires uniaxial tensile data for seven specimen orientations (every 15°, from 0° to 90°). Tensile tests with strain rates of 0.0002 s^{-1} were conducted on sheet specimens with orientations of 0º, 15°, 30°, 45º, 60°, 75° and 90º to the rolling direction. For this purpose, CuFe2P sheet specimens were tested according to the DIN 50125 specifications with the geometry shown in Figure 47.

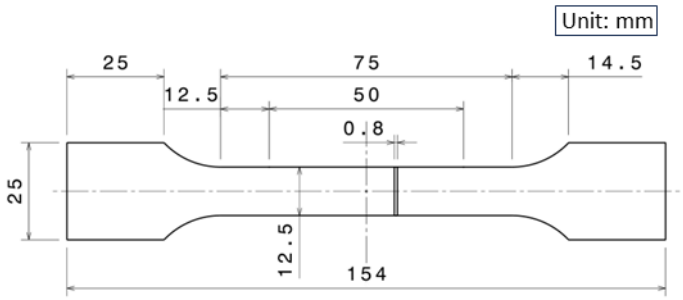

Figure 47. The geometry of CuFe2P tensile specimens for uniaxial tests performed on seven orientations relative to the rolling direction (every 15°, from 0° to 90°)

Tensile tests were performed on the tensile testing machine Instron 8801 at a constant velocity of 0.02 mm/s, using longitudinal and lateral clip-on extensometers. Four samples, 28 in total, were used for each orientation, according to Figure 49. One sample with the highest discrepancy in stress-strain results was discarded from the four initial samples for each orientation.

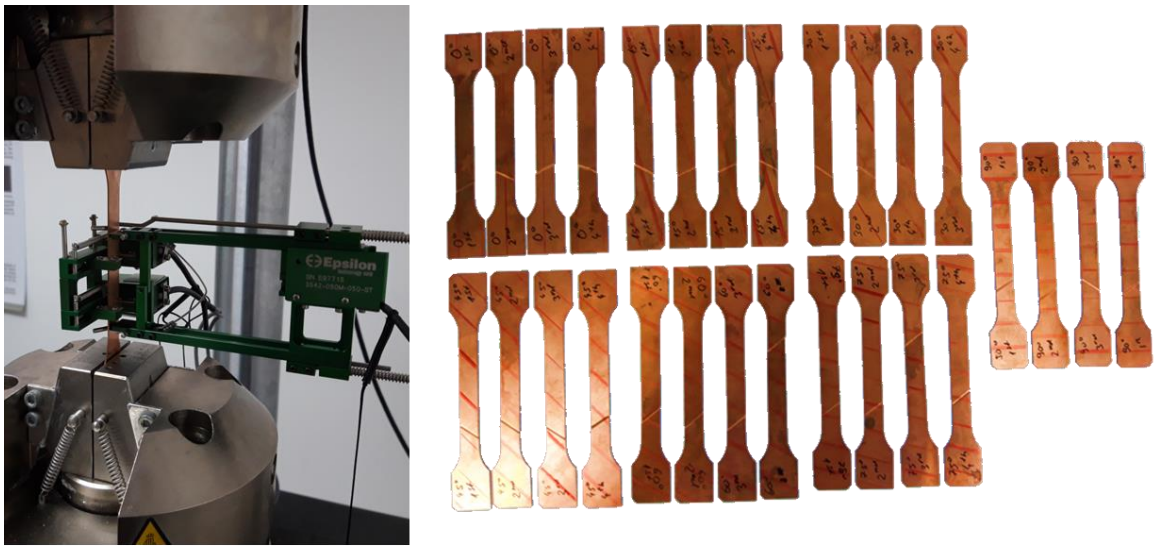

Figure 48. Uniaxial tensile a) experimental setup and b) tested specimens

From tensile test machine force measurement and longitudinal extensometer data, true stress-strain diagrams are generated as shown in Figure 49. The results are presented for three samples for each orientation. Based on this data, material characteristics like Young's modulus, Poisson's ratio, yield stress, tensile strength and elongation were obtained. Obtained results clearly show differences between these material characteristics with variations of the specimen orientation to the rolling direction, which confirms prior investigations about the CuFe2P

sheet's severe anisotropy. For instance, specimens oriented at 90° to the rolling direction have the highest values of elastic modulus, up to 143.3 GPa, while specimens oriented at 30° to the rolling direction have the lowest value, down to 108.7 GPa. Poisson's ratio also showed variations, with values ranging from 0.234 in the 90° orientation to 0.464 in the 60° orientation. In general, specimens oriented at 45° and 60° to the rolling direction showed the lowest yield stress and tensile strength, while specimens with the orientation of 0° and 75°to the rolling direction had the highest. Table 5. represents an overview of the mechanical properties of CuFe2P sheets in different orientations relative to the rolling directions. Evaluation of data for determination of Lankford coefficients as constant or incremental value was done in [133].

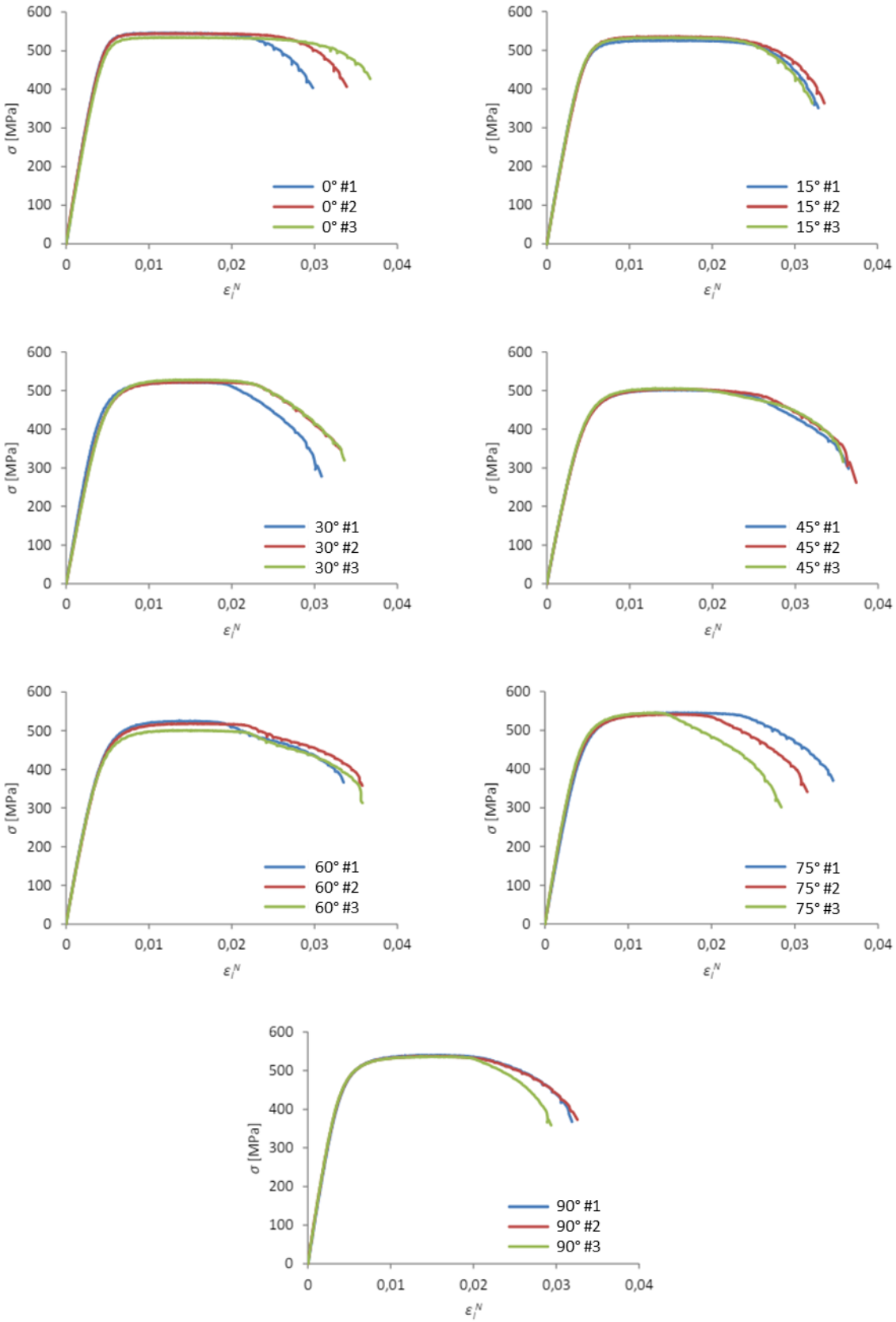

Figure 49. True stress-strain curve for CuFe2P specimens with seven different orientation to the rolling direction [133]

Table 7. Mechanical properties of CuFe2P sheets with seven different orientations relative to the rolling directions

Orientation	Sample	E [GPa]	ν	$\sigma_{0.01}$ [MPa]	$\sigma_{0.2}$ [MPa]	σ_M [MPa]
0°	1	128.5	0.271	364.29	537.48	545.59
	2	137.7	0.289	226.93	531.90	544.76
	3	120.7	0.307	365.97	524.43	534.56
15°	1	122.2	0.308	316.82	505.88	526.24
	2	117.7	0.275	319.61	517.15	535.92
	3	118.8	0.278	340.84	515.75	533.40
30°	1	121.9	0.452	329.23	491.63	522.06
	2	109.8	0.368	331.13	489.59	522.34
	3	108.7	0.38	320.35	494.08	528.04
45°	1	110.9	0.434	233.34	463.77	501.97
	2	111.1	0.408	216.44	461.27	503.91
	3	114.4	0.438	205.80	463.24	505.75
60°	1	123.9	0.347	214.35	479.43	526.25
	2	120.1	0.464	222.00	476.25	518.88
	3	117.4	0.414	256.07	465.85	501.78
75°	1	117.4	0.281	303.37	505.49	545.16
	2	126.9	0.37	291.85	500.71	542.20
	3	129.2	0.305	289.07	506.66	545.90
90°	1	130.0	0.234	310.41	503.40	540.16
	2	143.3	0.361	227.20	494.82	537.35
	3	138.7	0.269	272.22	498.57	536.78

With the usage of longitudinal and lateral extensometers, it is possible to calculate the Lankford coefficient according to Equation (7). Lankford coefficients as constant values were calculated for two different strain ranges. One range covers up to 0.006 of true longitudinal plastic deformation ε_l^p, and another up to 0.013. For the approximation range $0 \leq \varepsilon_l^p \leq 0.006$, the values range from 0.64 to 2.07, while for the approximation range $0 \leq \varepsilon_l^p \leq 0.013$, slightly lower values are obtained, ranging from 0.74 to 2.34. In both cases, the highest values of the Lankford coefficient are obtained for samples oriented at 60°, while the lowest for specimens oriented in the rolling direction, as shown in Table 8.

Table 8. Representative values of the Lankford coefficient with seven different orientations relative to the rolling directions

Orientation	Lankford coefficient	
	$0 \leq \varepsilon_l^p \leq 0.006$	$0 \leq \varepsilon_l^p \leq 0.013$
0°	0.64	0.74
15°	0.80	0.80
30°	1.08	1.20
45°	1.41	1.65
60°	2.07	2.34
75°	1.69	1.47
90°	1.51	1.37

4.6. Conclusion of experimental investigation

Based on the obtained experimental data, the following conclusions are derived:

- The material considered shows pronounced anisotropy in all considered uniaxial tensile mechanical properties, i.e., the stress–strain curve, the elastic modulus, the tensile strength, the elongation, and the Lankford coefficient, which significantly depend on the specimen orientation relative to the rolling direction.

- An increase in strain rate generally resulted in increased values of tensile strength and elongation for all tested orientations, while the elastic modulus remained almost constant.

- The values of the Lankford coefficient are influenced by the strain rate; the lowest values were obtained for the lowest strain rate. By calculating the values of the Lankford coefficient at different values of longitudinal plastic strain, it is observed that this coefficient decreases with the ongoing deformation process. This alternation is most pronounced for the highest strain rate considered. These observations challenge the conventional assumption of the Lankford coefficient being constant.

- The inelastic heat fraction (IHF) varied with strain rate and specimen orientation relative to the rolling direction, indicating that the material capacity to convert plastic work into heat depends on loading conditions. Generally, IHF increases with strain rate, with samples oriented at 45° to the rolling direction exhibiting the highest values.

- The breaking angles assessed in the tensile tests performed show that specimen orientation influences fracture behaviour, while strain rate has a minor effect. The highest breaking angles were observed for specimens aligned with the rolling direction (0° orientation), while specimens oriented at 45° to the rolling direction exhibited the lowest breaking angles.

- Compression tests demonstrated that strain rate sensitivity is present for both material, pure copper and copper alloy (CuFe2P). With a strain rate increase, there is an increase in force during the defined displacement of the compression test. DIC and IR techniques showed that plastic deformation corresponds to heat generation localization.

- Crimping process was successfully performed on a uniaxial tensile test machine in a controlled environment. Although the DIC method was unable to capture clear images at higher strain rates, the IR method revealed heat generation for the estimation of plastic deformation localization.

- Deep drawing tests confirmed the material's anisotropic behaviour, with pronounced earrings in the formed cups, with the highest earring observed at 50° and the lowest at 90°.

- Tensile tests conducted on seven different orientations relative to the rolling direction confirmed the material's severe anisotropy. These results are needed for advanced constitutive models that describe anisotropic elasto-plastic material behaviour, like Yld2004-18P.

Chapter 5

Continuum plasticity

5.1. Elasticity and plasticity

The stress tensor (**σ**) is a mathematical representation of internal forces when a material is under external loads. It represents the intensity of internal forces through a specific plane, where each component of the tensor is representing the force per unit area [N/mm^2] acting in a particular direction. The stress tensor as a second-order tensor is written as 3x3 matrix for a three-dimensional stress state, equation (8). The diagonal elements represent normal stresses, which act perpendicular to the planes that correspond to the coordinate axes (1-2-3), while other elements represent shear stresses, acting parallel to the plane

$$\boldsymbol{\sigma} = \begin{bmatrix} \sigma_{11} & \sigma_{12} & \sigma_{13} \\ \sigma_{21} & \sigma_{22} & \sigma_{23} \\ \sigma_{31} & \sigma_{32} & \sigma_{33} \end{bmatrix}. \tag{8}$$

On the same principle, the strain tensor (**ε**) measures the deformation of a material as a response to the applied stress defined. The same as a stress tensor, the strain tensor is defined as a 3x3 matrix for 3D cases in which normal strain represents changes in length along the coordinate axes and shear strain represents changes in angle between two lines parallel to the coordinate axis being initially perpendicular

$$\boldsymbol{\varepsilon} = \begin{bmatrix} \varepsilon_{11} & \varepsilon_{12} & \varepsilon_{13} \\ \varepsilon_{21} & \varepsilon_{22} & \varepsilon_{23} \\ \varepsilon_{31} & \sigma_{32} & \varepsilon_{33} \end{bmatrix}. \tag{9}$$

Using Voigt notation, 3x3 matrix can be written as 6-dimensional vector. This approach is used in the finite element software Abaqus, utilized in this work. Therefore, the stress and strain vectors are written as follows

$$\boldsymbol{\sigma} = [\sigma_{11}\ \sigma_{22}\ \sigma_{33}\ \sigma_{12}\ \sigma_{23}\ \sigma_{31}], \tag{10}$$

$$\boldsymbol{\varepsilon} = [\varepsilon_{11}\ \varepsilon_{22}\ \varepsilon_{33}\ \varepsilon_{12}\ \varepsilon_{23}\ \varepsilon_{31}]. \tag{11}$$

Tensor invariants are scalar quantities derived from tensors that remain unchanged by rotation of the coordinate system. In the context of continuum mechanics, tensor invariants are particularly useful because they enable description of the material behaviour in a manner that is independent of the specific orientation of the material in space. Figure 50. presents the rotation of a Cartesian coordinate system in the context of anisotropic materials. For the context of sheet metal rolling, the rolling and transverse directions are indicated, which are critical in describing the material's anisotropic properties:

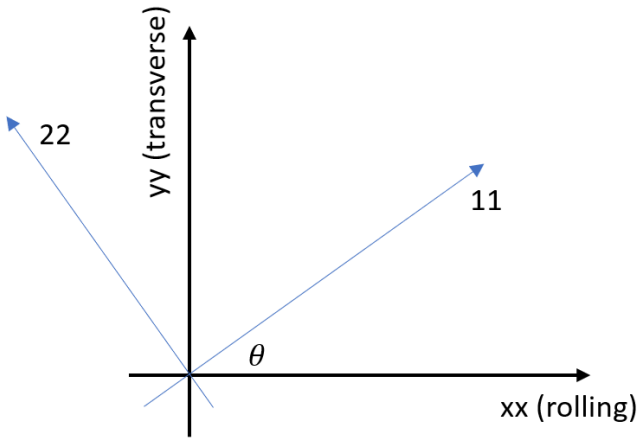

Figure 50. Illustration of rotation of a Cartesian reference base

$$\begin{bmatrix}\sigma_{xx}\\ \sigma_{yy}\\ \sigma_{zz}\end{bmatrix} = \begin{bmatrix}\cos^2\theta & \sin^2\theta & -2\cos\theta\sin\theta\\ \sin^2\theta & \cos^2\theta & 2\cos\theta\sin\theta\\ \cos\theta\sin\theta & -\cos\theta\sin\theta & \cos^2\theta-\sin^2\theta\end{bmatrix}\begin{bmatrix}\sigma_{11}\\ \sigma_{22}\\ \sigma_{12}\end{bmatrix}, \tag{12}$$

$$\begin{bmatrix}\varepsilon_{xx}\\ \varepsilon_{yy}\\ \gamma_{zz}\end{bmatrix} = \begin{bmatrix}\cos^2\theta & \sin^2\theta & -\cos\theta\sin\theta\\ \sin^2\theta & \cos^2\theta & \cos\theta\sin\theta\\ 2\cos\theta\sin\theta & -2\cos\theta\sin\theta & \cos^2\theta-\sin^2\theta\end{bmatrix}\begin{bmatrix}\varepsilon_{11}\\ \varepsilon_{22}\\ \gamma_{12}\end{bmatrix}. \tag{13}$$

The stress invariants are defined as the coefficients of the characteristic polynomial of the stress tensor. For a 3D stress state, these invariants are typically denoted as I_1, I_2 and I_3 and are calculated as follows:

$$I_1 = \sigma_1 + \sigma_2 + \sigma_3 \quad (14)$$

$$I_2 = \sigma_1\sigma_2 + \sigma_2\sigma_3 + \sigma_3\sigma_1 \quad (15)$$

$$I_3 = \sigma_1\sigma_2\sigma_3 \quad (16)$$

where σ_1, σ_2 and σ_3 are the principal stresses. Data for describing a new constitutive model are based on the experimental investigation. In most cases, simple tensile tests performed on tensile test machines, with contact or non-contact extensometer, would be basis for material behaviour definition. As tensile test machine is measuring force applied on specimen, while extensometer is measuring elongation, stress value can be defined as

$$\sigma_0 = \frac{F}{A_0} \quad (17)$$

and deformation as

$$\varepsilon = \frac{\Delta l}{l_0}, \quad (18)$$

where A_0 is initial cross-section area of the specimen and l_0 is initial length of two measured points of the extensometer, most common initial length of l_0 is 50 mm. In case, diagram based on equation (15) and (16) is plotted, it would represent engineering stress strain curve, according to the Figure 51. On the graph, two points are noted, Y as yield point up to which material is acting elastically and M as ultimate strength up to which material is stable. After M point, necking of tensile test specimen and failure with further elongation of specimen is expected.

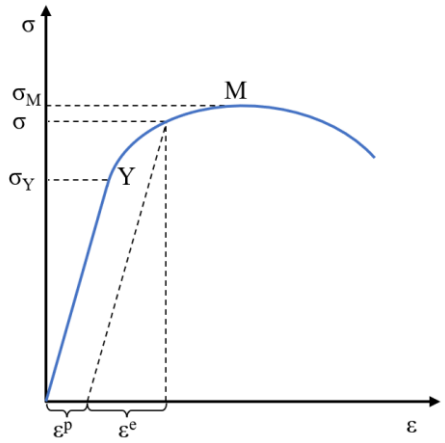

Figure 51. Engineering stress strain curve graph

The theory of linear elasticity can be applied for cases where material exhibits small strain and where object will return to original shape when load is removed, while the theory of plasticity is dealing with the larger strains where stress will reach the yield point. Unlike elasticity, which is reversible, plastic deformation leads to a permanent change of shape after the load is removed. With the decomposition of the elastic and plastic strain rates, the strain increment can be split into elastic and plastic components:

$$\mathrm{d}\varepsilon = \mathrm{d}\varepsilon^{\mathrm{e}} + \mathrm{d}\varepsilon^{\mathrm{p}}, \tag{19}$$

where dε, dε^e and dε^p represent increments of total strain, elastic strain and plastic strain. The Hooke's law is describing material behaviour at small strains, when material is in reversible, linear, condition. The incremental form of Hooke's law can be written as

$$\mathrm{d}\sigma = \mathbf{C}\,\mathrm{d}\varepsilon^e = \mathbf{C}\,(\mathrm{d}\varepsilon - \mathrm{d}\varepsilon^p), \tag{20}$$

where elastic stiffness matrix or elasticity tensor (**C**) defined as

$$\mathbf{C} = \begin{bmatrix} \lambda + 2G_{\mathrm{s}} & \lambda & \lambda & 0 & 0 & 0 \\ \lambda & \lambda + 2G_{\mathrm{s}} & \lambda & 0 & 0 & 0 \\ \lambda & \lambda & \lambda + 2G_{\mathrm{s}} & 0 & 0 & 0 \\ 0 & 0 & 0 & G_{\mathrm{s}} & 0 & 0 \\ 0 & 0 & 0 & 0 & G_{\mathrm{s}} & 0 \\ 0 & 0 & 0 & 0 & 0 & G_{\mathrm{s}} \end{bmatrix}, \tag{21}$$

with lame constant (λ) and shear modulus (G_{s}) are defined as:

$$\lambda = \frac{\mathrm{E}\nu}{(1-2\nu)(1+\nu)}, \tag{22}$$

$$G_{\mathrm{s}} = \frac{E}{2(1+\nu)}, \tag{23}$$

where E and ν are Young's modulus and Poisson's ratio, respectively.

It was proven that the volume of a material element remains constant during plastic deformation, implying that the material density does not change as a result of external forces [134,135]. This assumption simplifies the constitutive equations and is especially relevant for sheet metal plasticity theories. The Lankford coefficient is a direct consequence of the incompressibility hypothesis. Since the volume remains constant, any increase in length must

be accompanied by a decrease in the other two dimensions. The *r*-value quantifies this relationship in the plane of the sheet (width and thickness).

$$\mathrm{d}\varepsilon = \mathrm{d}\varepsilon_{11}^{\mathrm{p}} + \mathrm{d}\varepsilon_{22}^{\mathrm{p}} + \mathrm{d}\varepsilon_{33}^{\mathrm{p}} = 0. \quad (24)$$

5.2. Yield criterion

A yield criterion is a theoretical model that predicts the conditions when material will begin to deform plastically. When yield criterion condition is met, the plastic deformation occurs. The yield criterion can be defined as

$$F(\boldsymbol{\sigma}) = f(\boldsymbol{\sigma}) - \sigma(\varepsilon^{\mathrm{p}}) = 0, \quad (25)$$

where $F(\boldsymbol{\sigma})$ is yielding criterion, $f(\boldsymbol{\sigma})$ is yield function and $\sigma(\varepsilon^{\mathrm{p}})$ is yield stress. Case in which $F(\boldsymbol{\sigma}) < 0$ represents elastic deformation of the material, acting reversible. If $F(\boldsymbol{\sigma}) = 0$, the material deforms plastically.

5.2.1. Isotropic yield criterion

The isotropic yield criterion is a fundamental concept in the field of plasticity that determines initiation of plastic deformation in materials for various states of stress. It is termed "isotropic" because it assumes that the material's properties are the same in all directions, meaning the material does not exhibit directional dependence or anisotropy.

Von Mises yield criterion, also known as the maximum distortion energy criterion, is one of the most utilized isotropic yield criteria. The yielding criterion is defined by the state at which the second invariant of the deviatoric part of the stress tensor reaches a critical value. It can be expressed as

$$\sigma_{\mathrm{v}}^2 = 3J_2 = \frac{1}{2}[(\sigma_{11} - \sigma_{22})^2 + (\sigma_{22} - \sigma_{33})^2 + (\sigma_{33} - \sigma_{11})^2] + 3(\sigma_{12}^2 + \sigma_{13}^2 + \sigma_{23}^2), \quad (26)$$

where σ_{v}^2 is the von Mises equivalent stress and J_2 is the second invariant of the deviatoric stress tensor.

The von Mises yield function for three-dimensional cases can be visualized as a yield surface in the principal stress space, as shown in Figure 52. This surface is a cylinder oriented along the hydrostatic axis, where $\sigma_1 = \sigma_2 = \sigma_3$.

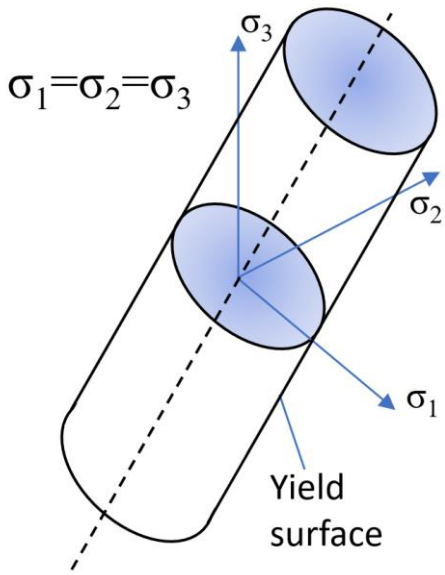

Figure 52. Von Mises yield surface in principal stress state

Tresca yield function which was proposed in 1864., and it is the oldest yield criterion for isotropic material behaviour. It is also known as the maximum shear stress criterion, and it is used to predict the yielding of ductile materials during complex loading conditions. It is based on the experimental observation that yielding occurs when the maximum shear stress in the material reaches a critical value, which is characteristic of the material. Tresca yield function can be written as

$$\frac{1}{2}\max\left(|\sigma_1-\sigma_2|,|\sigma_2-\sigma_3|,|\sigma_1-\sigma_3|\right) > \tau_{max}. \quad (27)$$

The Tresca criterion is more conservative than the von Mises criterion, meaning it predicts yielding at lower stress values. It is used in metal forming processes like extrusion and rolling, where shear stress plays a significant role. Tresca yield function for three-dimensional stress states can be visualized as a yield surface in the principal stress space, as shown in Figure 53. This surface is a hexagonal prism oriented along the hydrostatic axis, where $\sigma_1 = \sigma_2 = \sigma_3$.

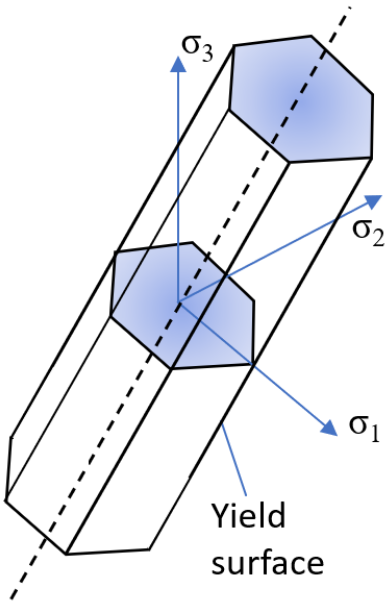

Figure 53. Tresca yield surface in principal stress state

5.2.2. Anisotropic yield criterion

Materials that exhibit direction-dependent properties are anisotropic materials. Unlike isotropic materials, which yield uniformly in all loading directions, anisotropic materials have different yield stresses and strain ratios along different orientations. This anisotropy is often a result of the material crystallographic texture and microstructural evolution during processes like rolling and heat treatment.

The Lankford coefficient (*r*-value) is a parameter for characterizing the anisotropic behaviour of sheet metals during plastic deformation. The Lankford coefficient is not a constant value but can vary depending on the strain level and the orientation of the specimen with respect to the rolling direction. For instance, r_0, r_{45} and r_{90} represent the Lankford coefficients measured at 0 degrees, 45 degrees and 90 degrees to the rolling direction. It is defined as the ratio of the true plastic strain in the width direction to the true plastic strain in the thickness direction during uniaxial tensile testing, according to equation (7).

Normal (R_n) and planar anisotropy (ΔR) are based on Lankford values calculated for tree rolling directions - r_0, r_{45} and r_{90}. Normal anisotropy represents resistance to thinning, related to earing defects during the deep drawing process. The ideal material for the deep drawing process would have $R_n > 1$ and $\Delta R = 0$ [136]. Material with anisotropic behaviour would have $R_n \neq 1$ and $\Delta R \neq 0$, where

$$R_n = \frac{r_0+2r_{45}+r_{90}}{4}, \quad (28)$$

$$\Delta R = \frac{r_0-2r_{45}+r_{90}}{2}. \quad (29)$$

The yield criterion for an anisotropic material is a mathematical representation that defines the onset of plastic deformation for various stress states. The most basic form of an anisotropic yield criterion is Hill's quadratic yield function [137]. This criterion extends the isotropic von Mises yield function, by incorporating additional parameters that account for the material's anisotropic behaviour. Hill's function is defined by a quadratic form that relates the stress components to a set of material constants that describe the anisotropy. Despite its simplicity and ease of use in numerical simulations, Hill's criterion often falls short in accurately predicting the complex yielding behaviour, especially aluminium alloys, which can exhibit anomalous behaviours not captured by this criterion.

5.2.3. Hill1948 function

The Hill 1948 yield function is a mathematical model used to describe the yielding behaviour of anisotropic materials. This yield function is implemented in the finite element (FE) program ABAQUS and is defined as

$$\sigma^2 = F(\sigma_{22}-\sigma_{33})^2 + G(\sigma_{33}-\sigma_{11})^2 + H(\sigma_{11}-\sigma_{22})^2 + 2L\sigma_{23}^2 + 2M\sigma_{13}^2 + 2N\sigma_{12}^2, \quad (30)$$

where σ_{11}, σ_{22} and σ_{33} are the normal stress components, while σ_{12}, σ_{13} and σ_{23} are the shear stress components. The coefficients *F, G, H, L, M* and *N* are anisotropic parameters that characterize the material's response to different stress states. These parameters can be calculated as follows:

$$F = \frac{1}{2}\left(\frac{1}{R_{22}^2} + \frac{1}{R_{33}^2} - \frac{1}{R_{11}^2}\right), \quad (31)$$

$$G = \frac{1}{2}\left(\frac{1}{R_{33}^2} + \frac{1}{R_{11}^2} - \frac{1}{R_{22}^2}\right), \quad (32)$$

$$H = \frac{1}{2}\left(\frac{1}{R_{11}^2} + \frac{1}{R_{22}^2} - \frac{1}{R_{33}^2}\right), \quad (33)$$

$$L = \frac{3}{2R_{23}^2}, \quad (34)$$

$$M = \frac{3}{2R_{13}^2}, \tag{35}$$

$$N = \frac{3}{2R_{13}^2}, \tag{36}$$

where R_{11}, R_{22}, R_{33}, R_{23}, R_{13} and R_{12} are the material's anisotropic yield stress ratios. These ratios are determined from experimental data and reflect the directional dependence of the yield stress in the material.

5.2.4. Yld2004-18P function

The Barlat′s Yld2004-18P yield function is an advanced anisotropic yield criterion designed to model the yielding behavior of anisotropic materials, particularly metals with complex anisotropy like aluminum alloys. This function is implemented in the finite element (FE) software ABAQUS starting from version 2019, and is defined as

$$\sigma^m = \frac{1}{4}\left(\left|\tilde{S}_1' - \tilde{S}_1''\right|^m + \left|\tilde{S}_1' - \tilde{S}_2''\right|^m + \left|\tilde{S}_1' - \tilde{S}_3''\right|^m + \left|\tilde{S}_2' - \tilde{S}_1''\right|^m + \left|\tilde{S}_2' - \tilde{S}_2''\right|^m + \left|\tilde{S}_2' - \tilde{S}_3''\right|^m + \left|\tilde{S}_3' - \tilde{S}_1''\right|^m + \left|\tilde{S}_3' - \tilde{S}_2''\right|^m + \left|\tilde{S}_3' - \tilde{S}_3''\right|^m\right), \tag{37}$$

where m is the exponent related to material crystal plasticity and $\tilde{S}_i', \tilde{S}_i''$ are principal values of stress tensors $\tilde{\boldsymbol{S}}'$ and $\tilde{\boldsymbol{S}}''$. The stress tensors are defined by two linear transformations of the deviatoric stress $\boldsymbol{S}$. The associated linear transformations on the stress deviator are

$$\mathbf{C}' = \begin{bmatrix} 0 & -c_{1212}' & -c_{1313}' & 0 & 0 & 0 \\ -c_{2211}' & 0 & -c_{2233}' & 0 & 0 & 0 \\ -c_{3311}' & -c_{3322}' & 0 & 0 & 0 & 0 \\ 0 & 0 & 0 & c_{1212}' & 0 & 0 \\ 0 & 0 & 0 & 0 & c_{1313}' & 0 \\ 0 & 0 & 0 & 0 & 0 & c_{2323}' \end{bmatrix}, \tag{38}$$

$$\mathbf{C}'' = \begin{bmatrix} 0 & -c_{1122}'' & -c_{1133}'' & 0 & 0 & 0 \\ -c_{2211}'' & 0 & -c_{2233}'' & 0 & 0 & 0 \\ -c_{3311}'' & -c_{3322}'' & 0 & 0 & 0 & 0 \\ 0 & 0 & 0 & c_{1212}'' & 0 & 0 \\ 0 & 0 & 0 & 0 & c_{1313}'' & 0 \\ 0 & 0 & 0 & 0 & 0 & c_{2323}'' \end{bmatrix}, \tag{379}$$

where c_{ijkl}' and c_{ijkl}'' represents anisotropy parameters, 18 in total.

5.3. Material hardening

Material hardening occurs in ductile metals as they are plastically deformed. During plastic deformation, dislocations within the metal crystal lattice structure will occur. As the dislocations rise, their movement becomes more difficult, representing the material's resistance to further deformation. As a result of this increased resistance, the material will have a higher yield stress. Hardening is a critical aspect in metal forming processes as it affects the force required to shape the material and can also influence the material's ductility. The degree of hardening is dependent on factors such as the amount and type of deformation, the material's initial microstructure and its composition. Understanding and accurately modelling material hardening is essential for realistic predicting the behaviour of metals during manufacturing processes.

5.3.1. Isotropic hardening

Isotropic hardening is a concept that describes a specific type of hardening behaviour observed in materials during plastic deformation. When material undergoes isotropic hardening, its yield surface in the stress space expands uniformly in all directions without changing its shape or position. It means that the material resistance to plastic deformation equally increases in all loading directions. The increase in yield stress with plastic deformation is often represented by a hardening variable such as equivalent plastic strain. This model is particularly useful for materials that exhibit a proportional relationship between stress and strain beyond the initial yield point and do not show directional dependency in their hardening behaviour.

In mathematical terms, isotropic hardening can be expressed by a yield function that changes size, but the shape remains constant as a function of the hardening variable. The yield function is usually associated to the von Mises yield criterion for isotropic materials. Hardening is quantified by an increase in the equivalent stress with the ongoing deformation. This assumption simplifies constitutive modelling of materials, but may neglect the evolution of texture and anisotropy that could occur during forming processes. Some of the known isotropic hardening laws are the following:

$$\sigma^{\mathrm{iso}} = \sigma_0 + K\,(\varepsilon^{\mathrm{p}})^n \qquad \text{Ludwick (1909)} \qquad (40)$$

$$\sigma^{\mathrm{iso}} = K\,(\varepsilon^{\mathrm{p}})^n \qquad \text{Hollomon (1944)} \qquad (41)$$

$$\sigma^{\text{iso}} = \sigma_0 + Q(1 - e^{-b\varepsilon^{\text{p}}}) \quad \text{Voce (1948)} \quad (42)$$

$$\sigma^{\text{iso}} = K\,(\varepsilon_0^{\text{p}} + \varepsilon^{\text{p}}) \quad \text{Swift (1947)} \quad (43)$$

$$\sigma^{\text{iso}} = \sigma_0 \tanh(E\varepsilon^{\text{p}}/\sigma_0) \quad \text{Swift (1947)} \quad (44)$$

where σ_0 is the initial yield stress, K is a strength coefficient, ε^{p} is equivalent plastic strain, n is a strain hardening exponent, Q is saturation parameter and b is material constant related to the rate of hardening.

Figure 54 shows a uniform increase of the yield surface in all directions. When material is loaded in tension to point T and then unloaded and compressed to point C, the stress value in both points will be the same: $|\sigma_{\text{T}}| = |\sigma_{\text{C}}|$.

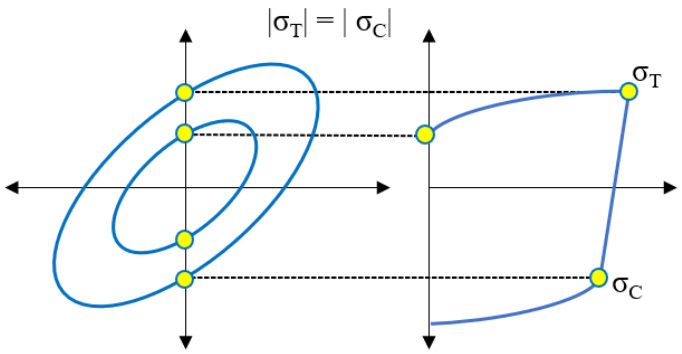

Figure 54. Concept of isotropic hardening

5.3.2. Kinematic hardening

When a metal is stressed in one direction and plastically deformed, it undergoes work hardening, which increases its yield strength. However, if the direction of loading is reversed, the material will exhibit a lower yield stress than it was in the initial loading direction. This reduction in yield stress is known as the Bauschinger effect. These internal changes lead to an asymmetry in the stress-strain response, where the material "remembers" its loading history and responds differently to tensile or compressive load. Understanding and accounting for the Bauschinger effect is important for accurately predicting the behaviour of materials in applications where there would be a change in loading direction. For example, in the production of a terminal and other sheet metal forming processes.

Translation of the yield surface in stress space can be seen in Figure 55. When material is loaded in tension up to point T and then compressed up to point C, stress value would be different. In this example $|\sigma_T| > |\sigma_C|$.

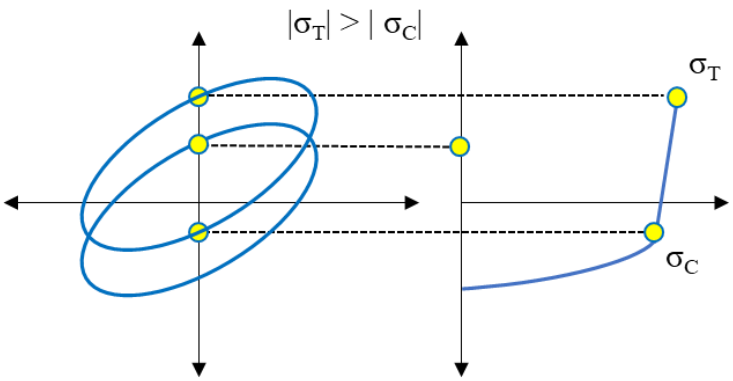

Figure 55. Concept of kinematic hardening

5.3.3. Anisotropic hardening

In isotropic hardening, a material's resistance to deformation increases uniformly regardless of the loading direction. On the contrary, anisotropic hardening introduces variation in hardening behaviour depending on to the load direction. This is commonly observed in metal sheets, as they are produced with a rolling process. The anisotropic nature of hardening is often characterized by the evolution of the yield surface in the stress space, which may expand, translate or distort non-uniformly with plastic deformation [138]. Constitutive models attempt to capture this behaviour by including directional hardening rules and anisotropy coefficients, which are calibrated using experimental data from tests conducted in different orientations relative to the material's processing direction [139]. Implementation of anisotropic hardening is beneficial for predicting the material response in complex loading conditions, such as the crimping process, to more accurately predict crimp shape and springback.

5.4. Associated and non-associated flow rule

The associated flow rule (AFR) is based on the principle of normality, which states that the plastic strain increment vector is normal to the yield surface at the current stress point in the stress space. This flow rule means that the plastic potential function $f_p(\boldsymbol{\sigma})$, from which the direction of plastic flow is derived, is the same as the yield function $f_y(\boldsymbol{\sigma})$.

$$f_p(\boldsymbol{\sigma}) = f_y(\boldsymbol{\sigma}) \tag{45}$$

In mathematical terms, the associated flow rule can be expressed as:

$$\mathrm{d}\boldsymbol{\varepsilon}^{\mathrm{p}} = \mathrm{d}\lambda \frac{\partial f_y(\boldsymbol{\sigma})}{\partial \boldsymbol{\sigma}} \tag{46}$$

where dλ is a plastic multiplier.

This condition simplifies the formulation of constitutive models and is widely used in the analysis of isotropic materials. However, it may not always accurately describe the behaviour of anisotropic materials, where a non-associated flow rule might be more appropriate.

The non-associated flow rule (non-AFR) negates the assumption that the yield function and the plastic potential are identical. Instead, it allows for the plastic potential to be a different function from the yield criterion.

$$f_p(\boldsymbol{\sigma}) \neq f_y(\boldsymbol{\sigma}) \tag{47}$$

This means that the direction of plastic strain increment is not necessarily normal to the yield surface. The non-associated flow rule can be mathematically expressed as:

$$\mathrm{d}\boldsymbol{\varepsilon}^{\mathrm{p}} = \mathrm{d}\lambda \frac{\partial f_p(\boldsymbol{\sigma})}{\partial \boldsymbol{\sigma}} \tag{48}$$

The non-associated flow rule is particularly useful for materials where the plastic volume change is significant or where the yield behaviour is pressure sensitive. It allows for a more accurate representation of the material behaviour under complex loading conditions. In the context of sheet metal forming, non-associated flow rule can better predict phenomena like earing, springback, and orientational dependence of uniaxial plastic material properties. Differences in geometric interpretation of these concepts for plane stress state can be seen in Figure 56.

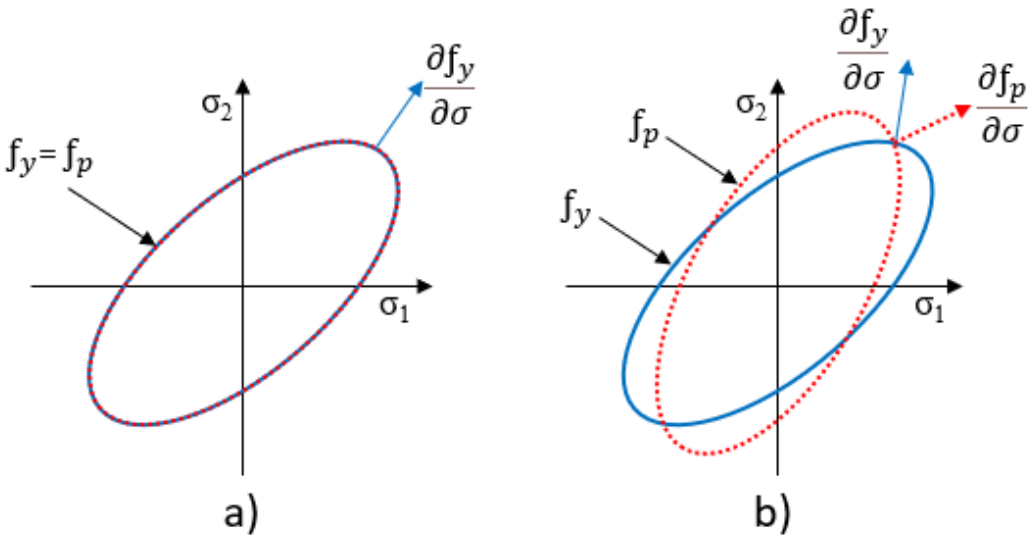

Figure 56. Geometrical interpretation of a) AFR and b) non-AFR flow rule

5.5. Thermoplasticity

In plastic deformation, the mechanical work done on a material is not fully recoverable, and a portion of it is converted into heat. Consequently, temperature will rise in the material. The ratio of the work converted into heat is characterized by a material-specific parameter often denoted as the Taylor-Quinney coefficient or β, which represent inelastic heat fraction. The heat generated during plastic deformation locally increases the temperature of the material. High temperature rise can affect the material mechanical properties, such as yield stress and elongation, often leading to thermal softening. The distribution and dissipation of this heat are governed by Fourier's law. Accurate modelling of the temperature distribution within a deforming material requires coupling the mechanical analysis of plasticity with thermal analysis, where Fourier's law plays a crucial role.

$$q_s = -k\frac{\partial T}{\partial n} \tag{49}$$

where k is coefficient of thermal conductivity and $\frac{\partial T}{\partial n}$ is temperature gradient.

Thermal plasticity is observed in high-speed deformation processes where the adiabatic condition can lead to temperature increases. Experimental study of thermoplasticity involves the usage of techniques like infrared thermography to measure temperature fields and digital

image correlation to capture strain fields. Based on experimental investigation amount of mechanical work which is converted into heat can be calculated (3).

Chapter 6

Numerical implementation

6.1. Constitutive models

6.1.1. Strain rate dependent material plasticity

To accurately simulate material behaviour for different loading velocities, it is essential to incorporate strain rate effect into constitutive models. As the crimping process in this study involves two different materials, pure copper (Cu-ETP) for wire strands and copper alloy (CuFe2P) for the terminal, they need to be defined separately. Based on the experimental data from Figure 22, Cu-ETP and CuFe2P elastic behaviour is defined according to Table 9.

Table 9. Elastic modulus and Poisson′s ratio for CuFe2P and Cu-ETP sheets

	Young's modulus [GPa]	**Poisson's ratio**
CuFe2P	130	0.33
Cu-ETP	110	0.33

Experimental research revealed that Young′s modulus is not influenced by the strain rate, while it has an impact on material plasticity behaviour. Based on stress-strain curves obtained in the experimental investigations, Figure 57 presents true stress-plastic strain curves for strain rates of 0 s^{-1}, 0.2 s^{-1}, 1 s^{-1} and 5.65 s^{-1}. When defining the strain rate effect on material plasticity in ABAQUS software, it is necessary to define the static strain rate (0 s^{-1}), which corresponds to the quasistatic strain rate (0.0002 s^{-1}) from experimental investigations.

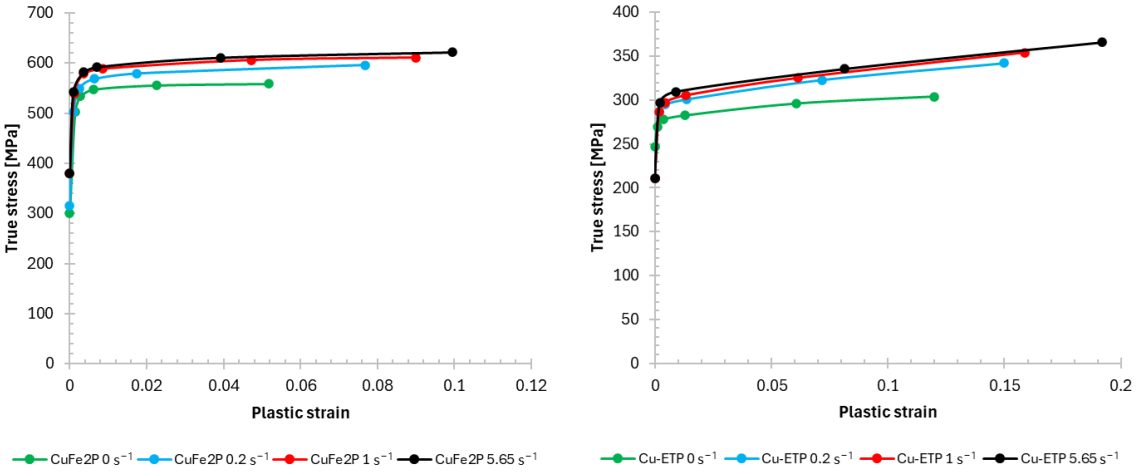

Figure 57. True stress-plastic strain curves for CuFe2P and Cu-ETP sheets at various strain rates

6.1.2. Anisotropy

The Finite Element Method (FEM) applies anisotropic material behaviour by discretizing a model into elements with direction-dependent behaviours. In this study, plastic anisotropy behaviour of CuFe2P sheets was modelled. Depending on the complexity of the anisotropic model, there is a need for a several parameters. For example, the Hill48 criterion needs a minimum of four parameters for plane stress, while Yld2004-18P criterion requires eighteen anisotropic parameters for 3D stress state. Both of these anisotropic yield criteria use one of the basic plastic material data - Lankford coefficients (*r*-values).

6.1.2.1. Hill-1948 anisotropy parameters

Equation (30) for Hill-1948 has been presented in overview of anisotropic yield criterion, where anisotropic parameters *F*, *G*, *H*, *L*, *M* and *N* are needed. For case of planar anisotropy, such as in the deep drawing process, implementation into ABAQUS is simplified. For planar anisotropy

$$r_0 \neq r_{90} \tag{50}$$

due to which

$$R_{11} \neq R_{22} \neq R_{33} \tag{51}$$

In the case reference yield stress σ^0 in metal plasticity model is equal to σ_{11} then

$$R_{11} = \frac{\sigma_{11}}{\sigma^0} = 1 \tag{52}$$

for planar anisotropy

$$R_{11} = R_{13} = R_{23} = 1 \tag{53}$$

and other three anisotropic yield stress ratios are defined as

$$R_{22} = \sqrt{\frac{r_{90}(r_0+1)}{r_0(r_{90}+1)}} \tag{54}$$

$$R_{33} = \sqrt{\frac{r_{90}(r_0+1)}{(r_0+r_{90})}} \tag{55}$$

$$R_{12} = \sqrt{\frac{3r_{90}(r_0+1)}{(2r_{45}+1)(r_0+r_{90})}} \tag{56}$$

According to Lankford values from experimental data (Figure 29), the anisotropic yield strain ratio used in Hill-1948 criterion implemented into Abaqus can be seen in Table 10. For calculating anisotropic yield strain ratios two sets of *r*-values are utilized: those corresponding to the quasistatic strain rate of 0.0002 s^{-1} and the highest achievable strain rate 5.65 s^{-1}.

Table 10. Anisotropic yield strain ratio at two different strain rates for Hill-1948 stress function

	R_{11}	R_{22}	R_{33}	R_{12}	R_{13}	R_{23}
0.0002 s^{-1}	1	1.13	0.98	0.92	1	1
5.65 s^{-1}	1	1.18	1.03	0.93	1	1

6.1.2.2. Yld2004-18P anisotropy parameters

The anisotropy parameters for the Yld2004-18P model were determined using experimental data and an optimization procedure implemented via a MATLAB script [140]. The script is iteratively optimizing eighteen parameters to find the most appropriate values. The optimization algorithm is minimizing the difference between the experimentally measured flow stresses and *r*-values and the corresponding values predicted by the Yld2004-18P model, based

on the weight factors. Figure 58. presents the end of the optimization process for the determination of Yld2004-18P anisotropy parameters. The close agreement between experimental and simulation curves indicates the accuracy of the parameter fitting.

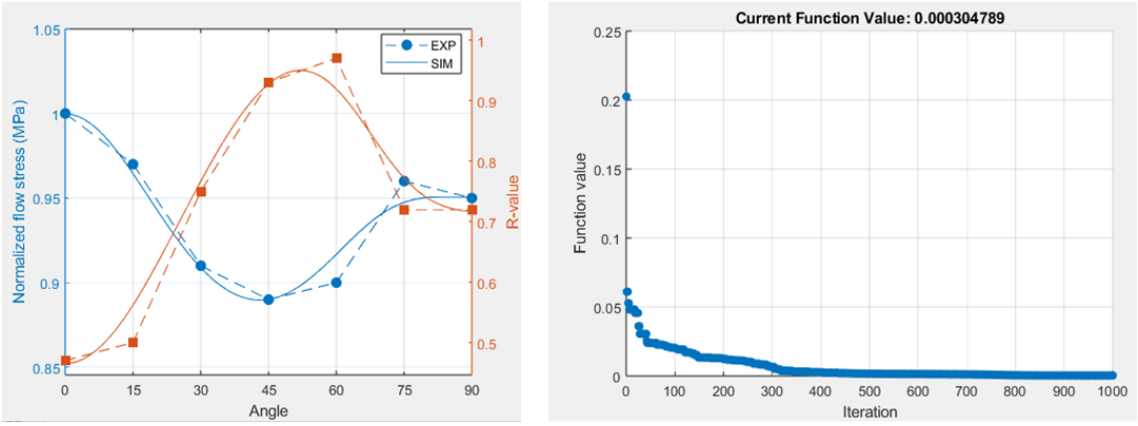

Figure 58. Optimization of Yld2004-18P anisotropy parameters using MATLAB script for CuFe2P sheet

Optimized anisotropy parameters for the Yld2004-18P yield criterion of CuFe2P sheets are shown in Table 11. These parameters define the directional dependence of the yield surface and can be input into ABAQUS software in the given format. A crystal structure exponent value of 8 was used, as it is most commonly used for Face Cubic Centre (FCC) materials [141].

Table 11. Yld2004-18P anisotropy parameters for CuFe2P sheets

C'_{1122}	C'_{1133}	C'_{2211}	C'_{2233}	C'_{3311}	C'_{3322}	C'_{1212}	C'_{1313}	C'_{2323}
0.99797	0.61214	1.14420	0.71314	1.05450	0.56936	0.54510	0.67145	0.43340
C''_{1122}	C''_{1133}	C''_{2211}	C''_{2233}	C''_{3311}	C''_{3322}	C''_{1212}	C''_{1313}	C''_{2323}
0.59825	1.08820	0.86053	1.20260	1.07960	1.32330	0.45027	0.84130	0.61495

6.1.3. Thermoplasticity

To simulate thermoplastic behaviour and capture temperature change during the deformation process, it is necessary to use an appropriate constitutive model. The amount of mechanical work which is transferred into heat (β) was determined in experimental investigations and

shown in Table 4. Although it was shown that β is being influenced by strain rate and specimen orientation to the rolling direction, it was defined as a constant value. By averaging the directional β values at the highest strain rate, a constant value of $\beta = 0.8$ was calculated. Other thermal material parameters are shown in Table 12. When defining thermal properties, it is necessary to have consistency with units. For mechanical engineering, most commonly SI (mm) units are used for input into ABAQUS software, which means that mass unit is measured in tonnes. To make a more straightforward conversion from tonne (SI units in mm) to kg (SI units in m) for thermal material properties, conversion was implemented in the table.

Table 12. Thermal material properties for CuFe2P and Cu-ETP

	CuFe2P		Cu-ETP	
	SI (m)	**SI (mm)**	**SI (m)**	**SI (mm)**
Density	8900	8.9×10^{-9}	8900	8.9×10^{-9}
Thermal conductivity	262	262	394	394
Specific heat	380	3.8×10^{8}	394	3.94×10^{8}
Inelastic heat fraction	0.8	0.8	0.8	0.8
Thermal expansion coeff.	16.3	16.3	17.7	17.7

6.2. Numerical models

6.2.1. Deep drawing process simulation

The Finite Element Analysis (FEA) model for the cup deep drawing is designed to replicate the experimental setup of a deep drawing process. A cylindrical blank with diameter of 65 mm is placed on top of die and pressured with force equal to 930 N via blank holder. Punch is displaced for 30 mm to form a cup from a cylindrical blank. To simplify the numerical model and decrease computation time, only quarter of CAD geometry is used. Die, punch and blank holder are modelled as rigid shell, while blank is modelled as solid body. To find the optimal mesh density, different scenarios were numerically modelled according to Table 13.

Table 13. Model data utilized for determination of mesh influence on numerical simulations of cup deep drawing

Case	Mesh density		Element type	Number of elements	Number of nodes
	Global	Thickness			
1	2	2	C3D8R	480	807
2	1	2	C3D8R	2106	3342
3	1	4	C3D8R	4212	5570
4	0.5	4	C3D8R	16116	20730
5	0.5	6	C3D8R	24174	29022
6	0.25	6	C3D8R	96696	114443
7	0.25	8	C3D8R	128928	147141

The solution convergence was investigated with usage of elasto-plastic isotropic material model. The convergences of displacement and force were carried out on seven different mesh densities according to the Figure 59. Based on the results, the proposed optimal mesh density for the circular corresponds to case 5, which consists of 24174 elements C3D8R with 6 elements per blank thickness. Chosen mesh density gave below 1% error in results for both, punch force and cup height, when compared to case 7, while being computation cost reasonable.

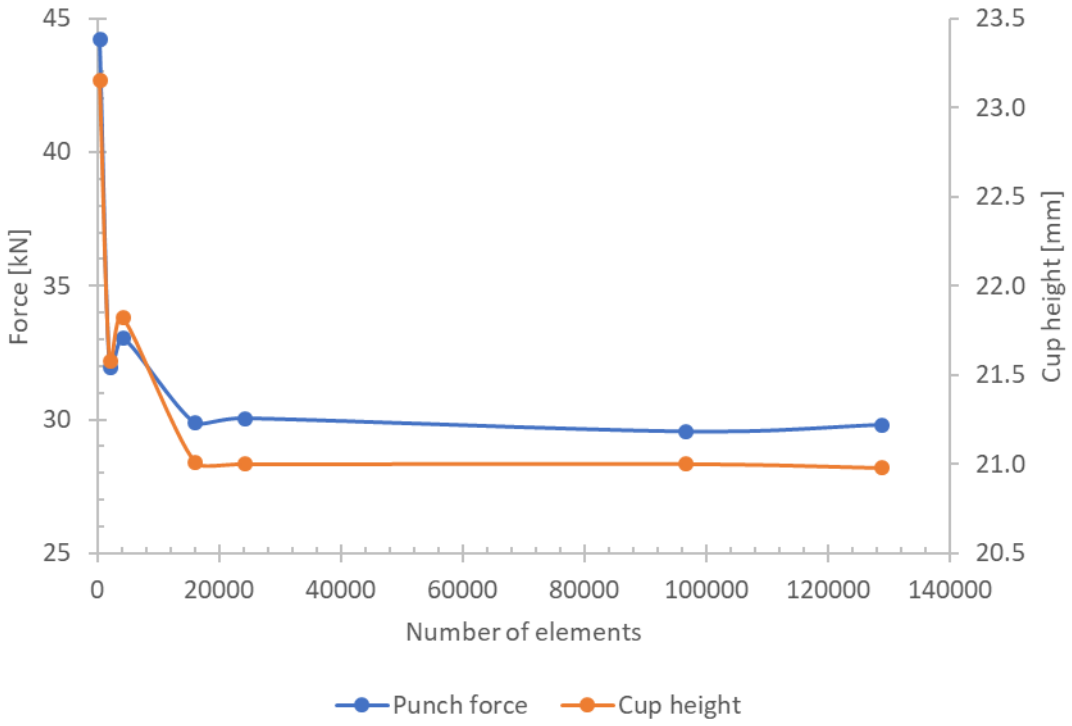

Figure 59. Force and cup height convergence for cup deep drawing

One-quarter of discretized model, according to the case 5, is presented in Figure 60, where solid elements C3D8R and shell elements S4R were used. The simulation was conducted in Abaqus/Explicit, with a coefficient of friction of 0.1. Validation of the model was indicated by a correlation between the simulated and experimental cup shapes and force-displacement curves, with aim to confirm the model's ability to predict the anisotropic plastic deformation of CuFe2P during deep drawing.

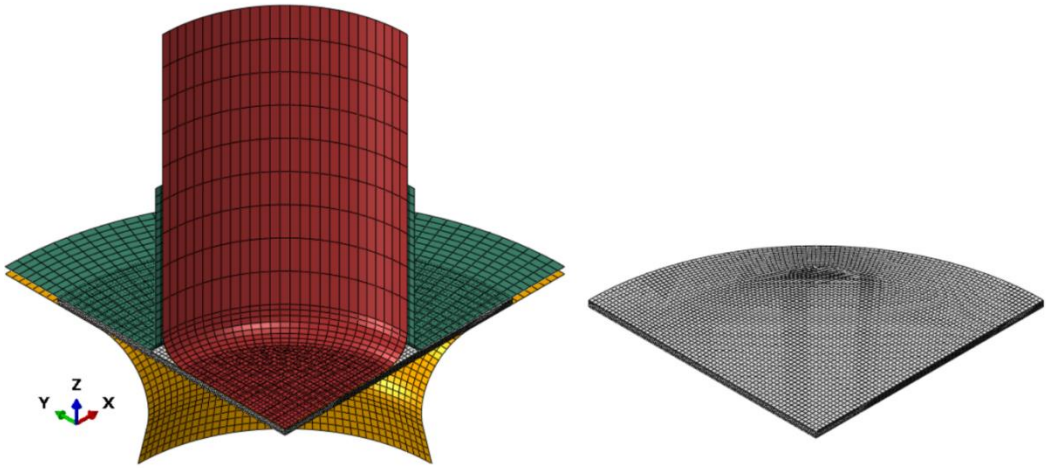

Figure 60. FEA model of cup deep drawing process in the finite element (FE) program Abaqus

6.2.2. Compression test simulation

The compression test setup consists of seven Cu or CuFe2P plates arranged in a stack. Each plate had dimensions of 17.5 mm in length and 7.5 mm in width, with the entire stack being compressed by a 7 mm thick tool. The tool was designed to apply a uniform pressure across the top surface of the upper plate, ensuring consistent deformation throughout the stack. The aim of this numerical model is to provide additional insights into the deformation mechanics of multi-layered metal stacks under compression, which is close to the crimping process. Initial compression test experimental and numerical results are shown in [142], after which new experimental setup was made and numerically described.

Numerical model of the experimental setup was defined with tools being rigid and discretized by S4R elements, while plates were discretized with solid C3D8RT elements. These 3D elements, with reduced integration, have thermal coupling capabilities, which is needed to evaluate material thermoplasticity. Several different mesh densities were analysed with force convergence criterion, and the optimal model of non-standard compression test is shown in Figure 61. Each plate is discretized with 36 000 C3D8RT elements.

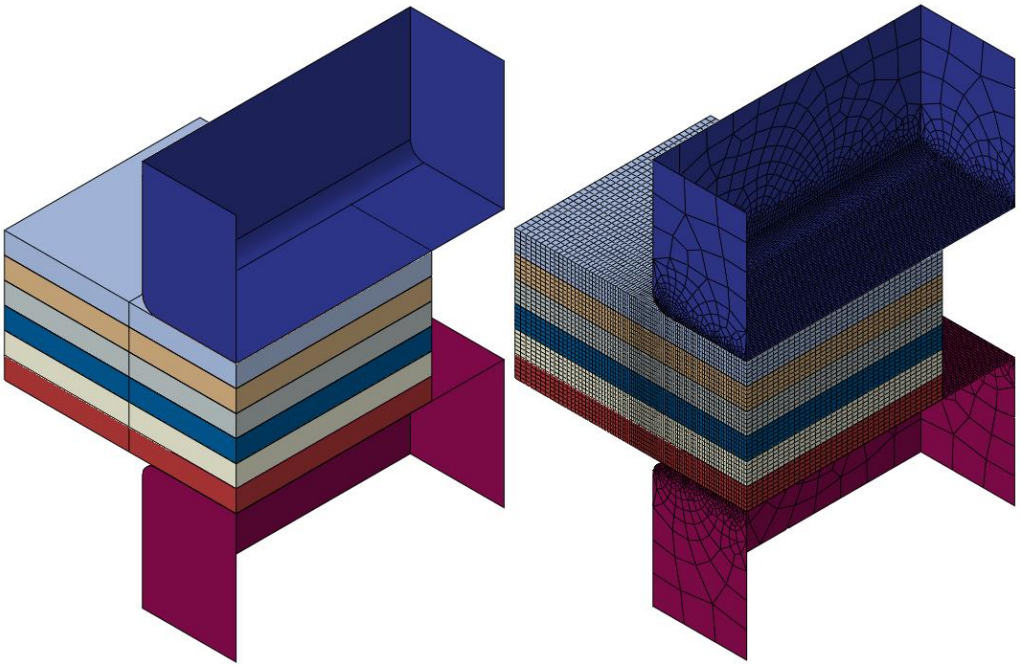

Figure 61. Numerical model of plate compression in the finite element (FE) program Abaqus

During plate compression two heat sources will increase material temperature, the mechanical work converted into heat and the friction between the copper sheets. The inelastic heat fraction β is defined as 0.8, while the coefficient of friction is set to 0.15. All frictional energy is

assumed to convert into thermal energy. The complete process is considered adiabatic, with no heat exchange with the environment. The displacement velocities used are the same as in the experimental investigation: 0.1, 10 and 50 mm/s.

6.2.3. Wire crimping process simulation

The 3D geometry of the crimping setup includes the terminal, wire strands, crimping tool and anvil. The terminal and wire strands are discretized using three-dimensional 8-node solid C3D8RT elements. The number of elements per terminal thickness and per wire strand radius is typically set to four to ensure adequate resolution without excessive computational cost. The crimping tool and anvil, which do not deform significantly during the process, are modelled as rigid bodies using 4-node shell elements S4R. This assumption reduces computational time while still allowing for accurate computation of contact forces. Material properties are defined based on experimental data. A general contact algorithm is used to automatically manage interaction between all components during crimping.

During simulation, the anvil is fixed, while the crimping tool is moved towards the anvil. After the crimping, to release the pressure, the anvil and crimping tools are moved away from the terminal. The final step in the simulation is the determination of the wire pull-out force. The numerical model can be seen in Figure 62.

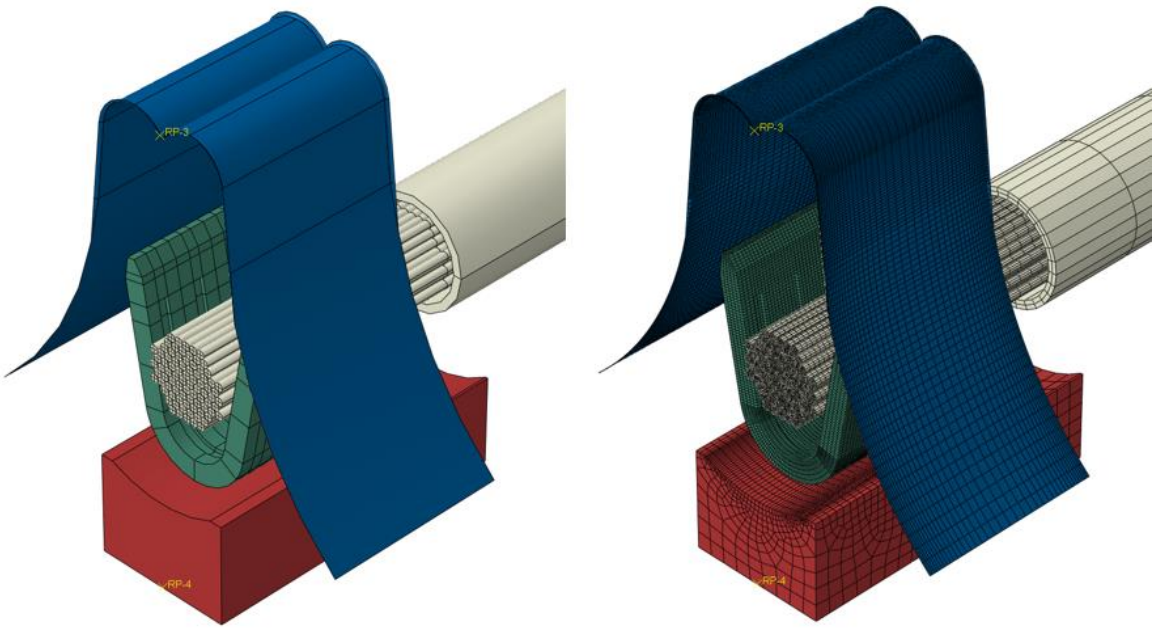

Figure 62. Numerical model of the wire crimping process in the finite element (FE) program Abaqus

6.2.3.1. Cohesion effect

During crimping simulation, after the terminal is plastically deformed by the crimping tools, there exist a measurable amount of elastic springback. It was noted that FEA simulation results do not represent correctly this state, as unrealistically, high springback occurs. This trend was also noticed by other authors, with the explanation that there is a cohesion between terminal wings that prevent crimp opening. To prove the theory, a small amount of lubricant was applied to the terminal, and the final results were similar to the numerical simulations without cohesion interaction [18]. Due to the high contact pressure and sliding of the terminal wings, tin (Sn) plating will diffuse into each other, and a new bond will be created. To model the cohesive behaviour of tin plating, it is necessary to define its stiffness and damage criterion in Abaqus CAE. These specific cohesive parameters can be calculated based on Sn tensile strength, elastic and shear modulus presented in Table 14.

Table 14. Mechanical properties of Sn

	Elastic modulus [GPa]	Shear Modulus [GPa]	Tensile strength [MPa]	Layer thickness [µmm]
Sn	41.6	15.6	220	10

The normal stiffness k_{nn} is calculated by given relation

$$k_{nn} = \frac{E}{t}, \tag{57}$$

where E is elastic modulus and t is layer thickness. For shear stiffness same approach is used

$$k_{ss} = k_{tt} = \frac{G}{t}, \tag{58}$$

where G is the shear modulus. Cohesive parameters are shown in table 15.

Table 15. Cohesive parameters for Sn plating

	Nominal stiffness [N/mm]	Shear stiffness [N/mm]	Nominal stress [MPa]	Shear stress [MPa]
Sn	4.16×10^6	1.56×10^6	220	150

For damage evolution, a linear softening law is applied, which describes how the material progressively loses its strength after damage initiation. The total displacement at failure is set

to 0.01 mm, at that point the cohesive connection will completely fail. This approach helps in capturing the terminal springback after crimping tools release the pressure on the terminal.

Chapter 7

Experimental and numerical results comparison

7.1. Deep drawing

Simulation of deep drawing process with a focus on the prediction of anisotropic material behaviour was conducted with Hill-1948, Yld2004-18P anisotropic yield criterion with associated flow rule integrated into Abaqus FEA package with solid C3D8R elements as shown in Figure 58. In addition to deep drawing simulation with associated flow rule, Hill1948 anisotropic yield criterion with non-associated flow rule (NAFR) within ADINA 8.6 FE program was made. The results of the NAFR-Hill models were obtained using an upgrade of the finite element analysis program ADINA 8.6, where the problem was considered as quasi-static. The above-mentioned upgrades represent an updated Lagrange formulation of a degenerate shell element with implemented constitutive formulations of Hill1948 model with non-associated yield flow rule and isotropic Voce hardening law [67]. In the description of the contact and friction conditions, the algorithm available in the program was used, which uses the constant function in addition to the classical Coulomb model and a constant coefficient of friction of 0.1. Experimental investigation on CuFe2P sheets has shown that *r*-values are not constant, they are affected by strain rate. To evaluate the difference and impact of different anisotropy parameters on deep drawing, numerical simulations have been made based on the data from Table 9. FEA results from both cases can be seen in Figure 63. According to the

results, there is a slight difference in stress level and consequently to plastic deformation. Numerical results with anisotropic parameters based on high strain rate have higher stresses, which is expected due to material higher yield stresses.

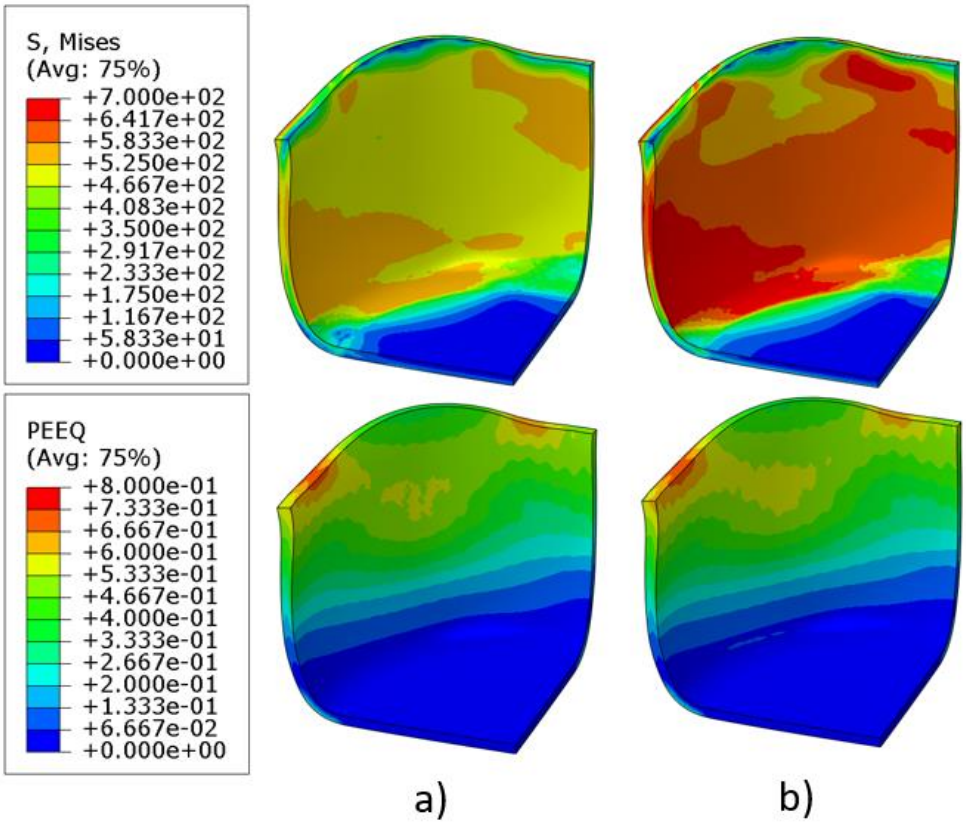

Figure 63. FEA results of deep drawing process with Abaqus Hill-1948 AFR model based on a) quasistatic and b) high strain rate material properties

Certain discrepancies between the numerical predictions and experimental results have been observed. Specifically, the predicted cup height, a critical dimension in the deep drawing process, deviates from the actual measurements. This divergence in results is due to the Hill1948 criterion's limitations in capturing the complex anisotropic behaviour of the material under multi-axial stress states. Cup height results are presented in Figure 64.

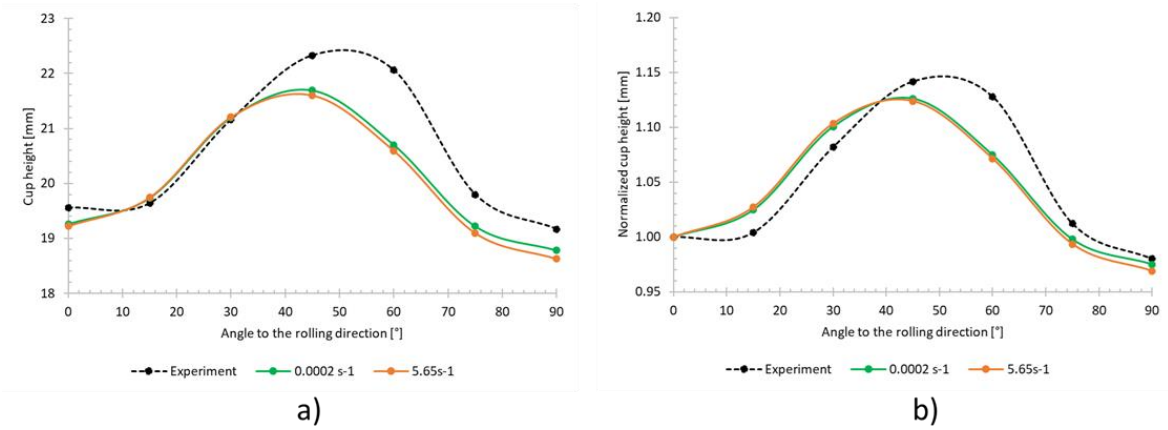

Figure 64. Prediction of a) real cup height and b) normalized cup height with Abaqus Hill-1948 AFR model with parameters calculated using Lankford coefficients corresponding to different strain rates

With further implementation of more advanced anisotropic models like Yld2004-18P and Hill1948 with non-associated flow rule, new results are obtained and presented in Figure 65. Results clearly show that Hill1948 with associated flow rule has results comparable to the much more complex model Yld2004-18P. Improved Hill1948 model with non-associated flow shows similar prediction like Hill1948 with associated flow.

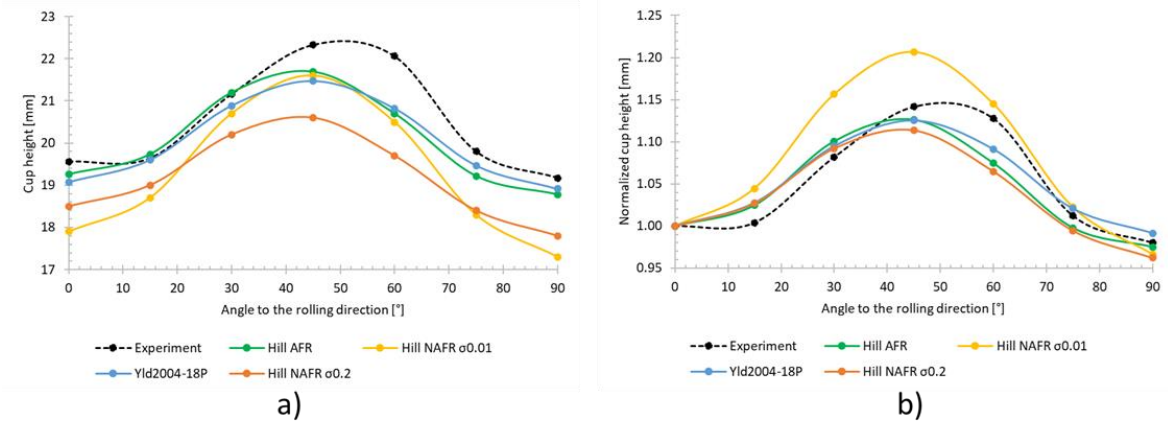

Figure 65. Prediction of a) real cup height and b) normalized cup height with different numerical models

Visual representation of cup height prediction is shown in Figure 66. where a CT scan of the real cup was compared to the result of numerical simulation based on the Hill1948 model with the associated flow rule.

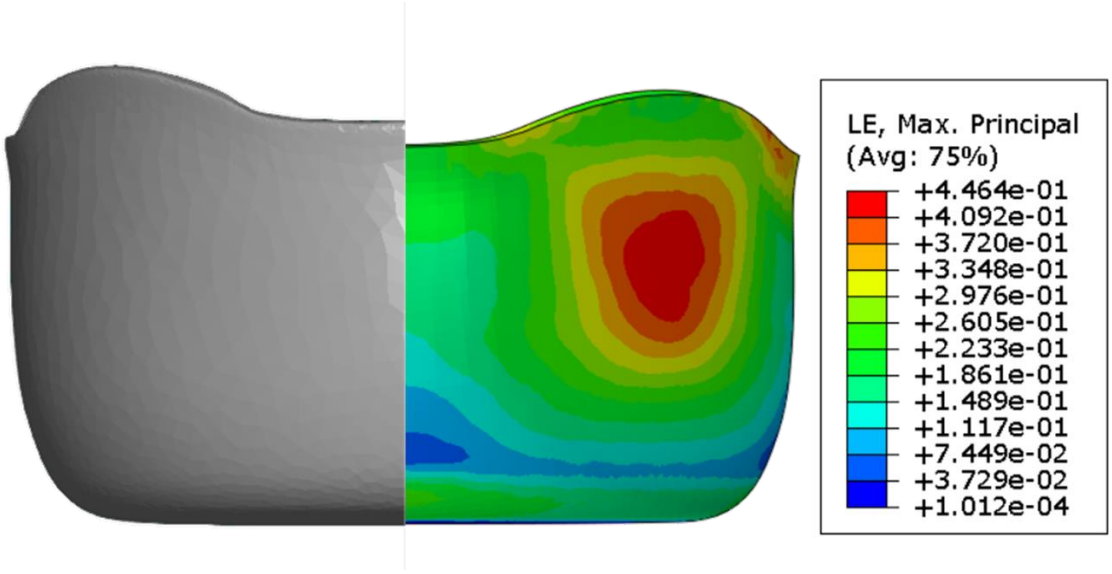

Figure 66. Cup height differences between CT scan of real sample and FEA model based on Hill1948 AFR

The forming force applied to the punch in the deep drawing process of a cup is influenced by several key factors, such as mechanical properties of the blank, friction, blank holder force, and punch speed. Blank holder force and punch speed can be taken directly from experimental setup, but friction must be assumed. As explained in experimental results section, blank was oiled and assumed coefficient of friction of 0.1 was set. Based on that, accuracy of numerical results of forming force will mostly depend on the defined interaction parameters and constitutive model. Comparison of numerical and experimental results of forming force is presented in Figure 67. Overall, there is a good match for both associate anisotropic models Hill48 and Yld2004-18P, where Hill48 is slightly more accurate in describing maximum force. Due to the explicit type of analysis, numerical curves have shown some fluctuations in force, which are minimal but also expected.

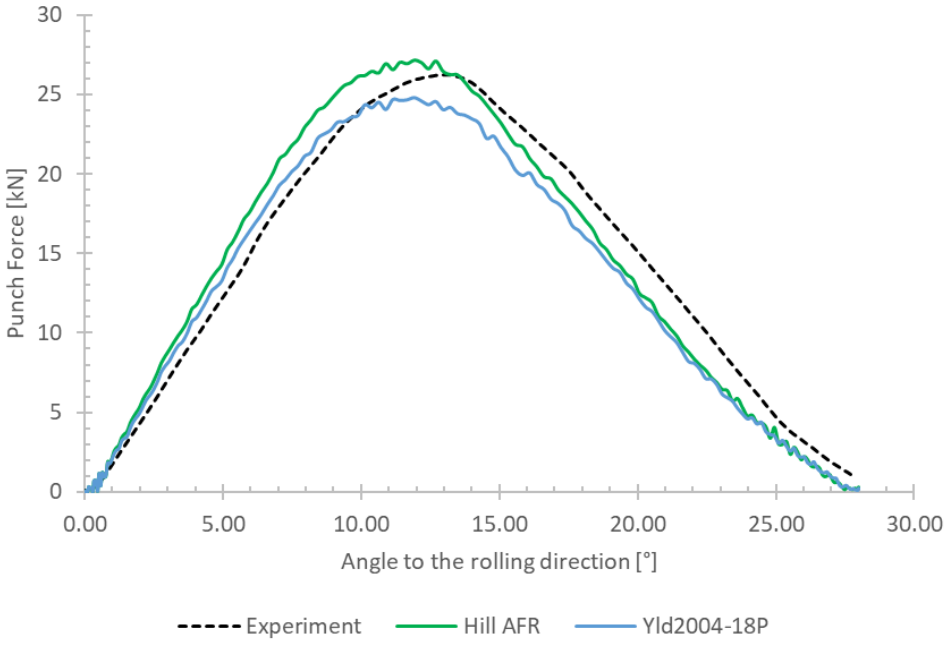

Figure 67. Force-stroke graph of forming force in the deep drawing process

Computation time for associated anisotropic models differs due to increased complexity of the Yld2004-18P model. Based on the presented deep drawing models, computation time for Hill1948 is 18 minutes, while for Yld2004-18P simulation time is doubled to 36 minutes. Simulations were performed on 30 cores on 2 processors Intel(R) Xeon(R) Gold 6444Y.

7.1.1. Analytical calculations of cup earing height in deep drawing process

Calculated *r*-values from uniaxial tensile tests can be correlated to the cup earing height in the deep drawing process. The directional dependence of the *r*-value can be graphically represented as a mirror image of the predicted height distribution of the cup. For example, if *r*-value is maximum for 30° samples and minimum for 90° samples, it is expected to have minimum height at 30° and maximum height at 90°. According to the work [143] a simplified equation for the analytical calculation of cup height reads

$$H_\theta = r_p + (R_b - R_c) + \frac{r_{\theta+90}}{(r_{\theta+90}+1)}\left[(R_c - R_b) + R_b \ln\left(\frac{R_b}{R_c}\right)\right]. \quad (59)$$

Where r_p is punch profile radius, R_b is a blank radius and R_c is tool opening radius, these values are calculated according to Figure 45 with the following equations

$$r_p = 3, \quad (60)$$

$$R_b = \frac{D_b}{2} = \frac{65}{2} = 32.5 \text{ and} \tag{61}$$

$$R_c = 0.25 \times (D_c + D_d) = 0.25 \times (35 + 39) = 18.5. \tag{62}$$

By substituting the values from equation (58), (59) and (60) into equation (57), it simplifies to

$$H_\theta = 17 + \frac{r_{\theta+90}}{(r_{\theta+90}+1)} \times 4.313\ . \tag{63}$$

Based on the values from Table 8, analytical cup height predictions are shown in Table 16.

Table 16. Cup height prediction with analytical calculation

Orientation	$0 \le \varepsilon_l^p \le 0.006$		$0 \le \varepsilon_l^p \le 0.013$	
	r	H [mm]	*r*	H [mm]
0°	0.64	19.59	0.74	19.48
15°	0.80	19.71	0.80	19.57
30°	1.08	19.91	1.20	20.02
45°	1.41	19.52	1.65	19.68
60°	2.07	19.23	2.34	19.35
75°	1.69	18.92	1.47	18.92
90°	1.51	18.68	1.37	18.84

The prediction of cup height using the analytical approach gives much lower values of the cup earing compared to the experimental results, as shown in Figure 68.

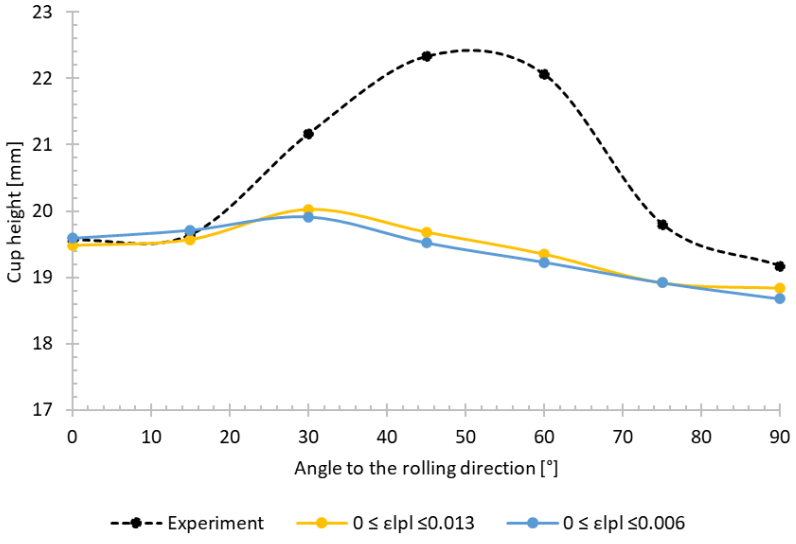

Figure 68. Comparison of analytical calculation of cup height and experimental results

7.2. Compression tests

The experimental and numerical investigation of the multi-layered material stack, subjected to compression by a 7 mm thick tool, provided insight into the deformation mechanics. Both material copper and copper alloy CuFe2P were compared. During the experimental investigation of CuFe2P it was noticed that higher strain was generated in an "X" form, accompanied by the temperature increase. With a more detailed investigation of images captured by the optical camera, it can be seen that failure of the plates occurred. In Figure 69 differences in numerical and experimental results can be seen.

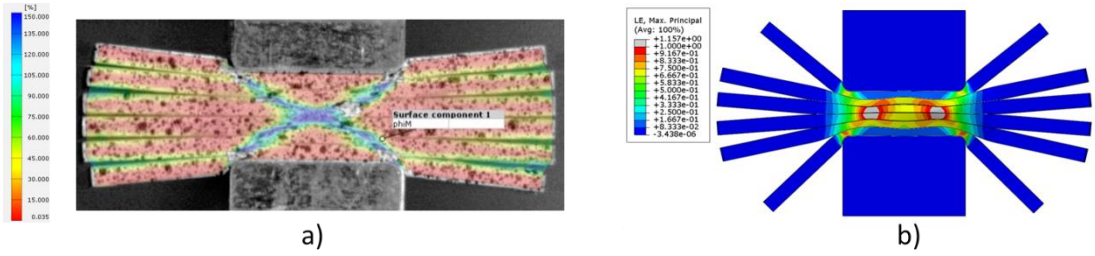

Figure 69. Compression test results for CuFe2P in a) experiment and b) numerical simulations

This trend is also followed by decrease in compression force, as the damage in material is increasing according to Figure 70. In this study, investigation of the material damage will not be considered as it is unwanted in metal forming and wire crimping process. There is a difference in force curve slope, which is due the stiffness.

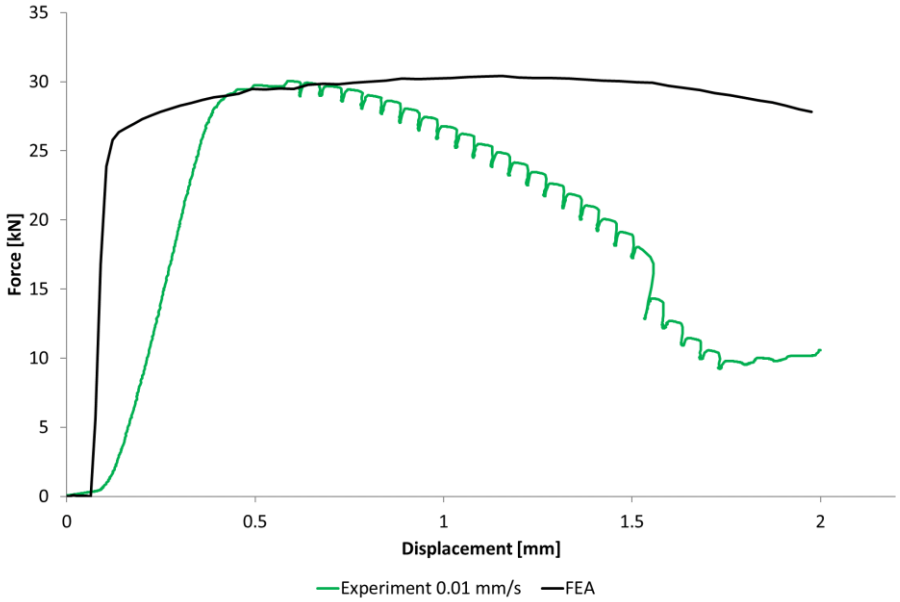

Figure 70. Experimental and numerical results of CuFe2P compression force

For pure copper, Cu-ETP, both force-displacement diagram and optical measurement showed no failure of the plates. Figure 71 represents final form of compressed plates and their relative displacements.

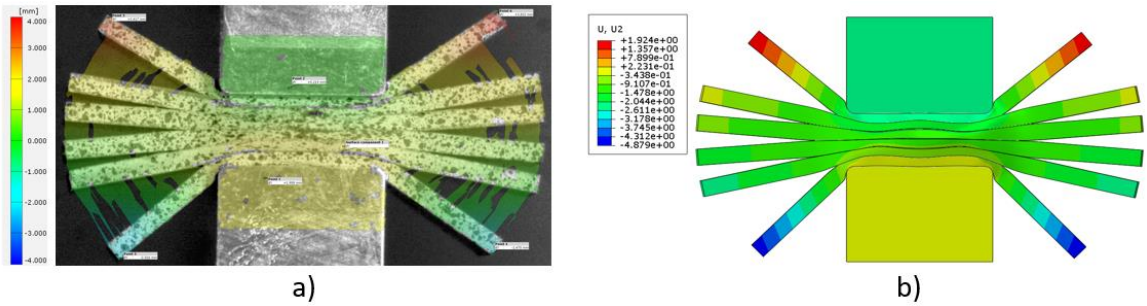

Figure 71. Relative displacement during compression of Cu-ETP plates at a) experimental and b) numerical results

The deformation plots revealed that the plates underwent both elastic and plastic deformation, with the middle plates experiencing a higher degree of plastic. The top and bottom plates, while also deforming, showed a reduced plastic region. Deformation differences can be seen in Figures 70.

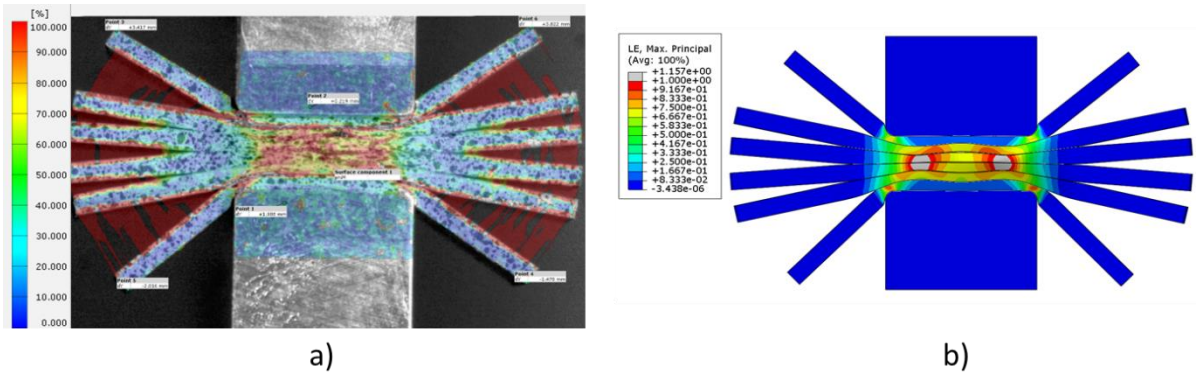

Figure 72. Deformation during compression at a) experiment and b) numerical results

Compression force-displacement graphs show a good match of numerical and experimental results in achieving the same level of force at a given displacement, as presented in Figure 73. The impact of experimental results when displacement is measured with DIC is compared to the tensile machine displacement values. The difference in the slope of the curve in the elastic region is due to the stiffness of the complete experimental setup, including the tensile test machine.

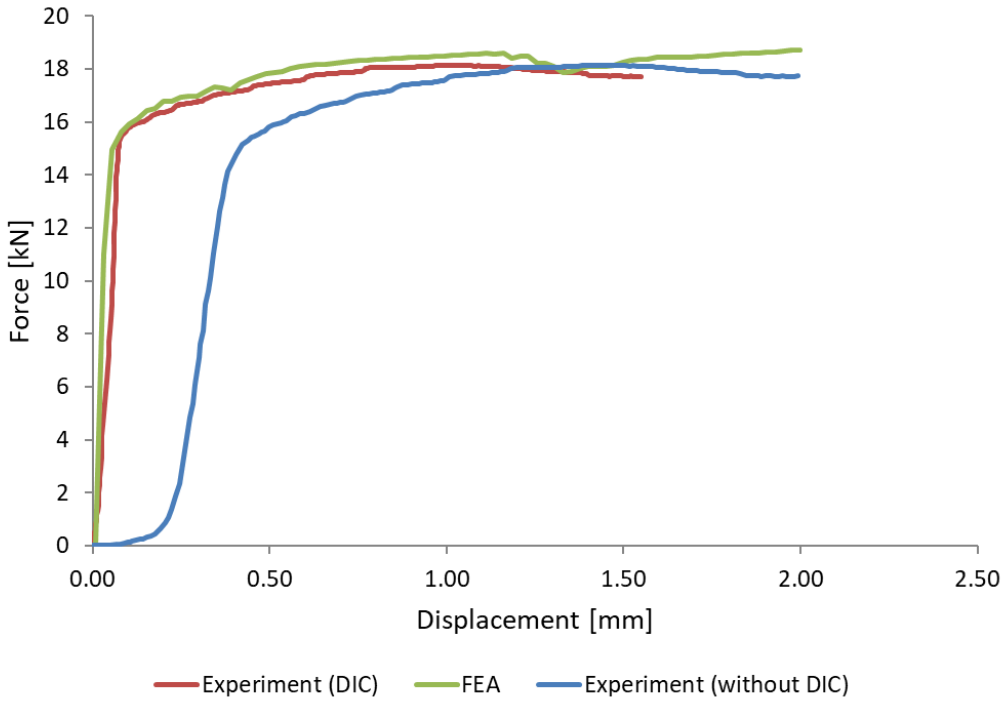

Figure 73. Experimental and numerical results of Cu-ETP compression force

During the compression test, it was observed that the final shape of the compressed plates was not as expected at a defined displacement of 2 mm for the tensile test machine. With DIC it was possible to measure real displacement and to compare movement of point A with FEA results. According to the results, the prediction of a numerical model is generally correct, with slight deviation after 0.5 mm displacement, results can be seen in Figure 74.

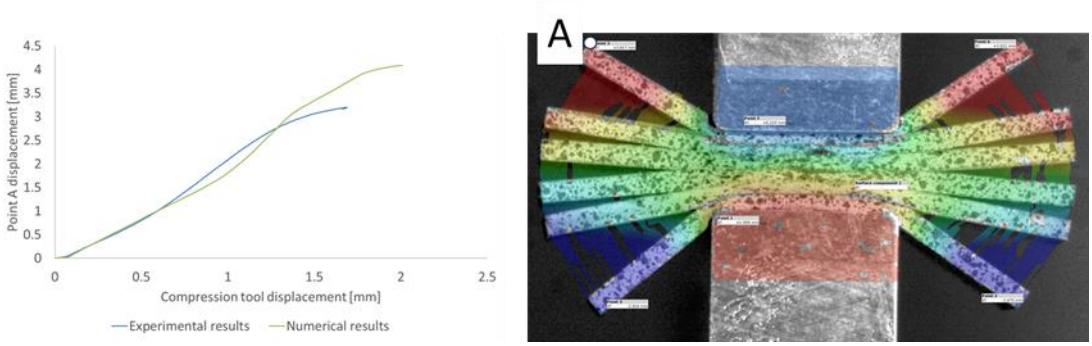

Figure 74. Displacement of point A for experimental and numerical results during compression test of Cu-ETP plates

Observation related to defined and real displacements should be considered in relation to Figure 70, as numerical results can be interpreted to deal with stiffer material. This is not correct, and experimental data should consider real displacements instead of defined ones.

7.3. Crimping simulations

Numerical results of the wire crimping process were made with an implemented constitutive model based on comprehensive experimental investigations using Abaqus software. Experimental research gave the opportunity to validate this complex numerical simulation at different strain rates. Visual inspection of crimp cross section is the initial and most common practice in the evaluation of the crimp shape design. Interaction between all components during the crimping simulation is complex, and determining the coefficient of friction is challenging. Several models with different coefficients of friction were made with the goal of finding the optimal COF by comparing crimp cross-sections from numerical simulations and experimental results. Figure 75 illustrates the equivalent stress distribution in the wire crimping process for various coefficients of friction, starting from 0.1 to 0.17, with a step of 0.01. Based on the numerical results, it can be seen that with lower COF terminal wings will penetrate deeper into wire strands, technically providing a better mechanical connection.

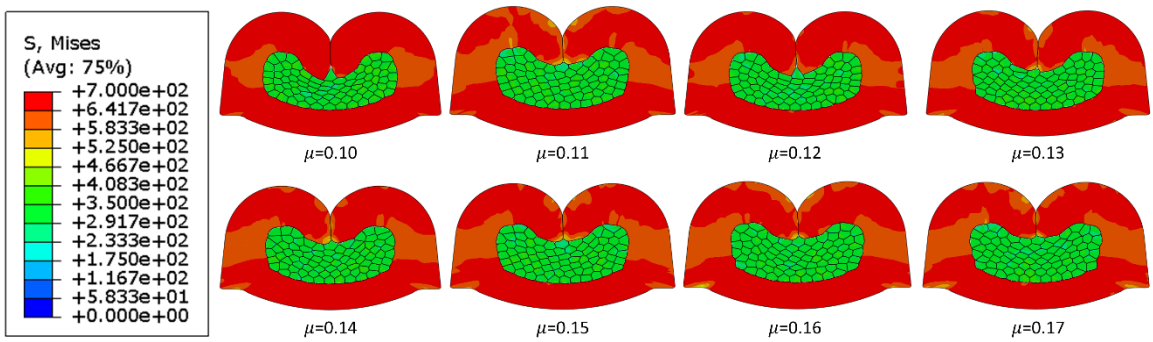

Figure 75. Influence of coefficient of friction on FEA results of crimp cross section for case of crimping velocity of 284 mm/s

For further evaluation of the impact of COF on FEA results, simulation values of crimping forces were compared to the experimental ones, as shown in Figure 76. It can be seen that with the variation of COF, the crimping force-displacement curve will change. Crimping force peak values will increase with the increase of the COF. The experimental crimping force curve is reaching marginally the same peak force values as the numerical simulation results.

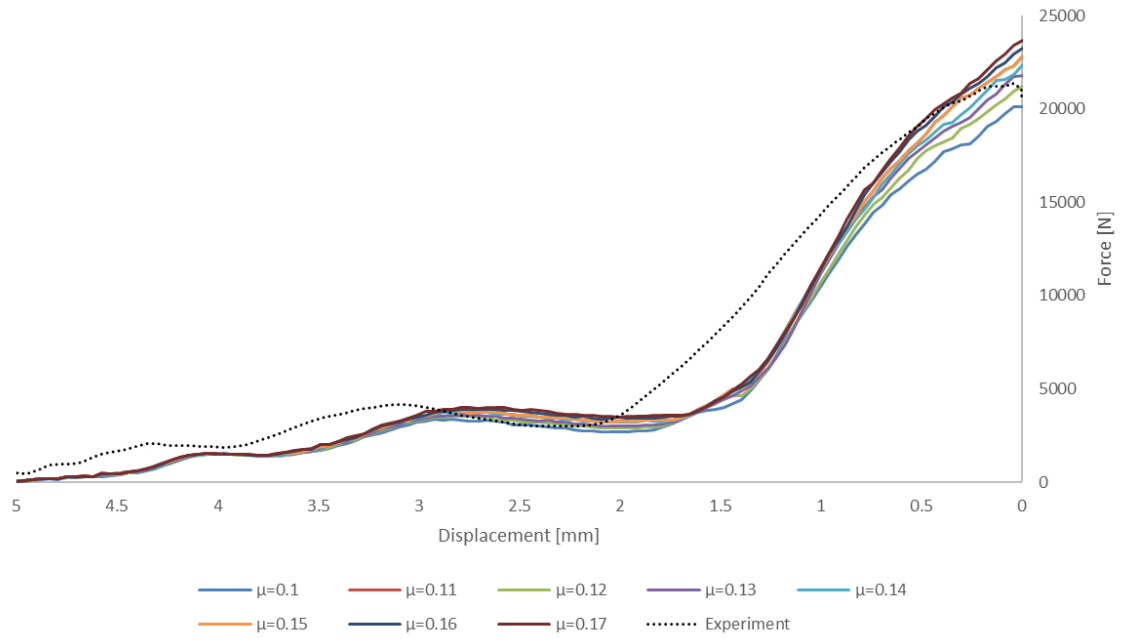

Figure 76. Impact of COF on crimping force-displacement curve

Although the peak values of the experiment correspond to the FEA results with COF of 0.12, there is a difference in force path. The biggest discrepancy is between displacements of 0.5 and 2 mm when the force-displacement curve slope is high. The reason for the difference is the stiffness of the tensile test machine (Instron 8801), crimping tools and also the crimping applicator. Based on the presented graph and known displacements, the stiffness of the complete setup can be calculated. When the stiffness of 50 kN/m is implemented in the calibration of displacement, experimental values would have a close match to numerical results with COF of 0.12 and 0.14 as shown in Figure 77.

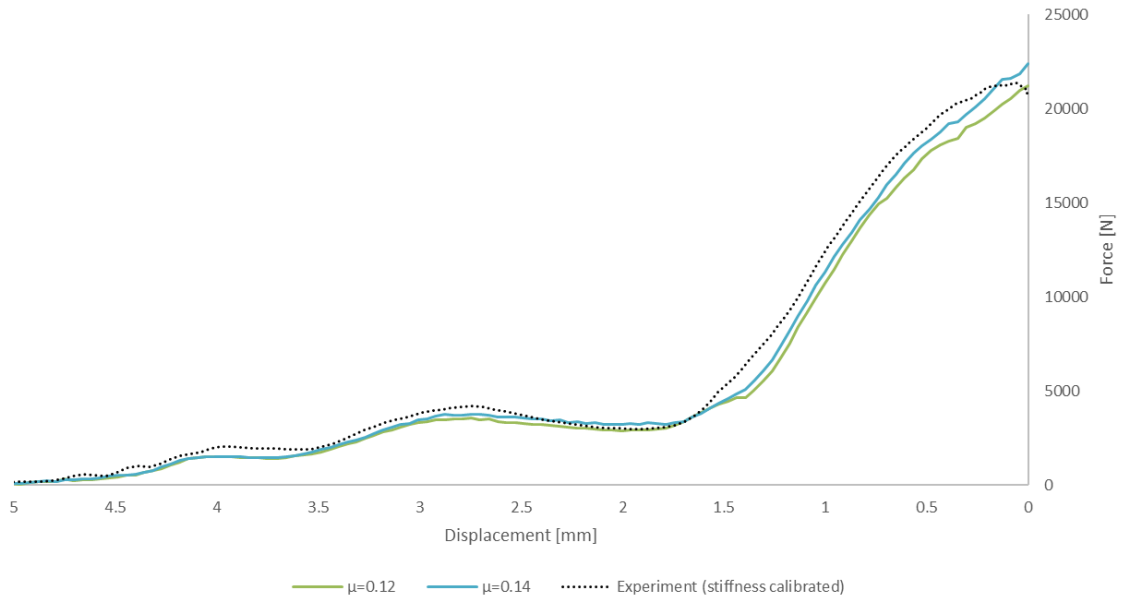

Figure 77. Wire crimping force comparison between FEA and experimental results with stiffness calibration

Based on the results, it can be concluded that 0.12 is the adequate COF for interaction between all components in the wire crimping process. Figure 78 compares a crimp cross-section of numerical simulation results with a COF of 0.12 with a cross-section made on the real sample with micro cuts and with a CT scan. The position of the micro-cut is extremely important, as the crimp cross-section may vary with the length of the crimp zone. When comparing experimental and numerical results, it can be seen that numerical predictions are in good match with the experimental crimp cross-section. This represents that the numerical model is a reliable tool for the prediction of material behaviour during the crimping process.

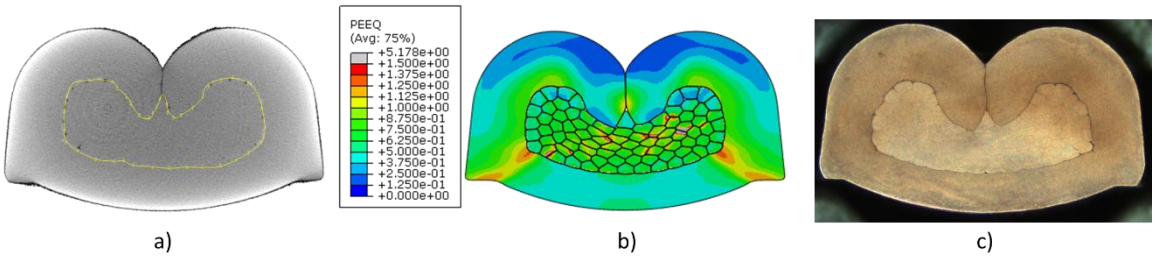

Figure 78. Comparison of crimp cross-section made by a) CT scan, b) numerical simulation and c) real sample micro-cut

7.3.1. Heat generation in crimping simulations

The heat generation during the wire crimping process is an outcome of the material being deformed plastically and frictional sliding. The top row of Figure 79 presents the FEA results,

illustrating the temperature distribution across the crimped wire and terminal, while the bottom represents experimental results. The colour gradients starting with red indicate a room temperature of 24 °C, while purple indicates the highest measured temperature. The experimental images reveal a similar pattern of heat concentration, validating the FEA model. The highest temperatures are observed at the same critical points, confirming that the FEA accurately predicts the thermal behaviour during crimping. However, slight discrepancies in temperature values between the FEA and experimental results can be attributed to heat exchange with crimping tools. In the experimental setup, the terminal is in contact with the anvil and during the crimping with the wire crimper, a heat exchange will occur. This can be seen in the latest step, when temperatures in FEA are going above the experimental results, as heat is not being transferred to the anvil and crimping tools. Wire strands were not painted with antiglare colour and known emissivity, so experimental values of wire strands' surface temperature may not be accurate. Overall, the comparison demonstrates that the FEA model is a reliable tool for predicting heat generation and distribution.

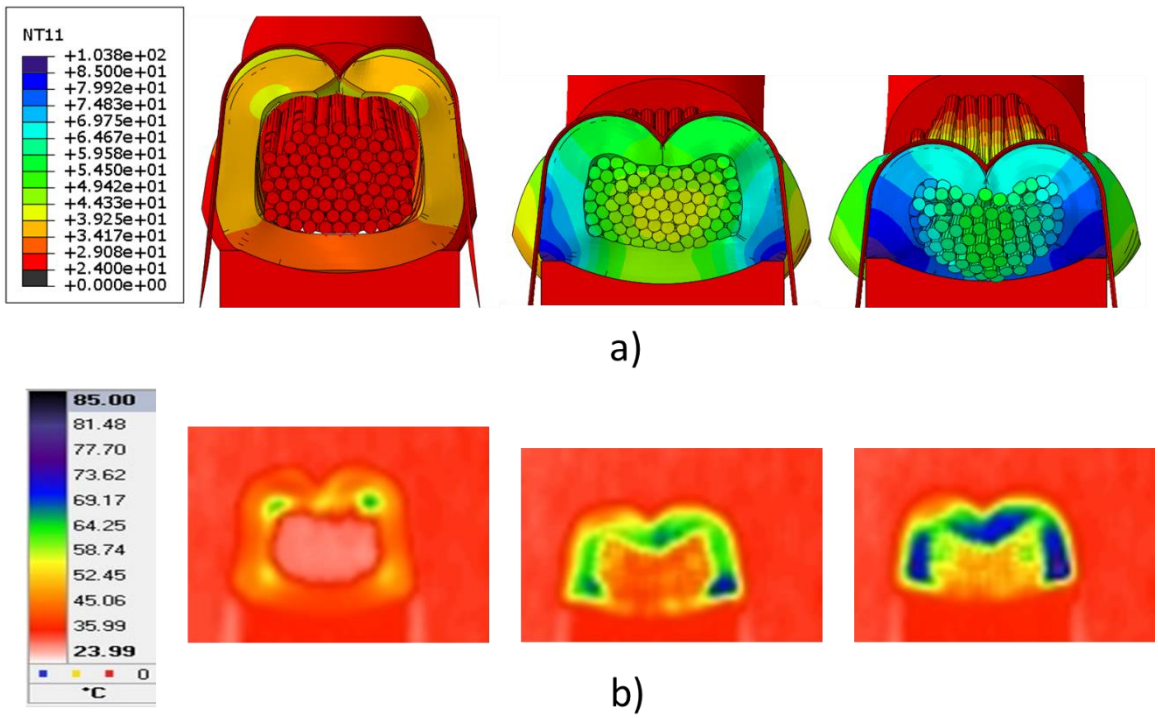

Figure 79. The temperature rise of the terminal during the crimping process performed a) numerically and b) experimentally

7.3.2. Terminal springback after crimping

The springback of the terminal, after the crimping process, is hard to model numerically due to the complex mechanical interactions. High material deformation and consequently, high contact pressure may create cohesion phenomena between terminal wings. The presence of cohesion phenomena between terminal wings will prevent the terminal opening and reduce the springback. Differences in wire crimping numerical results, with and without implemented cohesion, are shown in Figure 80. It can be seen that in cases when no cohesion is defined, terminal wings will separate after the crimping force is removed. Based on the results of the numerical model with cohesion defined no visible gap between terminal wings is detected.

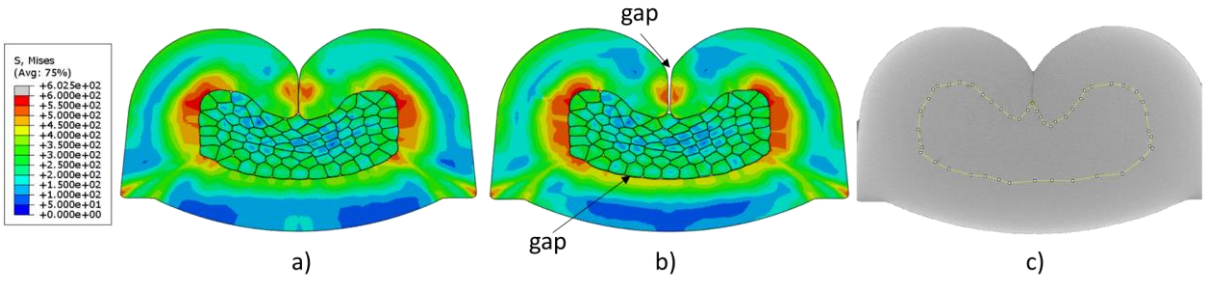

Figure 80. Crimp cross section from a) numerical model with cohesion b) numerical model without cohesion and c) experiment

To represent the level of springback at different crimping velocities, it was evaluated as a ratio of springbacked crimp height and initial crimp height, with and without adhesion. Higher ratios indicate a bigger springback and lack of crimp compaction after the crimping force is removed. By comparing these ratios, it is possible to visualize how different crimping speeds influence the springback behaviour, as shown in Figure 81. Results clearly show the terminal tendency to higher springback as the crimping speed increases, which is due to the fact that material yield stress increases with a strain rate increase.

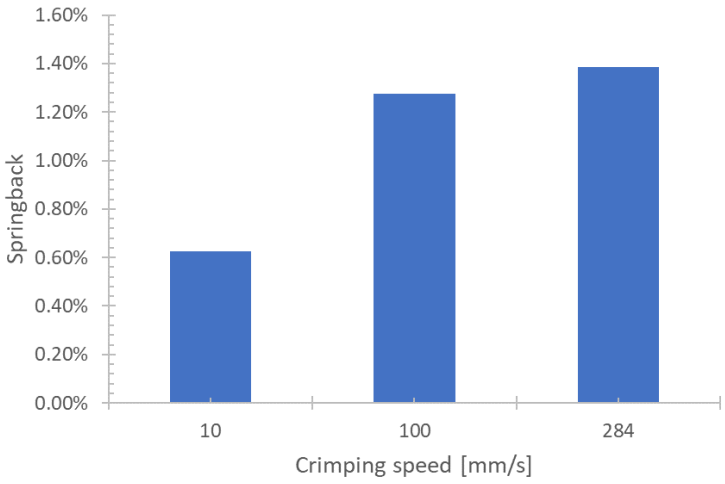

Figure 81. Influence of crimping speed on elastic springback of crimped terminal

Implementation of cohesion is not just crucial for the evaluation of spring back; it is also mandatory for further crimp investigations. By keeping the wire compact, strength of terminal crimp can be evaluated more accurately.

7.3.3. Wire pull-out force

For evaluation of the wire pullout force, a comparison between experimental and numerical results has been made. With numerical simulation, after the terminal is crimped and elastically springbacked to the final shape, the wire is pulled out to determine its maximum pullout force. Force displacement curves for experimental and numerical results, of terminal crimped with velocity of 100 mm/s, can be seen in Figure 82.

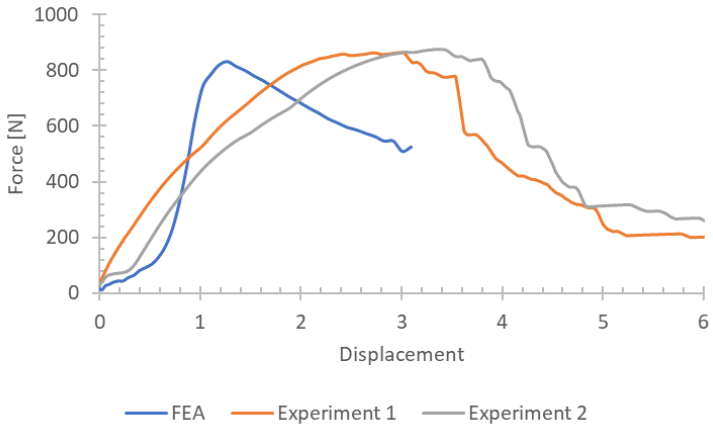

Figure 82. Numerical and experimental results of wire pull-out test for crimp sample crimped with a velocity of 100 mm/s

Maximum values of numerical and experimental results are almost the same, 864 N of pull out force on real sample and 832 N prediction of numerical simulations, which is a 3.7% difference. These small differences in results validate the accuracy of the numerical model in predicting the pullout force. When comparing the slope of both graphs, it can be seen that the slope of numerical results is greater than the experimental ones. The difference is expected and can be attributed to several factors. In the numerical simulation wire length was modeled to be as short as possible to reduce the number of elements and computational time. Conversely, in experiment setup wire should be long enough to provide a sufficient grip to prevent wire insulation slippage. Even with high tightening force, some slight slippage inside the jaws can be expected, which may be constant or for a small period of time. An additional factor is already presented and explained in Section 7.2 Compression tests, which demonstrates the impact of complete test setup stiffness.

During experimental investigation, it was found that there is a range of wire compression at which pull out force would have its maximum values. With the decrease in wire compression, there is a decrease in wire cross-section area, and wire snaps at a lower force. On the other side, with the increase of wire compression pull out force is lower as wire slips without breakage. Figure 83 shows the experimental and numerical evaluation of wire strands breaking or slipping during wire pullout.

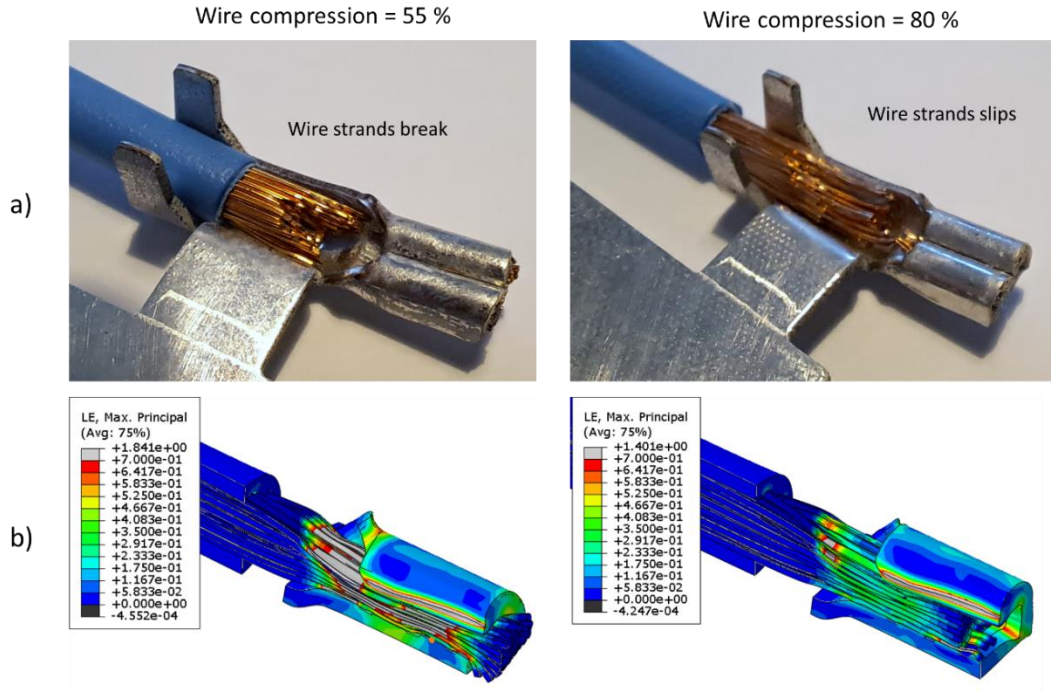

Figure 83. Wire pull-out a) experimental and b) numerical results at wire compression of 55% and 80%

For a better overview, the comparison of numerical and experimental results of wire pull-out force is shown in Figure 84. The graph indicates that both experimental and numerical results closely match, especially in the range of 55% to 75% wire compression. Beyond 75%, the pull-out force begins to decrease for both sets of results, highlighting the effect of wire strand slippage at higher compression levels. The close agreement of the experimental data (black dots) and FEA predictions (red dots) validates the accuracy of the numerical model in capturing the pull-out force behaviour across different compression percentages.

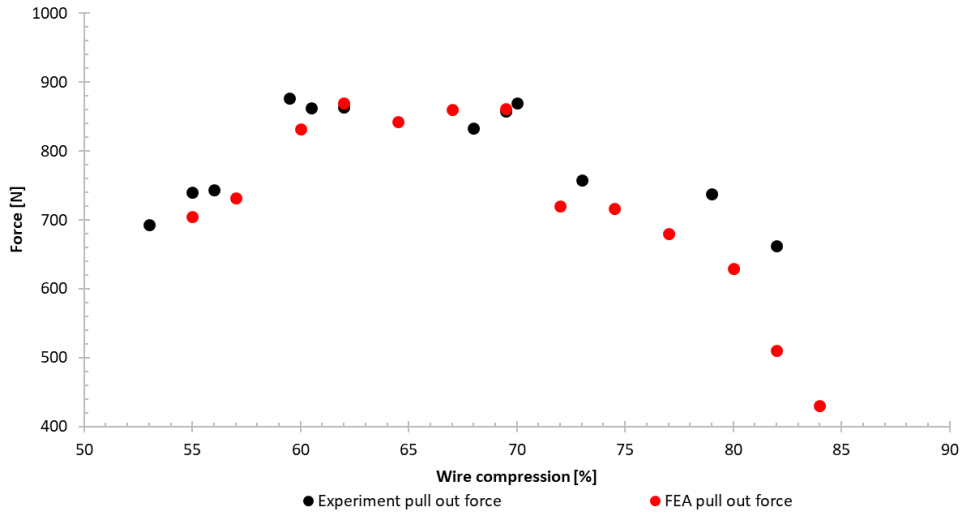

Figure 84. The comparison of experimental and numerical results of wire pull-out

7.3.4. Terminal crimp force monitoring

Terminal crimp force monitoring is demanded on production sites to reduce scrap rates. During the crimping process, force and displacement of the crimping tool are monitored, recorded and evaluated with the aim of detecting if current crimped samples are within tolerances. The same approach is used for the evaluation of the crimping process in numerical simulations. The force-displacement curves in Figure 85 represent two scenarios. The blue line represents the crimping force during the stroke of the crimp with all wire strands (full), while the green one represents the crimp with 9% missing strands. The graph is divided into different zones (Z1, Z2, Z3) which represent specific stages of the crimping process.

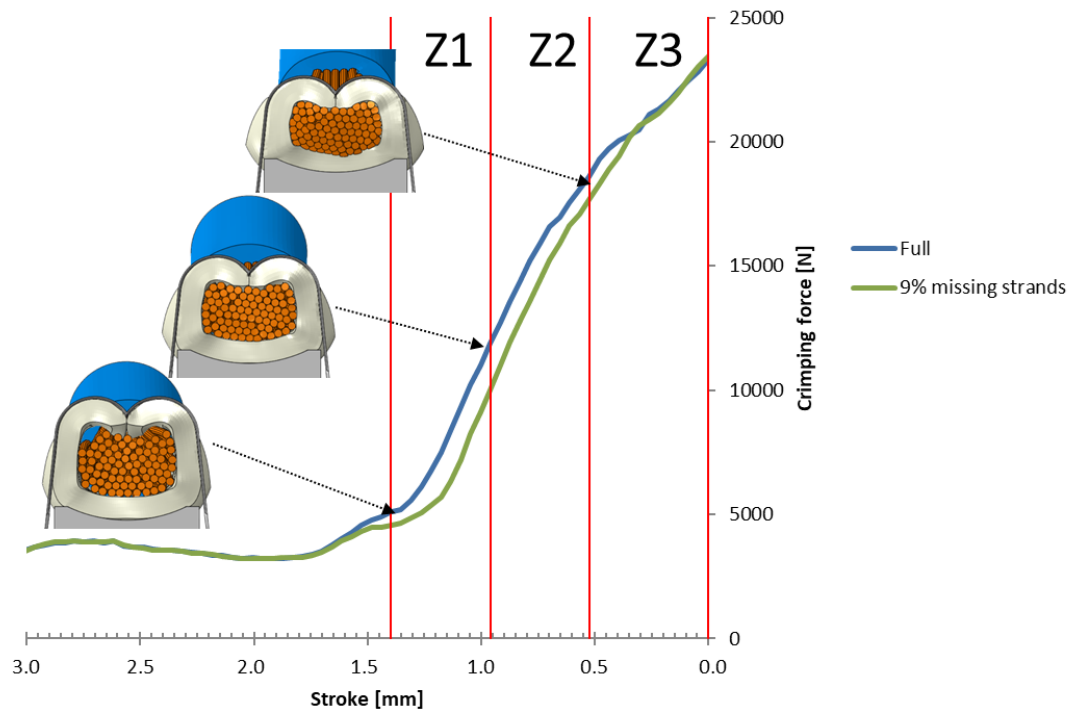

Figure 85. Crimp force monitoring during numerical simulation at crimping velocity of 100 mm/s

The initial phase (Z1) starts when terminal wings have bent and contact with wire strands is achieved, at that point differences between curves are being noticed. During next phase (Z2) slope of the curve starts to change, which represents wire strands are starting to deform plastically. In final phase (Z3) maximum force is achieved and terminal is plastically deformed.

The algorithm for the evaluation of crimping performance evaluates the area differences between the blue and green curves for each segment, and based on zone impact (weight factor), each sample is evaluated. The larger the area, the more point is gathered for each zone as results 1, 2 and 3 (RU1, RU2 and RU3) and summed to give the overall result (RUO). Limits for each zone are calculated based on the crimp force curve, while the overall limit (BLO) in area points is set to 50 by default. Table 17 shows crimp calculated values (RSx) in comparison to the limits. For presented wire compressions, 9% missing strand capabilities would be achieved, as there is at least one RUx value being above the defined limit BLx.

Table 17. Calculated parameter for crimp force monitoring based on crimping simulations

Wire compression [%]	RU1	RU2	RU3	RU0	BL1	BL2	BL3	BLO
60	27	24	13	65	24	24	28	50
67	25	32	22	78	24	24	26	50
72	26	39	28	91	25	25	24	50

Finding the optimal wire compression is done during product development on real samples by crimping the terminal to different values of wire compression and then performing mechanical and electrical tests. The approach with numerical simulation is based on a detailed analysis of wire pullout force and crimp force monitoring capabilities. Figure 86 shows the relationship of compression percentage and two key metrics: pullout force and crimp force monitoring results (RSO). During experimental investigations, it was found out that there is a range of wire compression in which retention forces are highest. In case the terminal is crimped to compression above approx. 70%, pull out force will start to reduce as wire strands will slip from the terminal connection. For the opposite case, when wire compression is below 60%, the force will also start to drop due to the big reduction in wire cross-section; wire snaps at lower forces. Numerical simulations have a great match with experimental results, with close exact values and also following the global trend. It was also found that with the increase of wire compression, crimp monitoring capabilities rise. Also in this case, numerical model is having a good match to the experimental results.

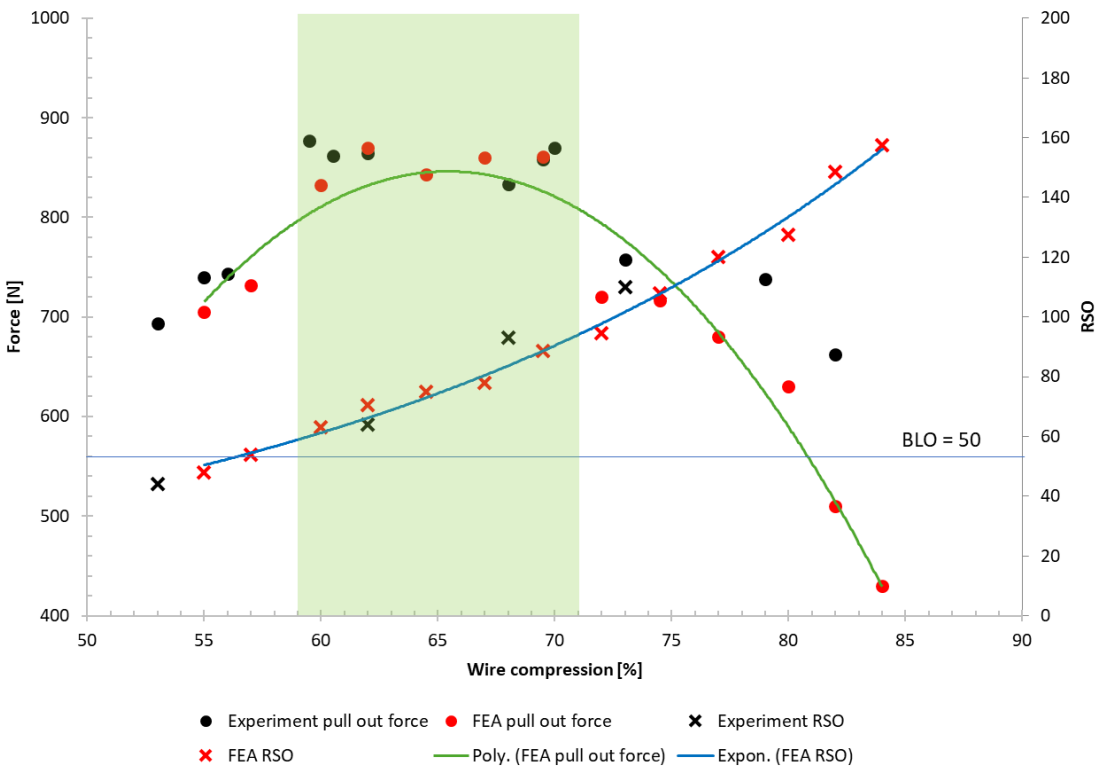

Figure 86. Relationship of wire compression percentage and crimp performance

Chapter 8

Conclusion

The wire crimping process is highly spread in the automotive industry, where it is used to bond electric terminals and wires. The aim of this study was to establish realistic numerical model for wire crimping simulation, which would be validated through extensive experimental investigation. The main focus was on understanding the mechanical and thermal behaviour of material during different stress states, with a final goal to have a terminal with predefined mechanical properties based on numerical simulations.

The manufacturing process of the copper alloy sheet CuFe2P involves rolling, which introduces anisotropy into its material properties. Consequently, uniaxial tensile mechanical properties vary depending on the loading direction relative to the rolling direction. This anisotropy arises from the alignment of the grain structure within the material's microstructure. The experimental results presented herein elucidate the elastoplastic behaviour of CuFe2P sheet, a material commonly employed in the production of electric terminals. The engineering stress-strain curves and *r*-value obtained from the experimental tests demonstrate that the CuFe2P sheet is a highly anisotropic material. The tensile strength, elongation and elastic modulus vary with the orientation of the tensile specimen relative to the rolling direction. Specimens aligned at 45° to the rolling direction exhibited the lowest elastic modulus and tensile strength, while those aligned at 0° showed the highest elongation. Specimens aligned at 90° demonstrated the highest tensile strength. It was found that the strain rate influences the strength and elongation of the CuFe2P sheet, while stiffness remains constant. As the strain rate increases, both the strength and elongation increase for all considered specimen orientations. This trend suggests

that the response of the CuFe2P alloy to strain rate is independent to the specimen orientation to the rolling direction.

The implementation of Digital Image Correlation (DIC) and infrared (IR) thermography techniques enabled the observation of local strain and temperature changes on the specimen surface during the loading process. The combination of these two non-contact methods facilitated the evaluation of thermoplastic material behaviour, providing valuable insights into the material's response during the metal forming process. This integrated approach enhances understanding of the material's behaviour, contributing to improved process optimization and product quality. The findings on the *r*-value and the inelastic heat fraction β present the complexity of the material's anisotropic behaviour. Experimental results demonstrate that *r*-values change with ongoing deformation process in tensile testing and are affected by strain rate, thus challenging the conventional assumption of it being constant. Similarly, both strain rate and tensile loading direction relative to rolling direction influenced the variations in the β coefficient. It indicates that the material's capacity to convert plastic work into heat is not a constant value.

Based on the experimental data, a new numerical model was established. The model takes into account the anisotropy in plastic material properties, thermoplasticity, strain rate effect and advanced contact interaction, like cohesion. The established numerical model was capable of more accurately predicting terminal behaviour during the crimping. The aim to determine the optimum compression of terminals with predefined mechanical properties of wires and terminal joints was achieved. The proposed numerical formulation allows the evaluation of the mechanical properties of the crimped terminal and enables the production of terminals with predefined mechanical properties.

Finally, the presented advanced numerical crimping simulations, validated by experimental data, accurately predicted the crimp cross-section and wire pull-out force at various wire compression ratios. Implementation of cohesive interaction is crucial for accurate evaluation of springback and wire pull-out force. The results demonstrated that higher crimping speeds lead to greater springback due to the increased material yield stress. By monitoring and evaluating the crimping force and displacement, it is possible to detect if crimped samples meet defined requirements. Implementing the same crimp monitoring algorithm into the numerical simulations enables the improvement of the crimping process with the aim of reducing the scrap ratio. The wire crimping simulations strongly correlated with experimental results,

effectively predicting optimal wire compression ranges. This validated numerical model provides a reliable tool for optimizing crimp design and ensuring production quality.

8.1. Scientific contribution

This study presents achievements in numerical modelling of the wire crimping process. Experimental investigations revealed that CuFe2P alloy is a highly anisotropic material and strain rate dependent. The tensile tests have shown that the Lankford coefficient changes with the increase of longitudinal deformation, challenging the conventional assumption of it being constant. Additionally, the inelastic heat fraction (IHF) varies with the strain rate and the orientation of the sample relative to the rolling direction, which indicates that the ability of the material to convert plastic work into heat is not a constant value. It was demonstrated how the strain rate and the sample orientation affect the fracture angle of the tensile specimens.

Based on the experimental results, numerical model is established in order to evaluate the strain rate effect on terminal and wire thermoplastic material behaviour in the case of large deformations. The established numerical model has increased accuracy in predicting crimped terminal shape, which results in terminals with predefined mechanical properties. Besides terminal wire pull-out force calculations, another meaningful contribution was monitoring crimp force numerically, which can determine and reduce the scrap ratio in production. The research results enable the production of terminals with predefined mechanical properties.

8.2. Further work

In further investigation it is planned to evaluate several different copper alloys which are commonly used for terminal production and make some general guidelines for terminal design. Additionally, a numerical simulation model of wire crimping would be extended to capture contact pressure and contact area between wire strands and terminal during defined dynamic loading, with the final aim to make a correlation with electrical resistance.

ŽIVOTOPIS

Ante Bubalo rođen je u Zagrebu, 31. prosinca 1988. godine. Osnovnu školu Mladost pohađao je u Zagrebu, a 2003. godine upisuje VII. Gimnaziju u Zagrebu. Godine 2007. upisuje Fakultet strojarstva i brodogradnje, gdje se opredjeljuje za konstrukcijski smjer. Tijekom studija držao je demonstrature iz Mehanike I, II i Nauke o čvrstoći. Sudjelovao je u radu Udruge mehatroničara te vodio projekt „Elektroničko upravljanje radom Otto motora“. Titulu magistra strojarstva stječe 2013. godine, te se zapošljava u tvrtki Yazaki Europe Limited u odjelu računalnih simulacija. Godinu dana nakon završetka diplomskog studija upisuje doktorski studij pod mentorstvom prof. dr. sc. Zdenka Tonkovića. U svom profesionalnom radu bavi se numeričkim analizama i patentnim pravom. Kao patentni specijalist i stručna pomoć sudjelovao je dva puta u patentnim sporovima pri Europskim patentnim uredima u Haagu i Münchenu. Koautor je dva članka objavljenih u međunarodnim časopisima, te je sudjelovao na četiri konferencije. Član je Hrvatskoga društva za mehaniku (HDM). Oženjen je i otac dvije kćeri.

CURRICULUM VITAE

Ante Bubalo was born in Zagreb on December 31, 1988. He attended Elementary School Mladost in Zagreb, and in 2003 he enrolled in VII. Gymnasium in Zagreb. In 2007, he enrolled on the Faculty of Mechanical Engineering and Naval Architecture, where he decided to specialize in engineering design. During his studies, he was a student assistant in Mechanics I, II and Strength of materials. He participated in the work of the Mechatronics Association and was leading the project "Electronic Control of Otto engine". He obtained his master's degree in mechanical engineering in 2013 and was employed by Yazaki Europe Limited in the numerical simulation department. A year after completing his graduate studies, he enrolled in doctoral studies under the mentorship of Prof. Zdenko Tonković PhD. In his professional work, he deals with numerical analyses and patent law. As a patent specialist and expert in the field, he participated twice in patent disputes at the European Patent Offices in The Hague and Munich. He is the co-author of two articles published in international journals and has participated in four conferences. He is a member of the Croatian Society of Mechanics (HDM). He is married and the father of two daughters.

REFERENCES

[1] Bubalo A, Tonković Z, Zorica D. Numerical and Experimental Investigations of Wire Crimping Process. 8th Int. Congr. Croat. Soc. Mech., Opatija: 2015.

[2] Petitprez M, Mocellin K. Non standard samples behaviour law parameters determination by inverse analysis. Comput Methods Mater Sci 2013;13:56−62.

[3] Roccato PE, Bellavia L, Galliana F, Capra PP, Perta A. Dependency of the electrical resistance in crimped connections on mechanical stresses. Eng Res Express 2020;2:035002. https://doi.org/10.1088/2631-8695/aba1a2.

[4] Li P, Liu G, Fan J, Sun J, Xiu H, Tian C. Mathematical model for the tensile strength of the crimping assembly of aviation wiring harness end. Sci Rep 2021;11:17868. https://doi.org/10.1038/s41598-021-97498-8.

[5] Galliana F, Bellavia L, Caria SE, Perta AP, Roccato PE. The Effect of Thermal Stresses on the Electrical Resistance of Crimped Connections. MAPAN 2023;38:71−82. https://doi.org/10.1007/s12647-022-00574-1.

[6] Kuckuck C, Lodige P, Blauth M, Yuan H, Song J. Analysis of the Interstrand and Strand/Connector Resistance Relations in Wire Connection Systems. IEEE Trans Compon Packag Manuf Technol 2020;10:1328−36. https://doi.org/10.1109/TCPMT.2020.3005075.

[7] Mohd RMM, Huzainie SAH, Ahmad BAG. Study of cable crimping factors affecting contact resistance of medium voltage cable ferrule and lug. 22nd Int. Conf. Exhib. Electr. Distrib. CIRED 2013, Stockholm, Sweden: Institution of Engineering and Technology; 2013, p. 1017−1017. https://doi.org/10.1049/cp.2013.1038.

[8] Castro TAM, Silva FJG, Campilho RDSG. Optimising a Specific Tool for Electrical Terminals Crimping Process. Procedia Manuf 2017;11:1438−47. https://doi.org/10.1016/j.promfg.2017.07.274.

[9] Villeneuve G, Kulkarni D, Bastnagel P, Berry D. Dynamic finite element analysis simulation of the terminal crimping process. Electr. Contacts - 1996 Proc. Forty-Second IEEE Holm Conf. Electr. Contacts Jt. 18th Int. Conf. Electr. Contacts, Chicago, IL, USA: IEEE; 1996, p. 156−72. https://doi.org/10.1109/HOLM.1996.557193.

[10] Chen Y, Zhang M, Cao R, Xiang Y, Zhang B, Liu G. Reliability study on crimping joint of copper-clad aluminum wire cable in spacecraft. 2020 21st Int. Conf. Electron. Packag. Technol. ICEPT, Guangzhou, China: IEEE; 2020, p. 1–5. https://doi.org/10.1109/ICEPT50128.2020.9202546.

[11] Williams DM, Range ME, Pascucci VC, Savrock JT. Forensic analysis of thermally stressed crimp connections. 2015 IEEE 61st Holm Conf. Electr. Contacts Holm, San Diego, CA, USA: IEEE; 2015, p. 331–7. https://doi.org/10.1109/HOLM.2015.7355117.

[12] Fleischmann H, Spreng S, Kohl J, Kisskalt D, Franke J. Distributed condition monitoring systems in electric drives manufacturing. 2016 6th Int. Electr. Drives Prod. Conf. EDPC, Nuremberg, Germany: IEEE; 2016, p. 52–7. https://doi.org/10.1109/EDPC.2016.7851314.

[13] Ogihara S, Takata K, Hattori Y, Yoshida K. Mechanical Analysis of the Crimping Connection. Electr. Contacts - 2006 Proc. 52nd IEEE Holm Conf. Electr. Contacts, Montreal, QC, Canada: IEEE; 2006, p. 89–94. https://doi.org/10.1109/HOLM.2006.284070.

[14] Kuhn M, Nguyen HG. The future of harness development and manufacturing - Results from an expert case study, Ludwigsburg, Germany: 2019.

[15] Kugener S. Simulation of the Crimping Process by Implicit and Explicit Finite Element Methods 1995;4.

[16] Kakuta N. Crimp Analysis Simulation Technology. SAE Int J Passeng Cars - Electron Electr Syst 2008;1:501–7. https://doi.org/10.4271/2008-01-1271.

[17] Mroczkowski RS, Geckle RJ. Concerning "cold welding" in crimped connections. Electr. Contacts - 1995 Proc. Forty-First IEEE Holm Conf. Electr. Contacts, Montreal, Que., Canada: IEEE; 1995, p. 154–64. https://doi.org/10.1109/HOLM.1995.482867.

[18] Zhmurkin DV, Corman NE, Copper CD, Hilty RD. 3-Dimensional Numerical Simulation of Open-Barrel Crimping Process. 2008 Proc. 54th IEEE Holm Conf. Electr. Contacts, Orlando, Florida: IEEE; 2008, p. 178–84. https://doi.org/10.1109/HOLM.2008.ECP.41.

[19] Mocellin K, Petitprez M. Experimental and Numerical Analysis of Electrical Contact Crimping to Predict Mechanical Strength. Procedia Eng 2014;81:2018−23. https://doi.org/10.1016/j.proeng.2014.10.274.

[20] Mocellin K, Petitprez M, Bouchard P-O, Desjean C. Computational Modeling of Electrical Contact Crimping and Mechanical Strength Analysis. 2010 Proc. 56th IEEE Holm Conf. Electr. Contacts, Charleston, SC, USA: IEEE; 2010, p. 1−3. https://doi.org/10.1109/HOLM.2010.5619564.

[21] Bubalo A, Tonković Z, Zorica D. Development of quick and reliable method for electric terminal crimp design. 10th Int. Congr. Croat. Soc. Mech., Pula: 2022.

[22] Li P, Liu G, Wang P, Huang G, Yu Z, Xiu H, et al. Numerical and experimental study on the relationship between pull-out force and indentation depth of aviation wire crimp terminal. Sci Rep 2022;12:21939. https://doi.org/10.1038/s41598-022-26563-7.

[23] Zhmurkin DV. 3-D Simulation of Open-Barrel Crimping Process: Study of the Effect of Serrations. 2009 Proc. 55th IEEE Holm Conf. Electr. Contacts, Vancouver, British Columbia, Canada: IEEE; 2009, p. 114−20. https://doi.org/10.1109/HOLM.2009.5284414.

[24] Roccato PE, Bellavia L, Capra PP, Cinnirella L, Galliana F, Perta A. Influence of crimped connections in temperature rise tests. Meas Sci Technol 2020;31:044008. https://doi.org/10.1088/1361-6501/ab5824.

[25] Kumar RK, Babu AS. Finite element analysis and experimental study on metal joining by mechanical crimping. Int J Serv Comput Oriented Manuf 2014;1:295. https://doi.org/10.1504/IJSCOM.2014.066489.

[26] Dubar L, Pruncu CI, Dubois A, Dubar M. Effects of Contact Pressure, Plastic Strain and Sliding Velocity on Sticking in Cold Forging of Aluminium Billet. Procedia Eng 2014;81:1842−7. https://doi.org/10.1016/j.proeng.2014.10.243.

[27] Chenot J-L, Béraudo C, Bernacki M, Fourment L. Finite Element Simulation of Multi Material Metal Forming. Procedia Eng 2014;81:2427−32. https://doi.org/10.1016/j.proeng.2014.10.345.

[28] Kim SB, Huh H, Bok HH, Moon MB. Forming limit diagram of auto-body steel sheets for high-speed sheet metal forming. J Mater Process Technol 2011;211:851−62. https://doi.org/10.1016/j.jmatprotec.2010.01.006.

[29] Muller M, Barrans SM, Blunt L. Predicting plastic deformation and work hardening during V-band formation. J Mater Process Technol 2011;211:627−36. https://doi.org/10.1016/j.jmatprotec.2010.11.020.

[30] Reedy ED. Adhesion/atomistic friction surface interaction model with application to interfacial fracture and nanofabrication. Int J Solids Struct 2013;50:937−43. https://doi.org/10.1016/j.ijsolstr.2012.11.025.

[31] Shisode M, Hazrati J, Mishra T, De Rooij M, Horn CT, Van Beeck J, et al. Modeling boundary friction of coated sheets in sheet metal forming. Tribol Int 2021;153:106554. https://doi.org/10.1016/j.triboint.2020.106554.

[32] Kamiya S, Furuta H, Omiya M, Shimomura H. A novel evaluation method for interfacial adhesion strength in ductile dissimilar materials. Eng Fract Mech 2008;75:5007−17. https://doi.org/10.1016/j.engfracmech.2008.06.011.

[33] Hol J, Cid Alfaro MV, De Rooij MB, Meinders T. Advanced friction modeling for sheet metal forming. Wear 2012;286−287:66−78. https://doi.org/10.1016/j.wear.2011.04.004.

[34] Karupannasamy DK, De Rooij MB, Schipper DJ. Multi-scale friction modelling for rough contacts under sliding conditions. Wear 2013;308:222−31. https://doi.org/10.1016/j.wear.2013.09.012.

[35] Hachani M, Fourment L. A smoothing procedure based on quasi-C1 interpolation for 3D contact mechanics with applications to metal forming. Comput Struct 2013;128:1−13. https://doi.org/10.1016/j.compstruc.2013.05.008.

[36] Taureza M, Song X, Castagne S. On the influence of workpiece material on friction in microforming and lubricant effectiveness. J Mater Process Technol 2014;214:998−1007. https://doi.org/10.1016/j.jmatprotec.2013.11.003.

[37] Suzuki T, Wang Z, Yoshikawa Y. Effect of Plastic Deformation of Bulk Material on Frictional Behavior in Dry Metal Forming. Procedia Eng 2014;81:1872−7. https://doi.org/10.1016/j.proeng.2014.10.249.

[38] Venema J, Hazrati J, Atzema E, Matthews D, Van Den Boogaard T. Multiscale friction model for hot sheet metal forming. Friction 2022;10:316−34. https://doi.org/10.1007/s40544-021-0504-6.

[39] Safara Nosar N, Olsson M. Influence of tool steel surface topography on adhesion and material transfer in stainless steel/tool steel sliding contact. Wear 2013;303:30−9. https://doi.org/10.1016/j.wear.2013.02.015.

[40] Karupannasamy DK, Hol J, De Rooij MB, Meinders T, Schipper DJ. A friction model for loading and reloading effects in deep drawing processes. Wear 2014;318:27−39. https://doi.org/10.1016/j.wear.2014.06.011.

[41] Peng L, Lai X, Lee H-J, Song J-H, Ni J. Friction behavior modeling and analysis in micro/meso scale metal forming process. Mater Des 2010;31:1953−61. https://doi.org/10.1016/j.matdes.2009.10.040.

[42] Yang X, Zhang L, Politis DJ, Zhang J, Gharbi MM, Leyvraz D, et al. Experimental and modelling studies of the transient tribological behaviour of a two-phase lubricant under complex loading conditions. Friction 2022;10:911−26. https://doi.org/10.1007/s40544-021-0542-0.

[43] Doca T, Andrade Pires FM, Cesar De Sa JMA. A frictional mortar contact approach for the analysis of large inelastic deformation problems. Int J Solids Struct 2014;51:1697−715. https://doi.org/10.1016/j.ijsolstr.2014.01.013.

[44] Lee K, Moon C, Lee M-G. A Review on Friction and Lubrication in Automotive Metal Forming: Experiment and Modeling. Int J Automot Technol 2021;22:1743−61. https://doi.org/10.1007/s12239-021-0150-z.

[45] Figueiredo L, Ramalho A, Oliveira MC, Menezes LF. Experimental study of friction in sheet metal forming. Wear 2011;271:1651−7. https://doi.org/10.1016/j.wear.2011.02.020.

[46] Seitz A, Popp A, Wall WA. A semi-smooth Newton method for orthotropic plasticity and frictional contact at finite strains. Comput Methods Appl Mech Eng 2015;285:228−54. https://doi.org/10.1016/j.cma.2014.11.003.

[47] Martinet F, Chabrand P. Application of ALE ®nite elements method to a lubricated friction model in sheet metal forming. Int J Solids Struct 2000.

[48] Neto DM, Oliveira MC, Menezes LF, Alves JL. Applying Nagata patches to smooth discretized surfaces used in 3D frictional contact problems. Comput Methods Appl Mech Eng 2014;271:296−320. https://doi.org/10.1016/j.cma.2013.12.008.

[49] Makino T, Michimoto T, Moriyama S, Kikuchi T. Contact Potential Difference Measurement of Adhesion Process during Micro/Meso-scale Injection Upsetting. Procedia Eng 2014;81:444−9. https://doi.org/10.1016/j.proeng.2014.10.020.

[50] Kirkhorn L, Frogner K, Andersson M, Ståhl JE. Improved Tribotesting for Sheet Metal Forming. Procedia CIRP 2012;3:507−12. https://doi.org/10.1016/j.procir.2012.07.087.

[51] Wu F, Hong Y, Zhang Z, Huang C, Huang Z. Effect of Lankford Coefficients on Springback Behavior during Deep Drawing of Stainless Steel Cylinders. Materials 2023;16:4321. https://doi.org/10.3390/ma16124321.

[52] Davoodi B, Zareh-Desari B. Assessment of forming parameters influencing spring-back in multi-point forming process: A comprehensive experimental and numerical study. Mater Des 2014;59:103−14. https://doi.org/10.1016/j.matdes.2014.02.043.

[53] Baseri H, Bakhshi-Jooybari M, Rahmani B. Modeling of spring-back in V-die bending process by using fuzzy learning back-propagation algorithm. Expert Syst Appl 2011;38:8894−900. https://doi.org/10.1016/j.eswa.2011.01.102.

[54] Sulaiman S, Ariffin MKAM, Lai SY. Springback Behaviour in Sheet Metal Forming for Automotive Door. AASRI Procedia 2012;3:224−9. https://doi.org/10.1016/j.aasri.2012.11.037.

[55] Narasimhan N, Lovell M. Predicting springback in sheet metal forming: an explicit to implicit sequential solution procedure. Finite Elem Anal Des 1999;33:29−42. https://doi.org/10.1016/S0168-874X(99)00009-8.

[56] Dilip Kumar K, Appukuttan KK, Neelakantha VL, Naik PS. Experimental determination of spring back and thinning effect of aluminum sheet metal during L-bending operation. Mater Des 1980-2015 2014;56:613−9. https://doi.org/10.1016/j.matdes.2013.11.047.

[57] Liao J, Xue X, Barlat F, Gracio J. Material Modelling and Springback Analysis for Multi-stage Rotary Draw Bending of Thin-walled Tube Using Homogeneous Anisotropic Hardening Model. Procedia Eng 2014;81:1228−33. https://doi.org/10.1016/j.proeng.2014.10.102.

[58] Hashemi SJ, Roohi AH. Minimizing spring-back and thinning in deep drawing process of St14 steel sheets. Int J Interact Des Manuf IJIDeM 2022;16:381−8. https://doi.org/10.1007/s12008-021-00816-7.

[59] Zein H, El Sherbiny M, Abd-Rabou M, El Shazly M. Thinning and spring back prediction of sheet metal in the deep drawing process. Mater Des 2014;53:797−808. https://doi.org/10.1016/j.matdes.2013.07.078.

[60] Parsa MH, Ahkami SNA, Ettehad M. Experimental and finite element study on the spring back of double curved aluminum/polypropylene/aluminum sandwich sheet. Mater Des 2010;31:4174−83. https://doi.org/10.1016/j.matdes.2010.04.024.

[61] Esener E, Akşen TA, Ünlü A, Firat M. On the prediction of strength and deformation anisotropy of automotive sheets for stamping formability analysis. J Braz Soc Mech Sci Eng 2021;43:551. https://doi.org/10.1007/s40430-021-03276-y.

[62] Liu W, Feng S, Li Z, Zhao J, Wu G, Wang X, et al. Effect of rolling strain on microstructure and tensile properties of dual-phase Mg−8Li−3Al−2Zn−0.5Y alloy. J Mater Sci Technol 2018;34:2256−62. https://doi.org/10.1016/j.jmst.2018.05.002.

[63] Džoja M, Cvitanić V, Safaei M, Krstulović-Opara L. Modelling the plastic anisotropy evolution of AA5754-H22 sheet and implementation in predicting cylindrical cup drawing

process. Eur J Mech - ASolids 2019;77:103806. https://doi.org/10.1016/j.euromechsol.2019.103806.

[64] Chen Z, Zhao J, Fang G. Finite element modeling for deep-drawing of aluminum alloy sheet 6014-T4 using anisotropic yield and non-AFR models. Int J Adv Manuf Technol 2019;104:535−49. https://doi.org/10.1007/s00170-019-03921-w.

[65] Zhang L, Wang Y, Yang X, Li K, Ni S, Du Y, et al. Texture, Microstructure and Mechanical Properties of 6111 Aluminum Alloy Subject to Rolling Deformation. Mater Res 2017;20:1360−8. https://doi.org/10.1590/1980-5373-mr-2017-0549.

[66] Chahaoui O, Matougui N, Boulahrouz S, Heddar M, Babouri K. An Associated and Nonassociated Flow Rule Comparison for AISI 439-430TI Forming: Modeling and Experimental Analysis. Lat Am J Solids Struct 2021;18:e406. https://doi.org/10.1590/1679-78256724.

[67] Cvitanić V, Vlak F, Lozina Ž. A finite element formulation based on non-associated plasticity for sheet metal forming. Int J Plast 2008;24:646−87. https://doi.org/10.1016/j.ijplas.2007.07.003.

[68] Banabic D. An improved analytical description of orthotropy in metallic sheets. Int J Plast 2005;21:493−512. https://doi.org/10.1016/j.ijplas.2004.04.003.

[69] Lenzen M, Merklein M. Analysis of the Lankford coefficient evolution at different strain rates for AA6016-T4, DP800 and DC06, Penang, Malaysia: 2017, p. 160001. https://doi.org/10.1063/1.5008176.

[70] Wang H, Yan Y, Wan M, Wu X. Experimental investigation and constitutive modeling for the hardening behavior of 5754O aluminum alloy sheet under two-stage loading. Int J Solids Struct 2012;49:3693−710. https://doi.org/10.1016/j.ijsolstr.2012.08.007.

[71] Mars J, Wali M, Jarraya A, Dammak F, Dhiab A. Finite element implementation of an orthotropic plasticity model for sheet metal in low velocity impact simulations. Thin-Walled Struct 2015;89:93−100. https://doi.org/10.1016/j.tws.2014.12.019.

[72] Robert L, Velay V, Decultot N, Ramde S. Identification of hardening parameters using finite element models and full-field measurements: some case studies. J Strain Anal Eng Des 2012;47:3−17. https://doi.org/10.1177/0309324711430022.

[73] Ailinei I-I, Galatanu S-V, Marsavina L. Influence of anisotropy on the cold bending of S600MC sheet metal. Eng Fail Anal 2022;137:106206. https://doi.org/10.1016/j.engfailanal.2022.106206.

[74] Madivala M, Schwedt A, Prahl U, Bleck W. Anisotropy and strain rate effects on the failure behavior of TWIP steel: A multiscale experimental study. Int J Plast 2019;115:178−99. https://doi.org/10.1016/j.ijplas.2018.11.015.

[75] Pacheco M, García-Herrera C, Celentano D, Ponthot J-P. Mechanical Characterization of the Elastoplastic Response of a C11000-H2 Copper Sheet. Materials 2020;13:5193. https://doi.org/10.3390/ma13225193.

[76] Kami A, Dariani BM, Sadough Vanini A, Comsa DS, Banabic D. Numerical determination of the forming limit curves of anisotropic sheet metals using GTN damage model. J Mater Process Technol 2015;216:472−83. https://doi.org/10.1016/j.jmatprotec.2014.10.017.

[77] Marth S, Djebien S, Kajberg J, Häggblad H-Å. Stepwise modelling method for post necking characterisation of anisotropic sheet metal. Model Simul Mater Sci Eng 2021;29:085001. https://doi.org/10.1088/1361-651X/ac2797.

[78] Dzoja M, Cvitanic V. Parameter identification for anisotropic Yld2000-2d stress function under non-associated flow rule. 2019 4th Int. Conf. Smart Sustain. Technol. Split., Split, Croatia: IEEE; 2019, p. 1−6. https://doi.org/10.23919/SpliTech.2019.8783153.

[79] Xiong X, Zhang G, He L, Zhu C, Zhang Q, Lei Y. Study on Ta-2.5W alloy sheet texture evolution and r value anisotropy under different rolling reduction ratio. Mater Lett 2019;234:109−12. https://doi.org/10.1016/j.matlet.2018.09.073.

[80] Xie Q, Van Bael A, An YG, Lian J, Sidor JJ. Effects of the isotropic and anisotropic hardening within each grain on the evolution of the flow stress, the r-value and the deformation

texture of tensile tests for AA6016 sheets. Mater Sci Eng A 2018;721. https://doi.org/10.1016/j.msea.2018.02.053.

[81] Miller V, Berman T, Beyerlein I, Pollock T. Prediction of Magnesium Alloy Formability: The Role of Texture, 2016, p. 257−62. https://doi.org/10.1007/978-3-319-48114-2_51.

[82] Cvitanić V, Kovačić M. Algorithmic Formulations of Evolutionary Anisotropic Plasticity Models Based on Non-Associated Flow Rule. Lat Am J Solids Struct 2017;14:1853−71. https://doi.org/10.1590/1679-78253431.

[83] Hodowany J, Ravichandran G, Rosakis AJ, Rosakis P. Partition of plastic work into heat and stored energy in metals. Exp Mech 2000;40:113−23. https://doi.org/10.1007/BF02325036.

[84] Taylor GI, Quinney H. The latent energy remaining in a metal after cold working. Proc R Soc Lond Ser Contain Pap Math Phys Character 1934;143:307−26. https://doi.org/10.1098/rspa.1934.0004.

[85] Bever MB, Holt DL, Titchener AL. The stored energy of cold work. Prog Mater Sci 1973;17:5−177. https://doi.org/10.1016/0079-6425(73)90001-7.

[86] Skozrit I, Frančeski J, Tonković Z, Surjak M, Krstulović-Opara L, Vesenjak M, et al. Validation of Numerical Model by Means of Digital Image Correlation and Thermography. Procedia Eng 2015;101:450−8. https://doi.org/10.1016/j.proeng.2015.02.054.

[87] Chrysochoos A, Louche H. An infrared image processing to analyse the calorific effects accompanying strain localisation. Int J Eng Sci 2000;38:1759−88. https://doi.org/10.1016/S0020-7225(00)00002-1.

[88] Chrysochoos A, Huon V, Jourdan F, Muracciole J-M, Peyroux R, Wattrisse B. Use of Full-Field Digital Image Correlation and Infrared Thermography Measurements for the Thermomechanical Analysis of Material Behaviour. Strain 2010;46:117−30. https://doi.org/10.1111/j.1475-1305.2009.00635.x.

[89] Pottier T, Toussaint F, Louche H, Vacher P. Inelastic heat fraction estimation from two successive mechanical and thermal analyses and full-field measurements. Eur J Mech - ASolids 2013;38:1−11. https://doi.org/10.1016/j.euromechsol.2012.09.002.

[90] Samuel AF, Levin ZS, Trujillo CP, Fensin SJ, Demkowicz MJ, Beyerlein IJ, et al. Quasi-static and dynamic response of a Cu/Nb composite following equal channel angular extrusion. Mater Sci Eng A 2022;853:143711. https://doi.org/10.1016/j.msea.2022.143711.

[91] Chen J, Lu L, Lu K. Hardness and strain rate sensitivity of nanocrystalline Cu. Scr Mater 2006;54:1913−8. https://doi.org/10.1016/j.scriptamat.2006.02.022.

[92] Seidt JD, Kuokkala V-T, Smith JL, Gilat A. Synchronous Full-Field Strain and Temperature Measurement in Tensile Tests at Low, Intermediate and High Strain Rates. Exp Mech 2017;57:219−29. https://doi.org/10.1007/s11340-016-0237-z.

[93] Song J, Yang J, Liu F, Lu K. High temperature strain measurement method by combining digital image correlation of laser speckle and improved RANSAC smoothing algorithm. Opt Lasers Eng 2018;111:8−18. https://doi.org/10.1016/j.optlaseng.2018.07.012.

[94] Zhang B, Shim VPW. Determination of inelastic heat fraction of OFHC copper through dynamic compression. Int J Impact Eng 2010;37:50−68. https://doi.org/10.1016/j.ijimpeng.2009.07.003.

[95] Sendrowicz A, Myhre AO, Wierdak SW, Vinogradov A. Challenges and Accomplishments in Mechanical Testing Instrumented by In Situ Techniques: Infrared Thermography, Digital Image Correlation, and Acoustic Emission. Appl Sci 2021;11:6718. https://doi.org/10.3390/app11156718.

[96] Li L, Muracciole J-M, Waltz L, Sabatier L, Barou F, Wattrisse B. Local experimental investigations of the thermomechanical behavior of a coarse-grained aluminum multicrystal using combined DIC and IRT methods. Opt Lasers Eng 2016;81:1−10. https://doi.org/10.1016/j.optlaseng.2016.01.001.

[97] Krstulović-Opara L, Surjak M, Vesenjak M, Tonković Z, Kodvanj J, Domazet Ž. Comparison of infrared and 3D digital image correlation techniques applied for mechanical

testing of materials. Infrared Phys Technol 2015;73:166−74. https://doi.org/10.1016/j.infrared.2015.09.014.

[98] Jones EMC, Jones AR, Winters C. Combined thermographic phosphor and digital image correlation (TP + DIC) for simultaneous temperature and strain measurements. Strain 2022;58:e12415. https://doi.org/10.1111/str.12415.

[99] Tretyakova TV, Wildemann VE. Interrelation between local strain jumps and temperature bursts due to the jerky flow in metals under the complicate loading conditions: experimental study by using the DIC-technique and the IR-analysis. Procedia Struct Integr 2016;2:3393−8. https://doi.org/10.1016/j.prostr.2016.06.423.

[100] Hopmann C, Klein J. Determination of strain rate dependent material data for FEA crash simulation of polymers using digital image correlation. Comput Mater Sci 2015;100:181−90. https://doi.org/10.1016/j.commatsci.2015.01.021.

[101] Pan B. Digital image correlation for surface deformation measurement: historical developments, recent advances and future goals. Meas Sci Technol 2018;29:082001. https://doi.org/10.1088/1361-6501/aac55b.

[102] Quanjin M, Rejab MRM, Halim Q, Merzuki MNM, Darus MAH. Experimental investigation of the tensile test using digital image correlation (DIC) method. Mater Today Proc 2020;27:757−63. https://doi.org/10.1016/j.matpr.2019.12.072.

[103] Nowak M, Maj M. Determination of coupled mechanical and thermal fields using 2D digital image correlation and infrared thermography: Numerical procedures and results. Arch Civ Mech Eng 2018;18:630−44. https://doi.org/10.1016/j.acme.2017.10.005.

[104] Perić M, Tonković Z, Rodić A, Surjak M, Garašić I, Boras I, et al. Numerical analysis and experimental investigation of welding residual stresses and distortions in a T-joint fillet weld. Mater Des 2014;53:1052−63. https://doi.org/10.1016/j.matdes.2013.08.011.

[105] Golasiński KM, Staszczak M, Pieczyska EA. Energy Storage and Dissipation in Consecutive Tensile Load-Unload Cycles of Gum Metal. Materials 2023;16:3288. https://doi.org/10.3390/ma16093288.

[106] Pieczyska E, Maj M, Golasiński K, Staszczak M, Furuta T, Kuramoto S. Thermomechanical Studies of Yielding and Strain Localization Phenomena of Gum Metal under Tension. Materials 2018;11:567. https://doi.org/10.3390/ma11040567.

[107] Corigliano P, Epasto G, Guglielmino E, Risitano G. Fatigue analysis of marine welded joints by means of DIC and IR images during static and fatigue tests. Eng Fract Mech 2017;183:26−38. https://doi.org/10.1016/j.engfracmech.2017.06.012.

[108] Ben Ayed L, Robert C, Delamézière A, Nouari M, Batoz JL. Simplified numerical approach for incremental sheet metal forming process. Eng Struct 2014;62−63:75−86. https://doi.org/10.1016/j.engstruct.2014.01.033.

[109] Yeh FH, Li CL, Tsay KN. An Analysis of Forming Limit for Various Arc Radii of Punch in Micro Deep Drawing of the Square Cup. Adv Mater Res 2012;433−440:660−5. https://doi.org/10.4028/www.scientific.net/AMR.433-440.660.

[110] Hashemi A, Hoseinpour Gollo M, Seyedkashi SMH. Process window diagram of conical cups in hydrodynamic deep drawing assisted by radial pressure. Trans Nonferrous Met Soc China 2015;25:3064−71. https://doi.org/10.1016/S1003-6326(15)63934-6.

[111] Manabe K, Koyama H, Yoshihara S, Yagami T. Development of a combination punch speed and blank-holder fuzzy control system for the deep-drawing process. J Mater Process Technol 2002;125−126:440−5. https://doi.org/10.1016/S0924-0136(02)00363-1.

[112] Chen C-Y, Kuo J-C, Chen H-L, Hwang W-S. Experimental Investigation on Earing Behavior of Aluminum/Copper Bimetal Sheet. Mater Trans 2006;47:2434−43. https://doi.org/10.2320/matertrans.47.2434.

[113] Dachang K, Yu C, Yongchao X. Hydromechanical deep drawing of superalloy cups. J Mater Process Technol 2005;166:243−6. https://doi.org/10.1016/j.jmatprotec.2004.08.024.

[114] Fang Y, Lu B, Chen J, Xu DK, Ou H. Analytical and experimental investigations on deformation mechanism and fracture behavior in single point incremental forming. J Mater Process Technol 2014;214:1503−15. https://doi.org/10.1016/j.jmatprotec.2014.02.019.

[115] Dejmal I, Tirosh J, Shirizly A, Rubinsky L. On the optimal die curvature in deep drawing processes. Int J Mech Sci 2002;44:1245−58. https://doi.org/10.1016/S0020-7403(02)00019-X.

[116] Kishimoto T, Sakaguchi H, Suematsu S, Tashima K, Kajino S, Gondo S, et al. Deformation Behavior Causing Excessive Thinning of Outer Diameter of Micro Metal Tubes in Hollow Sinking. Metals 2020;10:1315. https://doi.org/10.3390/met10101315.

[117] Azizi R. Different implementations of inverse finite element method in sheet metal forming. Mater Des 2009;30:2975−80. https://doi.org/10.1016/j.matdes.2008.12.022.

[118] Lin B-T, Huang K-M, Kuo C-C, Wang W-T. Improvement of deep drawability by using punch surfaces with microridges. J Mater Process Technol 2015;225:275−85. https://doi.org/10.1016/j.jmatprotec.2015.06.012.

[119] Olguner S, Bozdana AT. Prediction of Lankford Coefficients for AA1050 and AA5754 Aluminum Sheets Using Uniaxial Tensile Tests and Cup Drawing Experiments. In: Ivanov V, Trojanowska J, Machado J, Liaposhchenko O, Zajac J, Pavlenko I, et al., editors. Adv. Des. Simul. Manuf. II, Cham: Springer International Publishing; 2020, p. 438−46. https://doi.org/10.1007/978-3-030-22365-6_44.

[120] Bruhin L. Method for determining the quality of a crimped connection between a conductor and a contact. EP2173015B1, 2010.

[121] KME. Copper materials n.d. https://www.kme.com/fileadmin/DOWNLOADCENTER/COPPER%20DIVISON/4%20Industrial%20Rolled/1%20Rolled%20Copper%20for%20the%20Industry/2023_KME_Handout_en_v1.pdf (accessed April 13, 2024).

[122] Mecal. Guide to quality crimping 2019. https://www.mecalbystarn.com/wp-content/uploads/2023/01/crimp-spec-chart-2019.pdf (accessed June 13, 2024).

[123] Meiners M, Mayr A, Kuhn M, Raab B, Franke J. Towards an Inline Quality Monitoring for Crimping Processes Utilizing Machine Learning Techniques. 2020 10th Int. Electr. Drives Prod. Conf. EDPC, Ludwigsburg, Germany: IEEE; 2020, p. 1−6. https://doi.org/10.1109/EDPC51184.2020.9388207.

[124] Lane C, Burguete RL, Shterenlikht A. An Objective Criterion for the Selection of an Optimum DIC Pattern and Subset Size. Proc. XIth Int. Congr. Expo., Orlando: 2008.

[125] Čanžar P, Tonković Z, Kodvanj J. Microstructure influence on fatigue behaviour of nodular cast iron. Mater Sci Eng A 2012;556:88−99. https://doi.org/10.1016/j.msea.2012.06.062.

[126] Cavusoglu O, Leacock A, Gürün H. Forming-limit diagrams and strain-rate-dependent mechanical properties of AA6019-T4 and AA6061-T4 aluminium sheet materials. Mater Tehnol 2016;50:1005−10. https://doi.org/10.17222/mit.2015.259.

[127] Leacock A, Gürün H, Güral A. STRAIN-RATE-DEPENDENT TENSILE CHARACTERISTICS OF AA 2139-T 351 ALUMINUM ALLOY NATEZNA TRDNOST ALUMINIJEVE ZLITINE AA 2139-T 351, 2017.

[128] Jiang Y, Hu J, Jiang Z, Lian J, Wen C. Strain rate dependence of tensile strength and ductility of nano and ultrafine grained coppers. Mater Sci Eng A 2017;712. https://doi.org/10.1016/j.msea.2017.11.083.

[129] Ubertalli G, Matteis P, Ferraris S, Marcianò C, D′Aiuto F, Tedesco MM, et al. High Strain Rate Behavior of Aluminum Alloy for Sheet Metal Forming Processes. Metals 2020;10:242. https://doi.org/10.3390/met10020242.

[130] Gu GH, Kim Y, Seo MH, Kim HS. A Method for Measuring Plastic Strain Ratio Over a Wide Strain Range Using the Digital Image Correlation Technology. Met Mater Int 2023;29:1880−4. https://doi.org/10.1007/s12540-022-01351-0.

[131] International Organization for Standardization. ISO 10113:2020. Metallic materials − Sheet and strip − Determination of plastic strain ratio 2020.

[132] Grozmani N, Chupina D, Montavon B, Schmitt RH. Sinogram interpretability based CT artefact reduction for multi-material workpieces. Nondestruct Test Eval 2022;37:679−91. https://doi.org/10.1080/10589759.2022.2091134.

[133] Ljubić L. KARAKTERIZACIJA PLASTIČNE ANIZOTROPIJE LIMA LEGURE CuFe2P. Master Thesis. Faculty of Electrical Engineering, Mechanical Engineering and Naval Architecture, 2021.

[134] Bridgman PW. The Effect of Hydrostatic Pressure on the Fracture of Brittle Substances. J Appl Phys 1947;18:246−58. https://doi.org/10.1063/1.1697610.

[135] Bridgman PW. Studies in Large Plastic Flow and Fracture: With Special Emphasis on the Effects of Hydrostatic Pressure. P. W. Bridgman. New York-London: McGraw-Hill, 1952. 362 pp. $8.00. Science 1952;115:424−424. https://doi.org/10.1126/science.115.2990.424.a.

[136] Grote K-H, Antonsson EK. Springer Handbook of Mechanical Engineering. Springer Science & Business Media; 2009.

[137] Hill R. A theory of the yielding and plastic flow of anisotropic metals. Proc R Soc Lond Ser Math Phys Sci 1948;193:281−97. https://doi.org/10.1098/rspa.1948.0045.

[138] Chen J, Wang Z, Chu X, Yue Z, Zhao C, Zhou Y. Calibration of Yld2000-2D Anisotropy Yield Criterion with Traditional Testing and Inverse Identification Strategies. Materials 2023;16:6904. https://doi.org/10.3390/ma16216904.

[139] Safaei M, Yoon JW, De Waele W. Study on the definition of equivalent plastic strain under non-associated flow rule for finite element formulation. Int J Plast 2014;58:219−38. https://doi.org/10.1016/j.ijplas.2013.09.010.

[140] Yoon S. theysy/UMAT_optimization_public. Matlab Scr Yld2004-18P 2024. https://github.com/theysy/UMAT_optimization_public (accessed February 5, 2024).

[141] Barlat F, Brem JC, Yoon JW, Chung K, Dick RE, Lege DJ, et al. Plane stress yield function for aluminum alloy sheets−part 1: theory. Int J Plast 2003;19:1297−319. https://doi.org/10.1016/S0749-6419(02)00019-0.

[142] Pevec D. Numeričko modeliranje dinamičkih procesa deformiranja tankih bakrenih limova. Master Thesis. Faculty of Mechanical Engineering and Naval Architecture, 2016.

[143] Yoon JW, Barlat F, Dick RE, Karabin ME. Prediction of six or eight ears in a drawn cup based on a new anisotropic yield function. Int J Plast 2006;22:174–93. https://doi.org/10.1016/j.ijplas.2005.03.013.